



# **The Nonlinear Dynamical and Shock Mitigation Properties of Tapered Chains**

**by Robert Doney**

**ARL-RP-0211**

**June 2008**

## **NOTICES**

### **Disclaimers**

The findings in this report are not to be construed as an official Department of the Army position unless so designated by other authorized documents.

Citation of manufacturer's or trade names does not constitute an official endorsement or approval of the use thereof.

Destroy this report when it is no longer needed. Do not return it to the originator.

# **Army Research Laboratory**

Aberdeen Proving Ground, MD 21005

---

---

**ARL-RP-0211**

**June 2008**

---

## **The Nonlinear Dynamical and Shock Mitigation Properties of Tapered Chains**

**Robert Doney**

**Weapons & Materials Research Directorate, ARL**

REPORT DOCUMENTATION PAGE				Form Approved OMB No. 0704-0188	
<p>Public reporting burden for this collection of information is estimated to average 1 hour per response, including the time for reviewing instructions, searching existing data sources, gathering and maintaining the data needed, and completing and reviewing the collection information. Send comments regarding this burden estimate or any other aspect of this collection of information, including suggestions for reducing the burden, to Department of Defense, Washington Headquarters Services, Directorate for Information Operations and Reports (0704-0188), 1215 Jefferson Davis Highway, Suite 1204, Arlington, VA 22202-4302. Respondents should be aware that notwithstanding any other provision of law, no person shall be subject to any penalty for failing to comply with a collection of information if it does not display a currently valid OMB control number.</p> <p><b>PLEASE DO NOT RETURN YOUR FORM TO THE ABOVE ADDRESS.</b></p>					
1. REPORT DATE (DD-MM-YYYY) June 2008		2. REPORT TYPE Progress		3. DATES COVERED (From - To) January 2004 to January 2007	
4. TITLE AND SUBTITLE The Nonlinear Dynamical and Shock Mitigation Properties of Tapered Chains				5a. CONTRACT NUMBER	
				5b. GRANT NUMBER	
				5c. PROGRAM ELEMENT NUMBER	
6. AUTHOR(S) Robert Doney				5d. PROJECT NUMBER	
				5e. TASK NUMBER	
				5f. WORK UNIT NUMBER	
7. PERFORMING ORGANIZATION NAME(S) AND ADDRESS(ES) U.S. Army Research Laboratory ATTN: AMSRD-ARL-WM-TA Weapons & Materials Research Directorate Aberdeen Proving Ground, MD 21005				8. PERFORMING ORGANIZATION REPORT NUMBER  ARL-RP-0211	
9. SPONSORING/MONITORING AGENCY NAME(S) AND ADDRESS(ES)				10. SPONSOR/MONITOR'S ACRONYM(S)	
				11. SPONSOR/MONITOR'S REPORT NUMBER(S)	
12. DISTRIBUTION/AVAILABILITY STATEMENT Approved for public release; distribution unlimited.					
13. SUPPLEMENTARY NOTES					
14. ABSTRACT <p>An analytic and numerical study of the problem of mechanical impulse propagation through a horizontal alignment of progressively shrinking (tapered) elastic spheres that are placed between two rigid end walls is investigated. Particular attention is paid to the shock absorption and nonlinear dynamical properties as they pertain to energy partition. The studies are confined to cases where initial loading between the spheres is zero. The spheres are assumed to interact via the purely repulsive and strongly nonlinear Hertz potential.</p> <p>Propagation of energy is analytically studied in the hard-sphere approximation and parameter space diagrams plotting normalized kinetic energy of the smallest grain at the tapered end are developed for various chain lengths and tapering factors. These details are then compared to congruent diagrams obtained via extensive dynamical simulations. Our figures indicate that the ratios of the kinetic energies of the smallest to largest grains possess a gaussian dependence on tapering and an exponential decay when the number of grains increases. The results demonstrate the capability of these chains to thermalize propagating impulses and thereby act as potential shock absorbing devices.</p>					
15. SUBJECT TERMS					
16. SECURITY CLASSIFICATION OF:			17. LIMITATION OF ABSTRACT  SAR	18. NUMBER OF PAGES  147	19a. NAME OF RESPONSIBLE PERSON Robert Doney
a. REPORT U	b. ABSTRACT U	c. THIS PAGE U			19b. TELEPHONE NUMBER (Include area code) 410-278-7309

**THE NONLINEAR DYNAMICAL AND SHOCK MITIGATION  
PROPERTIES OF TAPERED CHAINS**

BY

ROBERT L. DONEY III

B.S., George Mason University, 1995

M.S., George Mason University, 2001

DISSERTATION

A Dissertation submitted to the  
Faculty of the Graduate School of  
The State University of New York at Buffalo  
in partial fulfillment of the requirements for the  
degree of

( Doctor of Philosophy )

Department of Physics





*For Joey*

---

## JOSEPH RANDALL RAY

Feb. 27, 1977 - March 12, 2006

Staff Sgt., 391st Engineer Battalion, U.S. Army Reserve, Asheville, N.C

Last mission: Road clearing operations in Asadabad, Afghanistan

Son :: Brother :: Husband :: Father :: Friend :: Patriot

---

# Acknowledgements

I would like to first thank my advisor, Professor Sen, for introducing me to this intriguing and relevant problem. He has been a great mentor and friend during the 3 years that I've known him and allowed the flexibility I needed to complete this work *in absentia* from the University, carry on with a full-time job, and be a father and husband. Secondly, I'm indebted to my committee members, Professors Bruce Pitman and Richard Gonsalves, for taking time out of their busy schedules to read and evaluate the research in this dissertation and upcoming defense. Thanks so much to all of you.

I am lucky to be married to such a supportive and devoted wife and best-friend, Stacy, who also happened to be the babe in my dreams. She has helped me maintain my sanity and focus on countless occasions, even though I haven't been able to reciprocate as often due to the commitments this degree has required. This has gone on through the birth of our two wonderful girls, Sarah and Cora. I am happy to say that I don't have to hide in the basement in front of the computer most every weekend anymore. I love them all and this work could not have been completed without their strength.

I cannot thank enough my parents, Robert and Mattie, who have supported me in numerous ways since I started college — just a few of which includes living at home while completing a B.S. at GMU, financial support, encouragement, and rides back and forth to NVCC when I didn't have a car. There's no way I could have gotten anywhere as far without their love and support. I'd also like to thank my parents-in-law, Dave and Gina Moore, for their support since they've been through this before. Thanks to my sister, Dawn and her family Brian, Katherine, and Christopher for their encouragement and rocket scientist jokes. On the latter point, many thanks also to Randy, Helen, Tyler, and Kimberly Ray for their kind words and hospitality. They know what all the fuss is about. Thanks to Paw, Grandma (who passed away in my first year at SUNY) and my extended family — Ruane, Ronda, Lisa, and Rita and their families for their support and love. I'd also like to thank my posse from Fairfax who have watched all this work from the sidelines and rightfully shaken their heads. Thanks for the kegs, the parties, the laughter, the movies, the memories, and the +5



Hammer of Thunderbolts and Belt of Giant Strength being worn by a Kobald: Ryan, Leigh, Justin, C.J., Alex, Dave, Koz, Jason, Matt, Shannon, Neil, Monte, Wojtek, Steve, Tom, Adair, Cindy, Sue, Mike, and Heather.

This dissertation ends about 473 Megaseconds<sup>1</sup> of time spent pursuing degrees. During that period I've accumulated that many years of "professional" work experience from a bookstore (where I met Stacy!), the Radiation Research lab at Ft. Belvoir, NASA, Orbital Sciences, the Institute for Defense Analyses (IDA), and currently, the U.S. Army Research Laboratory. I have been fortunate to cross paths with many interesting people. Several of them have steered my career in some way and I'd like to recognize them — hopefully in chronological order.

To Mr. Runzo at Fairfax High School for getting me really intrigued in Physics. The episodes of the "Mechanical Universe" were a really cool way to go into the weekend.

Walerian Majewski, professor of Physics at Northern Virginia Community College was a big force early in my career (fall 90-spring 92). A serious chalkboard jockey, he had boundless energy in creating and getting us active in the Society of Physics Students. We gave presentations, did research on the relativistic lifetime extension of cosmic ray muons, built superconducting Meissner engines, collected data from the GEOS weather satellite, and did public outreach to local schools. Later I took a course from him in electromagnetics at GMU (fall 93) and his recommendation got me out of making \$5.70 per hour at Supercrown books and into the Radiation Research Lab making \$10.00 per hour. Sweet.

To Ram Bhat, Tim Mikulski, Tom Brown, and Walter Klaus for making work at the Radiation lab fun and safe. Well almost safe. I did safety surveys of an X-ray machine that must have been the original prototype. The safety interlock didn't work on the sampler input and the meter kept going off scale on my Geiger counter as I turned up the scale by 10x several times. A urine analysis later revealed it was just a few chest X-rays worth of dosage — at least they were free. And here's to the unsanctioned liquid nitrogen experiments. There's nothing quite like the yelp from someone who has had a super-cooled eraser placed on their bald head. How fast does a spider shrivel up when placed in liquid NO<sub>2</sub>? Fast. And in regard to the infamous all-you-can-eat student farewell party, no one...no one I say can eat 14 slices of meat and cheese lover's pan pizza for lunch and keep it down.

Thanks are extended to Pepsi for inventing Mountain Dew which kept me wired and vibrating for hours into the night. Twenty pounds later, I had to switch to Diet Mountain Dew: all the caffeine without the calories, who knew?

---

<sup>1</sup>15 years. For a good laugh, check out <http://en.wikipedia.org/wiki/Attoparsec>

I'm indebted to the many talented people at IDA and the role they played in getting me to where I am today. Gordie Boezer was an outstanding mentor and taught me quite a bit about diplomacy. Norm Jorstad, Mike Rigdon, and John Frasier also were invaluable in my professional development. Ira Kohlberg taught me that there is always more to teach somebody about computers. And Jim Heagy taught me there was someone who loathed microsoft's bloatware products more than myself. It was at IDA that I met Jim Sarjeant who invited me to SUNY Buffalo to work on microdischarge in insulators. Thanks go to him for introducing me to Bill Bruchey. I'd also like to thank Doug Hopkins, Harry Gill and Erik Althoff for making the EE experience fun. After a year and loss of interest there however, I decided to come back to physics where I found new challenges awaiting me in such treasures as Baym (in particular problem 11.2), Jackson, and Ashcroft and Mermin. I was lucky to become friends with several people and enjoyed their company around the BBQ grill. Many thanks go to Joe Helfer and Brian Powell for the awesome racquetball games. It's great to see them struggle so much when we play — after all, what dissertation is complete without a little smack-talk? I'd also like to thank Bill Condit who introduced me to Professor Sen as well as Marlene Kowalski, Pat Meider, and Joe Helfer for administrative support throughout the years.

Finally, I'm greatly indebted to ARL and the many people there who have fully supported all my academic ventures. In particular, thanks go to Bill Bruchey for bringing me in and getting me hired as a government employee; Mike Zoltoski for helping me get reimbursed, and Mike Keele for mentoring me. Scott Schoenfeld and John Runyeon have both strongly supported my education and required travel to Buffalo and APS-sponsored conferences to present the research. Finally, I'm indebted to John Powell, Chuck Hummer and Carl Krauthauser for their interest and review of this work for various publications.

# Table of Contents

Dedication . . . . .	iii
Acknowledgements . . . . .	iv
<b>Abstract . . . . .</b>	<b>ix</b>
<b>List of Figures . . . . .</b>	<b>xi</b>
<b>Chapter 1 Introduction . . . . .</b>	<b>1</b>
1.1 Statement of the Problem . . . . .	1
1.2 Background . . . . .	2
1.2.1 Granular Media . . . . .	2
1.2.2 Granular Chains: Computational and Theoretical studies . . . . .	3
1.2.3 Granular Chains: Experimental Work . . . . .	9
1.3 Mathematical Description of Problem . . . . .	10
1.3.1 The Hertz Potential . . . . .	10
1.3.2 Equations of Motion . . . . .	12
1.3.3 Restitutive Losses . . . . .	12
1.3.4 Boundary and Initial Conditions . . . . .	13
1.3.5 Numerical Approach . . . . .	13
1.4 Reduced Problem . . . . .	14
1.4.1 Single Particle System . . . . .	14
1.4.2 Two-Particle System . . . . .	16
<b>Chapter 2 The Simple Tapered Chain (STC) . . . . .</b>	<b>23</b>
2.1 Introduction . . . . .	23
2.2 Hard-Sphere Approximation . . . . .	23
2.2.1 Lossless STC Hard-Sphere Approximation . . . . .	24
2.2.2 Lossy STC Hard-Sphere Approximation . . . . .	25
2.2.3 KE Parameter Space for STC Hard-Spheres . . . . .	26
2.3 Numeric Solution . . . . .	26
2.3.1 Temporal Behavior . . . . .	28
2.3.2 KE and F Parameter Space Behavior . . . . .	34
2.3.3 Energy Partition . . . . .	35
2.3.4 The Approach to Quasi-equilibrium . . . . .	41
2.4 Mathematical fit of KE parameter space . . . . .	47
<b>Chapter 3 The Decorated Tapered Chain (DTC) . . . . .</b>	<b>60</b>
3.1 Introduction . . . . .	60
3.2 Hard-Sphere Approximation . . . . .	60
3.3 Numeric Solution . . . . .	66
3.3.1 KE Parameter Space Behavior . . . . .	66
3.3.2 Energy Partition . . . . .	66

<b>Chapter 4</b>	<b>Hydrocode Simulations of Tapered Chains . . . . .</b>	<b>69</b>
4.1	2D Eulerian ALEGRA simulations . . . . .	70
4.2	3D Lagrangian ALEGRA simulations . . . . .	72
<b>Chapter 5</b>	<b>Closing Remarks . . . . .</b>	<b>76</b>
<b>Appendix A</b>	<b>STC Code from Pfannes<sup>80</sup> . . . . .</b>	<b>81</b>
<b>Appendix B</b>	<b>DTC Code Modifications . . . . .</b>	<b>95</b>
<b>Appendix C</b>	<b>PERL Code . . . . .</b>	<b>98</b>
<b>Appendix D</b>	<b>Energy partitioning in the DTC . . . . .</b>	<b>101</b>
<b>Appendix E</b>	<b>Normalization . . . . .</b>	<b>112</b>
<b>Appendix F</b>	<b>CUBIT script for 3D STC . . . . .</b>	<b>114</b>
<b>Appendix G</b>	<b>ALEGRA script for 3D STC . . . . .</b>	<b>117</b>
<b>References</b>	<b>. . . . .</b>	<b>123</b>

# Abstract

An analytic and numerical study of the problem of mechanical impulse propagation through a horizontal alignment of progressively shrinking (tapered) elastic spheres that are placed between two rigid end walls is investigated. Particular attention is paid to the shock absorption and nonlinear dynamical properties as they pertain to energy partition. The studies are confined to cases where initial loading between the spheres is zero. The spheres are assumed to interact via the purely repulsive and strongly nonlinear Hertz potential. Two systems are studied, each representing a staggering number of possible chain designs. Propagation of energy is analytically studied in the hard-sphere approximation and parameter space diagrams plotting normalized kinetic energy of the smallest grain at the tapered end are developed for various chain lengths and tapering factors. These details are then compared to congruent diagrams obtained via extensive dynamical simulations. Our figures indicate that the ratios of the kinetic energies of the smallest to largest grains possess a gaussian dependence on tapering and an exponential decay when the number of grains increases. The conclusions are independent of system size, thus being applicable to tapered alignments of micron-sized spheres as well as those that are macroscopic and more easily realizable in the laboratory. The results demonstrate the capability of these chains to thermalize propagating impulses and thereby act as potential shock absorbing devices. While inertial mismatches in these granular chains lead to remarkable energy absorption, short chains are found to be limited in that regard. A second granular system is therefore proposed and investigated which greatly improves performance for any size chain. These new systems feature surprisingly complicated dynamics and are inadequately represented by a hard-sphere approximation. Additionally, such systems have shock absorption capacities that vary as a function of position along the chain, enabling customized shock absorbers.

Additional studies investigate energy partitioning and fluctuations are investigated. Approximate power laws are developed which fit the decay of average fluctuations as the size of the system increases. Advanced simulations of tapered chains utilizing the modern hydrocode, ALEGRA is introduced. These simulations incorporate elastic-plastic equation of state and behavior allowing

us to probe very large loading of tapered chains. This leads into the discussion of our continuing work beyond this dissertation including the design of a shock absorbing panel. Historical context is provided which has lead researchers to begin looking seriously at these alluring properties of granular or discretized systems.

# List of Figures

1.1	Hertz, $x^{5/2}$ , Hookean-like, $x^2$ , and hard core potentials where $n = 5, 10$ . . . . .	11
1.2	Phase space diagrams for equation (1.8). . . . .	15
1.3	Single particle system between fixed compressible walls under harmonic ( $n = 2.0$ ) and anharmonic ( $n = 2.5$ ) potentials (a) normalized kinetic energy, (b) phase space, (c) force versus displacement. . . . .	17
1.4	Half-periods plotted as a function of $v_i$ for various values of $n$ . Each superimposed fit has the form given by $T/2 = A(n)v_i^{-x(n)}$ (dashed). For each $n$ the values of $A, x$ are plotted in Figure 1.5. . . . .	18
1.5	Coefficients $x, A$ from Figure 1.4 plotted vs. $n$ and fitted with appropriate functions in support of generalized expression for $T/2$ . . . . .	18
1.6	Velocity and position phase diagrams for the two particle system. Dynamics are shown for the first 120 $\mu s$ with corresponding points of interest identified. Note that maximum velocities do not necessarily correspond to crossing the $t = 0$ positions. . .	20
1.7	Cartoon depicting the evolving two particle system. Refer to figure 1.6 for locations in phase space. . . . .	21
1.8	Overlap, $\delta$ , as a function of time for the particle-particle interface in the $N = 2$ system. $\delta$ is represented as a percentage of the two spheres combined radii since it is normalized by 10 mm ( $2R_i$ ). . . . .	22
2.1	Simple tapered chain: $N = 10$ , $q_s = 8\%$ , $L = 70.7$ mm, $r_i = 5$ mm. The rightmost particle is grain $i$ , its nearest neighbor is, $i + 1$ , etc. . . . .	24
2.2	Normalized $E_K(N, q, E_L)$ parameter space for the STC hard-sphere approximation. $N$ varies from 3 to 20 and $q$ from 0% to 10%. . . . .	27
2.3	Normalized $E_K(N, q)$ parameter space for the STC hard-sphere approximation where initial velocity is supplied to the smaller end of the chain. . . . .	28
2.4	KE as a function of time for the smallest particle in a chain with $N = 15$ , $\omega = 0.5$ . Each plot is evaluated for a different tapering with initial kinetic energy as 0.0838 J. . . . .	29
2.5	KE as a function of time for the smallest particle in a chain with $N = 20$ , $\omega = 0.5$ . Each plot is evaluated for a different tapering with initial kinetic energy as 0.0838 J. . . . .	30
2.6	Absolute positions, velocities, and kinetic energies for particles 11-15. Particle 15 is the last grain and is in contact with the boundary. The subplots (a-c) represent the monodisperse chain where each grain has $r = 5$ mm, while (d-f) corresponds to a chain with a tapering of 10% so that particles 11-15 have radii 1.74, 1.57, 1.41, 1.27, and 1.14 mm, respectively. These subplots illustrate when the grains in question first receive the incident impulse. Note the earlier time of arrival for $q = 0.1$ since velocities are higher (up to a factor of 3 in the plots). For panels (d-f) the dynamics have been extended beyond initial incidence and reflection. . . . .	31
2.7	Each of the plots depict force as a function of time for the tail and head particles in a chain with $N = 15$ , $\omega = 0.5$ . The value of the tapering increases for successive plots and is denoted by the label $q$ . Negative forces imply acceleration towards the smaller end of the chain. . . . .	32
2.8	Numerical solution of $E_K(N, q)$ parameter space for constant $\omega$ . . . . .	36

2.9	Numerical solution of $F(N, q)$ parameter space for constant $\omega$ . . . . .	37
2.10	Difference plot of the lossless KE parameter spaces for the hard-sphere approximation (Figure 2.2a) and numerical solution (Figure 2.8a). Note that the azimuthal view has been rotated 180 degrees for clarity. . . . .	37
2.11	Energy partitioning for STCs where $N = \{3, 8, 14, 20\}$ represents the number of spheres and $q_s = \{0.0, 0.05, 0.1\}$ is the tapering. Noisy plots resembling panel $l$ indicate shock absorbing systems while those similar to panel $j$ transmits an impulse as a solitary wave — essentially without loss. Panels $a-c$ represent efficient energy conversion systems. . . . .	38
2.12	Normalized KE for $N = 3, q_s = 0.05$ . $E_1$ represents the head of the chain and input; $E_2$ is the central bead; and $E_3$ is the tail. Note the periodicity of the system resulting in a recurrence time of just under $80 \mu s$ . . . . .	39
2.13	Instantaneous kinetic energy per grain for $N = 15, t = 52 \mu s$ and selected tapering. .	40
2.14	Normalized kinetic energy landscape. Vertical axes represents the particle id while the horizontal axis is time out to $1000 \mu s$ . . . . .	49
2.15	Velocity distribution with superimposed Gaussian fit for each particle in a STC with $N = 4, q = 0$ . Particle 1 represents the end of the chain and particle 4 represents the head where the initial impulse was applied. . . . .	50
2.16	Velocity distribution with superimposed Gaussian fit for each particle in a STC with $N = 20, q = 0$ . Particle 1 represents the end of the chain and particle 20 represents the head where the initial impulse was applied. . . . .	51
2.17	Average kinetic energy of the system as a function of $n$ and $N$ . . . . .	52
2.18	Average kinetic energy of the system determined from simulation (circles) and theoretical expectation by the Virial Theorem (dashed). . . . .	52
2.19	Partition of energy by grain number for several STCs where $N = \{3, 8, 14, 20\}$ and $q = \{0, 0.05, 0.1\}$ at $t = 100 \mu s$ . The red line indicates the theoretical expectation that $\langle KE_n \rangle = \frac{n/(n+2)}{N}$ . . . . .	53
2.20	Partition of energy by grain number for several STCs where $N = \{3, 8, 14, 20\}$ and $q = \{0, 0.05, 0.1\}$ at $t = 500 \mu s$ . The red line indicates the theoretical expectation that $\langle KE_n \rangle = \frac{n/(n+2)}{N}$ . . . . .	53
2.21	Partition of energy by grain number for several STCs where $N = \{3, 8, 14, 20\}$ and $q = \{0, 0.05, 0.1\}$ at $t = 1000 \mu s$ . The red line indicates the theoretical expectation that $\langle KE_n \rangle = \frac{n/(n+2)}{N}$ . . . . .	54
2.22	Fluctuations as a function of time and $n$ for $N = 100, q = 0$ . . . . .	55
2.23	(a) Variation of $\langle F \rangle$ with $N$ for various $n$ and fitting function. (b) Variation (scatter) of $k$ with $n$ . (c) Variation of $A$ with $n$ and corresponding fitting function. (d) Variation of $B$ with $n$ and corresponding fitting function. . . . .	56
2.24	$\langle F \rangle$ as a function of $n$ for various $N$ determined from simulation (circles). Derived fitting function $\langle F \rangle = \langle F(n, N) \rangle$ is superimposed (dashed) in each panel. $n = 2$ data is excluded as it doesn't fit the function. . . . .	57
2.25	$ v_{max} $ as a function of time for $N = 16, 18, 20, 50$ . . . . .	58
2.26	The Simulated and Modeled STC. . . . .	59
3.1	Several example DTCs created by varying $f$ and $q_d$ for constant $N = 13$ . . . . .	61
3.2	Normalized kinetic energy surfaces, $E_K \equiv K_{OUT}/K_{IN}$ , for the decorated chain under the hard sphere approximation as functions of the number of spheres, $N$ , fractional size of interstitial sphere, $f$ , and tapering, $q_d$ . . . . .	65
3.3	Numerically-produced normalized kinetic energy surfaces, $E_K \equiv K_{OUT}/K_{IN}$ , for the decorated chain as functions of the number of spheres, $N$ , fractional size of interstitial sphere, $f$ , and tapering, $q_d$ . Several sample chains are identified in panels (d-i). . . .	67
3.4	Instantaneous kinetic energy per grain for various DTC configurations at $t = 52 \mu s$ where $q_d = \{0, 0.05, 0.1\}$ and $f = \{1.0, 0.7, 0.3\}$ . . . . .	68
4.1	Computational domain and problem setup for the ALEGRA simulation. . . . .	70



4.2	Evolution of $ \sigma_{xx} $ . Color scale is logarithmic. . . . .	71
4.3	Basic 3D simulation of a TC. Note that the bulk behavior of the spheres is consistent with expectation even though dynamics take place on a elemental or nodal basis. A small amount of plastic flow is visible. . . . .	72
4.4	Velocity of the head particle as a function of time for both EOM and ALEGRA simulations where $N = 5, q = 0.07$ and restitutive losses are neglected. . . . .	73
4.5	Time elapsed sequence where the initial velocity of the left-most grain has been increased to 500 m/s (red). The remaining spheres are initially stationary (blue). . . .	75
5.1	Schematic of what a tapered chain armor panel might look like. . . . .	78
D.1	Instantaneous kinetic energy per grain for various DTC configurations at $t = 10\mu s$ where $q_d = \{0, 0.05, 0.1\}$ and $f = \{1.0, 0.7, 0.3\}$ . . . . .	102
D.2	Instantaneous kinetic energy per grain for various DTC configurations at $t = 20\mu s$ where $q_d = \{0, 0.05, 0.1\}$ and $f = \{1.0, 0.7, 0.3\}$ . . . . .	103
D.3	Instantaneous kinetic energy per grain for various DTC configurations at $t = 30\mu s$ where $q_d = \{0, 0.05, 0.1\}$ and $f = \{1.0, 0.7, 0.3\}$ . . . . .	104
D.4	Instantaneous kinetic energy per grain for various DTC configurations at $t = 40\mu s$ where $q_d = \{0, 0.05, 0.1\}$ and $f = \{1.0, 0.7, 0.3\}$ . . . . .	105
D.5	Instantaneous kinetic energy per grain for various DTC configurations at $t = 50\mu s$ where $q_d = \{0, 0.05, 0.1\}$ and $f = \{1.0, 0.7, 0.3\}$ . . . . .	106
D.6	Instantaneous kinetic energy per grain for various DTC configurations at $t = 60\mu s$ where $q_d = \{0, 0.05, 0.1\}$ and $f = \{1.0, 0.7, 0.3\}$ . . . . .	107
D.7	Instantaneous kinetic energy per grain for various DTC configurations at $t = 70\mu s$ where $q_d = \{0, 0.05, 0.1\}$ and $f = \{1.0, 0.7, 0.3\}$ . . . . .	108
D.8	Instantaneous kinetic energy per grain for various DTC configurations at $t = 80\mu s$ where $q_d = \{0, 0.05, 0.1\}$ and $f = \{1.0, 0.7, 0.3\}$ . . . . .	109
D.9	Instantaneous kinetic energy per grain for various DTC configurations at $t = 90\mu s$ where $q_d = \{0, 0.05, 0.1\}$ and $f = \{1.0, 0.7, 0.3\}$ . . . . .	110
D.10	Instantaneous kinetic energy per grain for various DTC configurations at $t = 100\mu s$ where $q_d = \{0, 0.05, 0.1\}$ and $f = \{1.0, 0.7, 0.3\}$ . . . . .	111



# Chapter 1

## Introduction

*Most of everyday life is nonlinear, and the principle of superposition fails spectacularly. If you listen to your two favorite songs at the same time, you wont get double the pleasure!* - Steven H. Strogatz<sup>108</sup>

### 1.1 Statement of the Problem

Most everyone is familiar with or has seen a Newton's cradle. This popular physics apparatus and desk mainstay marvelously demonstrates the conservation laws of energy and momentum. A further attribute of the system pointed out by Hermann, *et. al.*<sup>42-44</sup> is the requirement of dispersionless propagation when there are more than two spheres. Thus, the spheres must be identical. What most people may not be aware of however, is that by tapering the size of the spheres the system becomes a shock absorber.

This has broad implications since shock mitigation is one area that will always be receptive to improvements in the the state of the art. It encapsulates several important applications of military, commercial, and industrial interest, such as blast-proofing, vibrational or sound suppression, and noise filtering. Traditional methods of dealing with undesirable transients, such as that from ballistic shock, include metal foams and honeycombs<sup>33,34</sup>. When honeycombs are extruded, one obtains a linear cellular alloy<sup>41</sup>, which has demonstrated improved energy absorption capabilities<sup>32</sup>. Another approach to dismiss transients is through the use of functionally graded materials (FGM)<sup>14</sup> where one can introduce impedance mismatches gradually or discontinuously.

The general problem under investigation therefore is understanding the energy mitigation process behind one-dimensional alignments of tapered, metal spheres in contact. In particular, this has led to the investigation of two families of systems which are broadly referred to as tapered chains (TC). These alignments barely touch in their initial configuration and are not under any precompression. In addition, they are considered to be maintained between two fixed — but compressible — walls.

When an impulse is applied to one end of the system, it propagates via interparticle contacts and can be dissipated or maintained depending on the number of spheres, the ratio of adjacent particle sizes and energy losses. Energy coming out of the system (or anywhere therein) can be easily measured in computer simulations thus allowing one to quantify the energy absorption capability as a function of the system parameters. In this work, components of the system may be referred to as grains, particles, beads, or spheres.

It will be seen that such seemingly simple systems exhibit very interesting nonlinear dynamics. Indeed, the potential energy is strongly nonlinear and the equations of motion (EOM) have no known analytic solution. Even if there were a solution in closed form, it's not clear that one could divine any physical meaning or intuition from it due to its presumed complexity. As a result, and as is typical for nonlinear problems, one resorts to numerical methods to solve for the particles' position, velocity, and acceleration as a function of time. At this point, it is instructive to provide a history of the developments which have led us to this study—an amalgam of granular media, contact mechanics, and one-dimensional, discrete systems.

## 1.2 Background

The propagation of mechanical impulses along a chain of spheres has become an increasingly strong research area during the past decade. Tapered chain systems are customized 1D constructions of, fundamentally, granular media where the contact nature is quite intriguing and critical to the dynamics. Granular media is usually considered to be 2D and 3D entities. A brief review of some observed phenomenology (section 1.2.1) is useful since similar behavior may be seen and prove useful in the analysis of 1D systems. Section 1.2.2 provides examples of the computational and theoretical studies of granular chains, while section 1.2.3 covers the experimental endeavors.

### 1.2.1 Granular Media

Discrete or granular media<sup>29,48,49,51,64,91</sup> consists of particles that can range in size from micrometers to meters and number in quantity from several to the uncountable. The most well-known constituents of this group are sands and powders and are utilized across many disciplines. This media is particularly intriguing in that among other things it has properties of liquids and solids and calls have been made to add it as a fundamental state of matter<sup>29</sup>. It exhibits alluring behavior is seen in the phenomena of force networks, avalanches, and jamming. Mathematically, granular media can be shown to be similar to nonlinear rods<sup>120</sup>.

Granular media (in any number of dimensions) has been intensely investigated for understanding wave propagation<sup>1</sup>. Much of this has been in regard to understanding sound propagation. It has become such a curiosity since, in 2D or 3D, not all grains are under contact so various contact or force networks are formed. That is, only particles in contact admit mechanical energy propagation and the identified network visually appears dendritic. However, when one slightly shakes the granular bed, the network is completely changed. This is important for improving imaging of buried objects, such as munitions, in various soils. Sinkovits and Sen<sup>101,102</sup> presented simulations on the vertical propagation of weak and strong impulses in deep gravitationally compacted columns. In such asymmetrically loaded columns, the sound velocity,  $c$ , increases with depth as  $c \propto z^{1/6}$ , where  $z$  is the depth. Sen<sup>101</sup> extended the study to include voids and mass impurities. The inclusion of the latter caused backscatter at the defects even though the chains were monodisperse (identically-sized). This then prompted further study by Sen, *et. al.*<sup>98</sup> to report it as a possible mechanism for the detection of buried impurities, such as mines, bones, lost treasure, etc. The specific nature of the propagation<sup>59</sup> and backscattering<sup>60</sup> was investigated more thoroughly by Manciu who correlated the results into a dissertation<sup>58</sup> on nonlinear acoustics in granular media.

It is intriguing and suggestive that, conceptually, granular media can be envisioned as the inverse of a porous material. In a porous material, there are gaseous (air) voids within a solid matrix. For dry granular media, the reverse is true: solid (grains) voids exist within a gaseous matrix. This is an interesting comparison to draw because the considerable amount of work required to collapse the voids in a porous material makes it a favorable technology against ballistic shock<sup>32</sup>.

### 1.2.2 Granular Chains: Computational and Theoretical studies

Since the Hertz potential is strongly nonlinear, a review of nonlinear methods and waves was in order. It was believed that such resources would prove valuable in the analysis and approximation of TCs. While there are an inordinate number of books available on nonlinear dynamics<sup>39,40,67,68,73,74,105,106,108,114</sup>, they generally focus on perturbation-type solutions and analysis of the resulting nonlinear and chaotic waves<sup>9,70,106,112,118</sup>.

In most cases, undamped, damped and forced oscillators, such as the Van der Pol and Duffing oscillators, are examined in detail along with their behaviors in phase space. The behavior of nonlinear waves is introduced through the simplest forms of dispersive and diffusive equations<sup>9,73</sup>: the Korteweg de Vries (KdV) equation<sup>52,122</sup> and Burgers equation<sup>15</sup>, respectively. The KdV equation for example admits solitary wave solutions.

A shortcoming of these works is that none of them address fractional power exponents. Mickens<sup>67</sup> and Gottlieb<sup>38</sup> have the most relevant analytic work on oscillators with fractional power nonlinearities. Their approach uses the so-called Harmonic Balance technique<sup>66</sup> for periodic systems which matches the coefficients in a truncated Fourier series to determine the frequency of oscillation. A benefit of the method is that it does not require a perturbation parameter so it is applicable to strongly nonlinear systems. Harmonic Balance however seems to be limited to specific problems.

Solitary waves (SW) are intriguing because they propagate over very large distances with negligible dissipation<sup>86</sup>. The first known observation was reported in 1844 by Russell<sup>92</sup> who noticed water waves in a shallow canal propagate without loss over several miles. Ultimately they were broken apart by branching of the channel. An exhaustive historical account of the theoretical development of SWs is expounded by Sander<sup>93</sup>. It should be noted that when SWs collide and emerge unchanged they are referred to as solitons because of the similarity to particles<sup>83</sup>.

SWs were of particular interest in past studies since, for monodisperse chains, they are the mode of energy transport<sup>77,95</sup>. Sen and Pfannes demonstrated that it takes about 15 grains for the SW to form in such a chain. Considerable effort has been spent investigating the phenomena numerically and experimentally. Nesterenko first arrived at an analytic solution of a *precompressed*, monodispersed system using anharmonic and long wavelength approximations of the EOM<sup>75</sup>. The equations were then reduced to a form similar to the KdV equation<sup>52</sup> whereby SWs<sup>35</sup> were observed.

Lattice dynamics are dependent on the type of interaction potential chosen. The 1D (atomic) lattice and coupled oscillators immediately stand out where Morse<sup>7</sup>, exponential<sup>114</sup>, and other nonlinear (perturbative) potentials have been used. A common observable in most cases is the existence of solitary waves. In point, Toda<sup>114</sup> obtained exact (soliton) solutions in a one-dimensional lattice with exponential interactions in closed form.

Additionally, one of the more curious behaviors in granular chains is that of inelastic collapse<sup>63</sup>. This occurs when the separation between particles drops to zero due to a competition between the number of particles in the system and energy losses. Since the velocity of the particles involved in the collapse decay, this would be an ideal phenomenon to exploit for shock mitigation purposes. We have not yet investigated this.

In the following subsections, specific developments of FPU and mixed harmonic-anharmonic potentials and the overlap potential are discussed. This follows with some review of work focused on equipartition and equilibrium in such systems.

## FPU and mixed harmonic-anharmonic potentials

Fermi, Pasta, and Ulam<sup>30</sup> (FPU) are credited with the first computational study on energy sharing between modes where quadratic, cubic, and broken linear potentials were used. As a side note, the FPU 1D lattice has become a testbed for looking at various physics such as impulse propagation, defining temperature, and energy sharing among modes. An enormous body of literature is available on the subject. They noticed that upon the inclusion of such nonlinearities, energy that was initially fed to the lower mode became mixed among several lower order modes, but then returned to the lowest mode. Such recurrence can indicate hidden periodicities. These results are in contrast to a purely linear problem. For example, if one were to excite the lowest mode only in a general solution to the (linear) wave equation, the energy would stay in the fundamental mode for all time<sup>78</sup>.

The approach to equilibrium in discrete systems has been a topic of considerable interest for quite some time and the open literature is replete with examples. In general one wishes to understand whether the system reaches equilibrium by how energy is shared among the sites in a 1D lattice and how long it takes to do so. Typically the systems studied have a Hamiltonian of the form,  $H = H_0 + \epsilon H_1$  where  $H_0$  represents the linear portion,  $H_1$  represents nonlinear ( $\sin(x)$ ,  $x^3$ ,  $x^4$ , etc.) terms and  $\epsilon$  is a tuning parameter. In this sense, many of the perturbation techniques in previous references may be applied. An additional benefit is that one can monitor how energy is shared between normal modes from the linear system and the effects of adding a small nonlinear perturbation.

Fermi addressed the question of energy equipartition<sup>30</sup> and Toda<sup>114</sup> points out lucidly,

Fermi did some work on the ergodic problem when he was young, and when electronic computers were developed he came back to this as one of the problems computers might solve. He thought that if one added a nonlinear term to the force between particles in a one-dimensional lattice, energy would flow from mode to mode eventually leading the system to a statistical equilibrium state where the energy is shared equally among the modes.

This investigation sparked a broad literature base<sup>24,85</sup> and a description of some of this work follows. Ford and Waters have addressed the issue of equipartition of FPU systems in several exhaustive papers. Ford<sup>31</sup> used a perturbation technique to show that the chain originally used by FPU didn't equipartition energy because of an inappropriate choice of frequencies. He argues that for weakly coupled oscillator system — with linear and nonlinear terms — one should expect (internal) resonance and energy sharing when the sum of harmonic frequencies is approximately

zero.

Tobolsky *et. al.*<sup>113</sup> observed equipartition for several lattice models. They commented however that the probability of a given deviation of kinetic and potential energies from one-half approaches a limit that decreases with increasing  $N$ . For a deviation,  $x$ , with probability of 1% being exceeded, I measure this decay (based on their data) as  $x = 3/(4\sqrt{N})$ , where  $N$  is the number of particles.

Boccheri *et. al.*<sup>10</sup> numerically investigate a one dimensional chain of particles with nearest neighbor interactions using a Lennard-Jones potential. They conclude that when the particle vibration energy exceeds a few percent of the depth of the potential well, equipartition of energy among the normal modes *is* satisfied in the time average. This is in contrast to the Toda lattice<sup>114</sup> where exponential interactions were not compatible with equipartition of energy in the time average.

Rosas and Lindenberg<sup>89</sup> studied pulse propagation in FPU lattices (where only quartic nonlinearities were considered). They varied the input velocity governing whether harmonic or anharmonic terms dominate (since the velocity of nonlinear waves is amplitude dependent). They concluded that the pulse width is not an appropriate measure of the way a pulse spreads in a purely anharmonic lattice but rather it measures the span over which a series of decreasing velocity pulses exist. This was an extension of an earlier, more comprehensive, study by Sarmiento *et. al.*<sup>94</sup>. They measured pulse propagation in isolated FPU chains and also those coupled to heat baths of zero and finite temperatures as well as 2d isolated arrays.

Finally, one of the more recent discoveries has been the observation of “breathers” —periodic and localized nonlinear lattice excitations<sup>81</sup>. These spontaneous and long-lived localizations of energy result from competition between nonlinearity and space discreteness<sup>81</sup>. Another typical requirement is for the array to be cooled at the boundaries. Essentially, all energy dissipation takes place at the end points and is equivalent to the physical situation of a surface cooling much faster than the bulk of the medium. Breathers emerge from such configurations where the lattice is initially thermalized and is an evolved form of self-excited oscillations—another nonlinear behavior. In this report, such behavior has not been observed because free-end BCs nor boundary-only cooling have been considered. Further conclusions of Piazza, *et. al.* were that breather mobility is impacted if space discreteness (i.e. weak nearest neighbor interaction or restoration potential) is too large.

## Overlap potential

The study of granular columns is dominated by the Hertz potential — see equation (1.3). This is a special case of the more generalized overlap potential,  $\delta^n$ . The overlap potential is quite distinct from FPU and other lattice potentials. First, they lack a harmonic term — that is, they are strongly



nonlinear. Thus, nonlinear perturbation methods fail when looking for a solution. Second, and most important, is that they lack a restoring term. So even if the overlap potential is considered with a “harmonic” exponent,  $\delta^2$ , the chain is very dissimilar from a simple harmonic system.

Nesterenko is considered to be the pioneer of theoretical, computational, and experimental studies of SW in Hertzian chains. His work is found compiled in chapter one of his book<sup>76</sup> which includes translations of his Russian publications. He was the first to observe solitons in Hertzian chains<sup>75</sup> and also dubbed such granular chains a “sonic vacuum,” since particles can lose contact when precompression in the chain is not considered.

The phenomenology of SWs in granular chains was addressed specifically in several computational papers by Sen and Manciu<sup>61,95</sup>. For long, uncompressed chains—where boundary effects are ignored—they observed that SWs are the mode of energy transport when  $n > 2$ . They used a combination of computational and analytic arguments to guess a form of the SW as,  $\phi_n(z) = -(A/2) \tanh[f_n(z)/2]$ , where the  $f_n(z)$  represents a series expansion in  $z$  and requires calculation of the coefficients for each term in the series. Their solution agrees quite well with simulations when only the first three coefficients are solved. Thus they were able to obtain displacement, velocity, and acceleration functions for the SW. This approach differs from that of Nesterenko’s long wave, or continuum, approximation in that zero precompression is considered and the EOM are not linearized. Their subsequent publication investigates how propagation of the SW is affected by dissipation and disorder for arbitrary power-law repulsive potentials,  $\delta^n$ . They conclude that even in the presence of disorder, a SW propagates—maintaining its width while the amplitude decreases exponentially with distance. The attenuation is common whether energy loss is caused by restitution or velocity-based friction, or from multiple backscattering events due to randomly-sized particles in the chain. The attenuation commonality thus enables one to choose an energy loss mechanism that is convenient. An additional note of interest is that as the SW propagates in the disordered medium, part of the energy remains behind the leading edge in the form of noise which doesn’t interfere with the SW. Since wave velocity is a function of amplitude and noise has a much smaller amplitude, the SW outpaces noise.

In a subsequent study, Sen *et. al.*<sup>97</sup> inquired as to whether it was possible to convert an impulse into thermal energy. Based on supporting computational studies they concluded that when particle radii taper to smaller sizes, the traveling SW must get “squeezed” into a smaller size. The SW consequently loses its reflective symmetry and is destroyed. More specifically, the SW is rapidly attenuated and undergoes dispersion due to progressively smaller and faster particle masses. That the energy transport mechanism was found to be disabled by tapered chains led to many exciting

questions and became the foundation for this dissertation. Curiously, Póschel and Brilliantov<sup>82</sup> found that by using a constant coefficient of restitution, one obtains optimum energy transmission if the mass of each particle is prescribed by an exponentially decreasing function.

Wu<sup>121</sup> uses an independent collision or binary collision model to understand wave propagation in uniform (monodisperse) and tapered chains. In such a system, energy is always confined to a single particle. This model is analogous to hard-spheres which is derived in sections 2.2 and 3.2.

Rosas and coauthors perform a series of relevant studies with Hertzian chains. In the first work<sup>87</sup>, the authors look at how propagation and backscattering between two granules is affected by the type (kinetic or hydrostatic) of friction and its magnitude. Among their conclusions is that friction on the second granule is responsible for backscattering. And in sum, they found a drastic asymmetry between backscattering and propagation for various frictional states. This work is followed up<sup>88</sup> by concluding that a binary collision model is quantitatively correct for (hard) potentials where  $n \geq 3$ . This is because the pulse is so narrow that at any given moment the energy is concentrated in just a few particles. Indeed they reiterate that in the continuum approximation ( $N \rightarrow \infty$ ), the pulse width goes as  $\alpha = \sqrt{(6(n-2))^2/n(n-1)}$ . Subsequently, the authors investigate frictional effects further for cylindrical and spherical granules<sup>90</sup>. An interesting result for the cylindrical case is that the backscatter velocity for finite friction is *greater* than that when it is neglected. They also find an exponential decay to the velocity of backscatter velocity as well as energy. The latter is in agreement with findings in this report (see figure 2.26(a)— $T(\omega)$  decays exponentially)

In more recent work, a new type of steady-state behavior, quasi-equilibrium<sup>99,100</sup>, has been observed. The findings of the authors' are summarized as follows. Without a linear, harmonic term in the potential, grains do not exhibit simple harmonic motion which produces sound waves — indeed a restoring term is required. This is the “sonic vacuum” Nesterenko referred to. As such, information or energy is transmitted by groups of particles rather than individual grains. When an interaction with a boundary occurs, energy remains nucleated at the site, some of which goes into recreating an attenuated SW while the rest rattles about, creating secondary SW (SSW)<sup>57</sup> of very small amplitude. Since SW width is controlled by  $n$ , the system transmits energy via SW and SSWs such that (1) large and small SW collisions exchange momenta if parallel<sup>114</sup>; (2) they undergo breakdown and reconstruction with attenuation by antiparallel collisions or interaction with a boundary<sup>59</sup>. At large times, it was found that the system tends towards a Gaussian velocity distribution. Apparently in all cases studied, the process of reconstructing a SW is imperfect. There is attenuation every time a boundary is encountered, the remaining energy goes into making SSW.

Mohan and Sen<sup>69</sup> investigated similar questions for mass-spring systems with quartic interactions

for both periodic and rigid, perfectly reflecting boundary conditions. They found that for the purely harmonic mass-spring chain, energy quickly approaches  $E_0/N$  per particle, thus equipartition was achieved. In the mixed harmonic/anharmonic case, the presence of harmonicity tends to “wash-out” nonlinear effects. Therefore the comparative strengths of linear and nonlinear terms become an important factor in determining the relaxation time.

### 1.2.3 Granular Chains: Experimental Work

Some of the earliest experimental work focused on the establishment of the restitutive coefficient for various materials and contact time of impacts. For example, Goldsmith<sup>36</sup> illustrated that the duration of contact,  $\tau$ , for two identical materials is,

$$\log \tau = -\frac{1}{5} \log v_i + \log \left\{ \left( 4.53 \frac{2(1-\sigma^2)m_1m_2}{E(m_1+m_2)} \right)^{2/5} \left( \frac{R_1+R_2}{R_1R_2} \right)^{1/5} \right\} \quad (1.1)$$

which is consistent with Hertz theory.

The validity of the Hertz potential has been discussed in several papers<sup>21,75</sup>. Bokor and Leventhall<sup>11</sup> verified Hertz validity outside its theoretical regime—mainly when permanent (inelastic) surface deformations occurred. Experiments have also been performed which look at force versus time plots<sup>46</sup> of colliding spheres to determine the power of the restoring term.

Rossmannith and Shukla<sup>91</sup> performed the first study on photoelastic investigations of granular media. Their work spotlighted dynamic load transfer in 1D vertical and increasingly oblique zig-zag columns of the photoelastic material, Homalite 100. This was further expanded to 2D beds of roughly-surfaced and multi-sized disks. The reported isofringe patterns in general correspond to higher stress accumulations. In addition, their report represents an excellent validation exercise for 3D hydrocode simulations (4).

Much experimental work has been carried out by Nesterenko and collaborators. One interesting area receiving attention, is through clever adjustment of material parameters. In this case, beads alternate in material composition rather than size. This has been investigated experimentally by Daraio<sup>23</sup>, yet I am unaware of numerical studies.

Coste *et. al.*<sup>20</sup> experimentally validate Nesterenko’s work where both zero and finite precompression is considered through force measurements on a sensor. The authors stress that no adjustable parameter had been used to corroborate their results.

Warr and Huntley<sup>117</sup> derive from experiment an exact expression for the rate of energy input into a system consisting of a single particle vibrating on a base plate in one dimension. The agitation

coupled with the rate of energy dissipation allowed the steady state of the system to be determined energetically. In particular they found,  $E_p = 1.7m_p V^2/(1 - \epsilon)$ , where  $V$  is the base plate velocity,  $\epsilon$  the coefficient of restitution, and  $E_p$  and  $m_p$  are the particle energy and mass, respectively. Additional research<sup>56</sup> investigates the phase behavior—fluidization and condensation (also known as clumping)—of a column of beads under similar vibrating plates.

Nakagawa *et. al.*<sup>72</sup> experimentally confirm impulse dispersion in tapered chains. They further provide a derived measurement for the coefficient of restitution of 0.95 and account for discrepancies in the computational studies by arguing that some of the energy is transferred to rotational degrees of freedom. Experimental work has also focused on the observation of SWs and their behavior at boundaries<sup>50,65,104</sup>. With relevance to chapter 3, a “decorated tapered chain” prototype has very recently been constructed for empirically testing and validating its shock mitigation capability<sup>2</sup>.

## 1.3 Mathematical Description of Problem

We define TCs (see for example figure 2.1) as 1-D granular arrays of elastic spheres that touch at a single point in their initial state and grow to a disk under compression in the plane perpendicular to the figure. The chains can be characterized by the number of grains,  $N$ , the successive decrease in size of the grains or tapering,  $q$ , and restitutive or energy losses,  $\omega$ .

The Hamiltonian of the system is represented as,

$$H = \frac{1}{2} \sum_i m_i \dot{x}_i^2 + \sum_i V(\delta_{i,i+1}^n) \quad (1.2)$$

where  $V(\delta_{i,i+1}^n)$  is the overlap potential. When  $n = 5/2$ ,  $V$  is referred to as the Hertz potential and is described in section 1.3.1. The equations of motion follow in section 1.3.2, resitutive losses in section 1.3.3, relevant boundary and initial conditions in section 1.3.4, and the numeric approach to solving the  $N$  equations of motion in section 1.3.5.

### 1.3.1 The Hertz Potential

The contact mechanics between adjacent elastic spheres was first identified by Hertz<sup>45</sup> circa 1882. Derivations of the interaction potential were later performed by both Landau<sup>53</sup> and Love<sup>55</sup>, with a simplified, order of magnitude approach by Leroy<sup>54</sup>. The results were that for spheres under compression, one obtains a completely repulsive and nonlinear potential. This Hertz potential can be written<sup>75,97</sup> as,

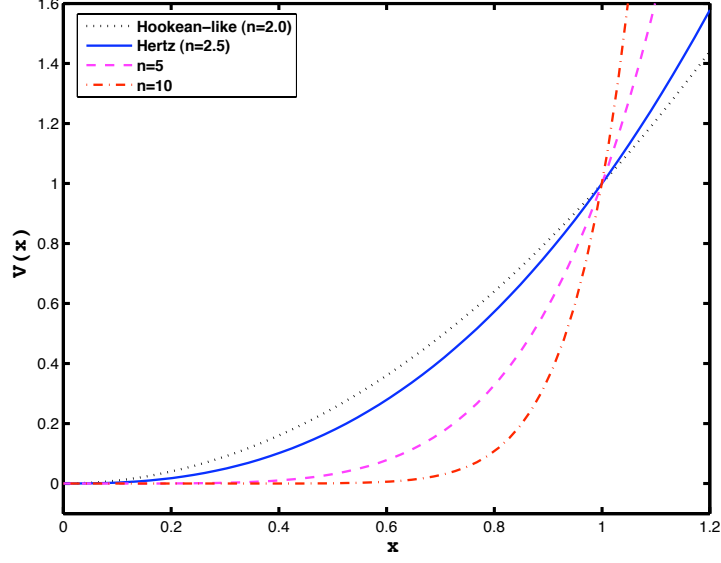


Figure 1.1: Hertz,  $x^{5/2}$ , Hookean-like,  $x^2$ , and hard core potentials where  $n = 5, 10$ .

$$V(\delta_{i,i+1}) = \frac{2}{5D} \sqrt{\frac{R_i R_{i+1}}{R_i + R_{i+1}}} \delta_{i,i+1}^{5/2} \equiv a_{i,i+1} \delta_{i,i+1}^{5/2}, \quad (1.3)$$

where

$$D = \frac{3}{4} \left( \frac{1 - \sigma_i^2}{E_i} + \frac{1 - \sigma_{i+1}^2}{E_{i+1}} \right). \quad (1.4)$$

Here,  $\delta_{i,i+1} = R_i + R_{i+1} - (z_{i+1} - z_i) > 0$ , represents the overlap between successive grains where  $z_j$  is their position. Additionally, the constant  $a_{i,i+1}$  has been defined for material properties:  $E_j$ , the Young's modulus and  $\sigma_j$ , the Poisson ratio; and radii,  $R_j$ . Note that  $j$  can refer to either particle  $i$  or  $i + 1$ . The use of an overlap function is to supplant the complicated details of compression and expansion. Note, that the nonlinearity in the potential is completely due to geometric effects. Further, the theory does not take into account plasticity.

For our particular study, all materials are the same in any *single* tapered chain so that equation (1.4) reduces to:

$$D = \frac{3}{2} \left( \frac{1 - \sigma^2}{E} \right). \quad (1.5)$$

If  $\delta_{i,i+1} \leq 0$  then  $V = 0$  since adjacent grains  $i$  and  $i + 1$  have lost contact. It may be noted

that equation (1.3) describes a repulsive potential that grows faster than a quadratic—or Hookean-like—form of  $\delta_{i,i+1}^2$ . The phrase, “Hookean-like” is used to stress the lack of a restoring term. The Hertz repulsion is hence a nonlinear force. More specifically, the repulsion is softer than something harmonic over short distances, but becomes steeper than a harmonic form with increasing compression. An extreme case would be the hard-sphere potential ( $n \rightarrow \infty$ ). These details are illustrated in Figure 1.1 where  $V(x)$  is plotted for various values of  $n$ .

### 1.3.2 Equations of Motion

The EOM for grain  $m_i$  at position  $z_i$  is constructed from equation (1.3) as

$$m_i \ddot{z}_i = \frac{5}{2} \left\{ a_{i-1,i} \delta_{i-1,i}^{3/2} - a_{i,i+1} \delta_{i,i+1}^{3/2} \right\}, \quad (1.6)$$

where the dots imply differentiation with respect to time. Recall that  $\delta_{i,i+1} = R_i + R_{i+1} - (z_{i+1} - z_i)$  represents the overlap of successive grains where  $z_j$  is the position of a grain. Results have been obtained for a large selection of chains consisting entirely of  $\text{Ti}_6\text{Al}_4\text{V}$  and  $\text{SiC}$  spheres. Arbitrarily, we have chosen to use  $\text{Ti}_6\text{Al}_4\text{V}$  when restitutive losses are ignored ( $\omega = 0$ ), and  $\text{SiC}$  otherwise. The following material properties<sup>62</sup> were assumed (where  $D$  is defined in equation (1.5)):

Table 1.1: Material Properties

Material	$\rho(\text{mg/mm}^3)$	$D(\text{mm}^2/\text{kN})$	Occurrence
SiC	3.2	0.003266	$\omega \neq 0$
$\text{Ti}_6\text{Al}_4\text{V}$	4.42	0.01206	$\omega = 0$

Note that the fundamental units of length, time, mass, and force in our simulations are the millimeter, microsecond, milligram, and kilonewton, respectively. This is to minimize potential rounding errors from small numbers.

### 1.3.3 Restitutive Losses

Real systems have various modes of energy dissipation—sliding, rolling, sound, etc. The literature is replete with methods for invoking restitutive losses<sup>5,6,19</sup>, many of them velocity based<sup>109</sup>. For simplicity, we have utilized the method of Walton and Braun<sup>116</sup>, where the coefficient of restitution,  $\omega$ , is defined as  $F_{\text{unload}}/F_{\text{load}} = 1 - \omega$ . Here  $F_{\text{unload}}$  represents the expansion phase of the contact event, and  $F_{\text{load}}$  is the compression phase. Values of  $\omega$  are constant (thus hydrostatic) throughout the simulation for each TC and are chosen as  $0 \leq \omega \leq 0.1$ . Therefore perfectly elastic collisions

correspond to  $\omega = 0$ . The majority of this report however focuses on  $\omega = 0$  since it establishes an upper limit or worst case scenario in terms of energy mitigation.

### 1.3.4 Boundary and Initial Conditions

In our model, the two boundaries consist of fixed, compressible walls. This is equivalent to spheres of infinite radius. As a result, the potential is adjusted such that  $R_0, R_{N+1} \rightarrow \infty$ . At an interface with the boundary, equation (1.3) becomes

$$V_B = \frac{2\sqrt{R}}{5D}(R - z_{i=1,N})^{5/2},$$

where  $R$  and  $z$  represent a particle adjacent to the boundary. One should therefore expect behavior at the boundary to be much different than that for interior particles.

The initial conditions have been based on a delta impulse applied to a bead at the edge (head) of the chain. Specifically, the conditions are

$$\begin{aligned}\dot{x}_{i=N}(t=0) &\neq 0, \\ \dot{x}_{i=1,2,\dots,N-1}(t=0) &= 0.\end{aligned}$$

Unless otherwise stated, the  $N$ th particle is given an initial velocity of  $0.01 \text{ mm}/\mu\text{s}$  ( $10 \text{ m/s}$ ). This condition could be compared to a particle being released into a zero-temperature bath of  $N - 1$  particles.

### 1.3.5 Numerical Approach

The original code was written by Pfannes<sup>80</sup> and is documented in appendix A. Modifications were needed to support studies in this report. The most significant of those were in regard to the decorated tapered chain (chapter 3) and is documented in appendix B. In these numerical studies, the velocity-Verlet algorithm<sup>3</sup> is used to solve the differential equations. The position and velocity information are updated according to:

$$\begin{aligned}x(t + \Delta t) &= x(t) + v(t)\Delta t + \frac{\Delta t^2}{2}a(t) \\ v(t + \Delta t) &= v(t) + \frac{\Delta t}{2}[a(t) + a(t + \Delta t)],\end{aligned}$$

where  $\Delta t$  represents the timestep. Accelerations are calculated from Newton's law where the force is evaluated based on the amount of overlap determined by  $x(i), x(i+1)$ . Most simulations were evaluated over a system time of 1 ms where the timestep was set to 10 picoseconds with  $10^8$  steps in the integration loop. In some cases, the simulation time was extended to 10 ms. For each simulation, a separate data file is written for each particle which contains the position, velocity, acceleration, kinetic energy, and other variables per timestep. In addition, a global file containing the potential, kinetic, and total energy of the whole system per time step is also written out.

To handle the thousands of simulations that needed to be run, an automation script using PERL was written. Appendix C lists the code that iterates through nested loops of the relevant chain parameters. In each cycle, it creates new subdirectories based on the current value in the loops, copies a template containing the C++ source listed in appendices A or B to that location, replaces the parameters with the current values in the loop, compiles the code, and then runs it. This is iterated 2200 times for simulations comprising chapter 2 and about 1000 times for simulations comprising chapter 3.

## 1.4 Reduced Problem

In order to gain an understanding of the more complicated motions for systems where  $3 \leq N \leq 20$ , it is useful to look at single and binary systems confined between fixed, but compressible walls. It is also pedagogical to observe the changes in phase space when one moves from a harmonic-like ( $n = 2$ ) to anharmonic ( $n \neq 2$ ) dependence in the overlap potential.

### 1.4.1 Single Particle System

To highlight the analytical difficulties in dealing with equations such as that in (1.6), consider the simplified, but general problem,

$$\ddot{x} + x^{(n-1)} = 0, \tag{1.7}$$

with initial conditions,  $x(0) = 0, \dot{x}(0) = v_0$ , where  $n > 2$  and values may be fractions. Surprisingly, little work has been done in dealing with solutions to second order differential equations where fractional powers need to be considered. There have been several efforts by Gottlieb<sup>38</sup> and the pioneering work of Mickens<sup>67</sup> who have used the method of harmonic balance which uses a truncated Fourier series to approximate the solution. A great benefit to this method is that it doesn't require perturbation of linear terms, so it can — in principle — work with strongly nonlinear equations.



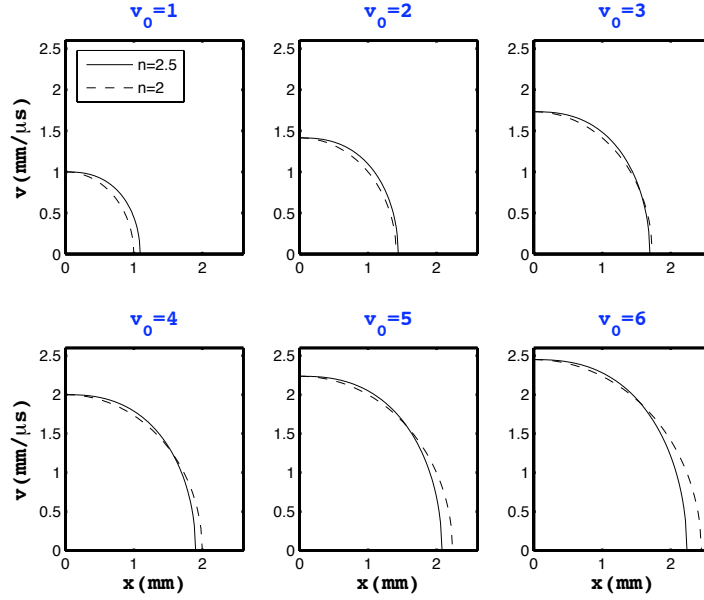


Figure 1.2: Phase space diagrams for equation (1.8).

However, efforts have so far have failed to produce a closed form solution to  $x(t)$  in equation (1.7).

One obtains the first integration of equation (1.7) as,

$$\dot{x} = \sqrt{v_0^2 - \frac{2}{n}x^n}. \quad (1.8)$$

Without explicitly solving the EOM, one can certainly plot the phase space  $(\dot{x}, x)$  for, say,  $n = 2.0, 2.5$ . This is illustrated in figure 1.2 for a variety of  $v_0$  (arbitrary units). Starting at  $v(x=0)$  in each plot, compression increases as the particle slows down. For  $v_0 = 1$ , the Hertz potential is soft allowing greater compression than that for  $n = 2$ . This was also reported in figure 1.1. As  $n$  increases the nonlinear effects become apparent as the Hertz potential becomes increasingly more repulsive with compression. One should expect therefore, a phase space similar to the above when looking at the numeric solution.

To calculate the period of oscillation,  $T$ , note that in a quarter-cycle the maximum compression  $x_m$  corresponds to  $v = 0$ . The period can then be written as,

$$T = 4 \int_0^{(nv_0^2/2)^{1/n}} \frac{dx}{\sqrt{v_0^2 - \frac{2}{n}x^n}}. \quad (1.9)$$

For  $n = 2$ , one obtains the trivial solution,  $T = 2\pi$ . It is clear that for  $N$  such equations coupled by particle overlaps, one needs to resort to numerical methods to evaluate  $x_i(t)$ .

Figure 1.3 highlights the numeric results for the harmonic-like,  $n = 2$  and Hertz,  $n = 2.5$ , cases. Both are oscillators and what stands out immediately is the “softness” of the  $n = 2.5$  potential. This is visible both in panels (a)—where in the anharmonic case the period is longer—and (b) where the closed trajectories in the anharmonic case clearly reach larger displacements in  $x$ . Panel (c) demonstrates the relative strengths of  $F$  as a function of the displacement. It also appears that the initial velocity,  $v_i = 10\text{m/s}$  does not cause a compression significant enough for the Hertz potential to become stronger than a quadratic. As such the sphere always behaves as a soft particle whose softness increases with  $n$ . Note that these results are consistent with expectations from figure 1.2 where  $v_0 = 1$ .

One can perform a quick study on a single particle in an overlap potential well,  $\delta^n$ . In this particular case, a soft particle—barely touching the boundaries—has an initial velocity,  $v_i$ . One can ask various questions such as how does the period of oscillation scale with  $n$  and  $v_i$ ? More importantly, is it possible to obtain a single expression that evaluates  $T = T(n, v_i)$ ? Figure 1.4 shows the decay in period for increasing  $v_i$  as well as the relative increase with  $n$ . The latter should be expected since the “hardness” of the potential is proportional to  $n$ . Because of the excellent fit afforded by a power law, it is suspected that a single formula can describe the solution space. As such we write,

$$T(n, v_i) = A(n)v_i^{-x(n)}, \quad (1.10)$$

where  $A(n), x(n)$  can be fit by some yet-to-be-determined function. It turns out that  $v_i$  decays as simply,  $(n - 2)/n$  while the values comprising  $A$  decay exponentially with a single phase  $\beta$  and plateau at  $\gamma$ . These conclusions, including the fitting functions and associated coefficients are plotted in figure 1.5. This then allows us to write the period of a particle oscillating in an overlap potential of exponent  $n$  with initial velocity  $v_i$  as,

$$T/2 = (\alpha e^{-\beta n} + \gamma)v_i^{-(n-2)/n} \quad (1.11)$$

where the coefficients are identified in the figures and for  $n = 5/2$ ,  $T \propto v^{-1/5}$ .

### 1.4.2 Two-Particle System

Figure 1.6 illustrates the velocity and position phase spaces of the binary system for the first  $120 \mu\text{s}$ . Several points of interest are identified in the velocity phase space—along with their corresponding location in position space—and represent either a zero crossing or occasional extremum. Figure

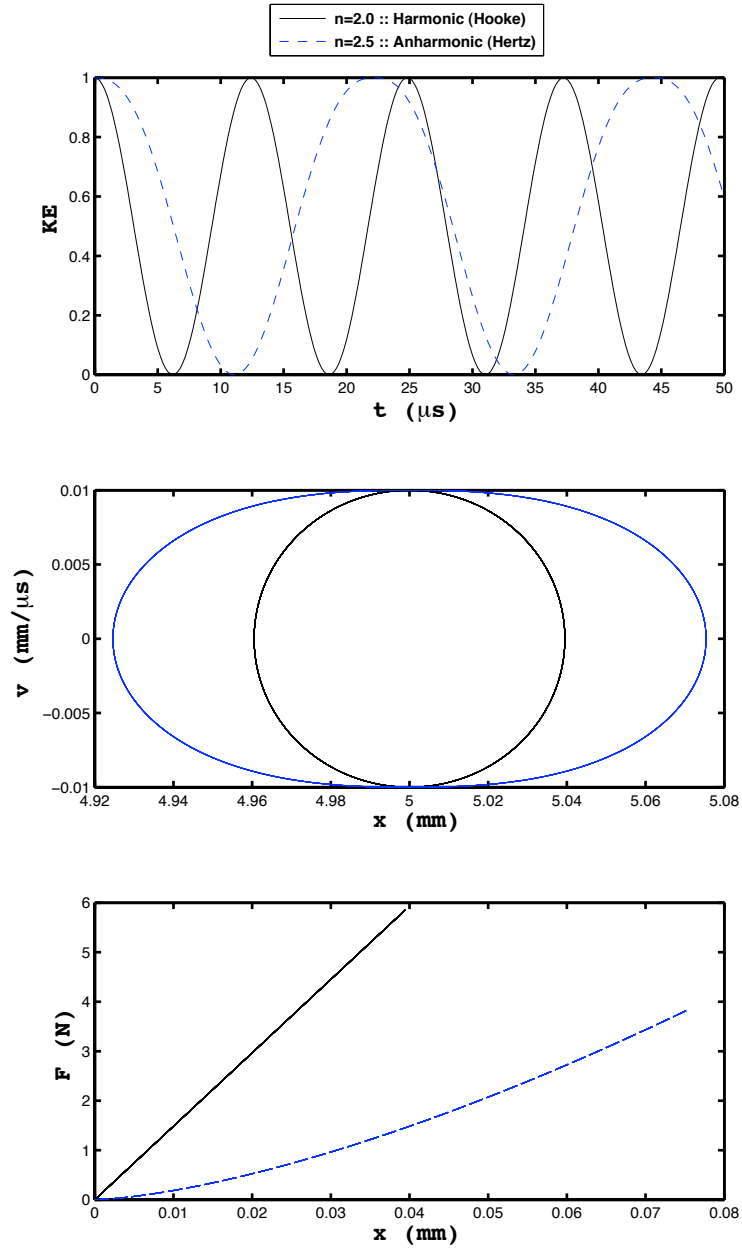


Figure 1.3: Single particle system between fixed compressible walls under harmonic ( $n = 2.0$ ) and anharmonic ( $n = 2.5$ ) potentials (a) normalized kinetic energy, (b) phase space, (c) force versus displacement.

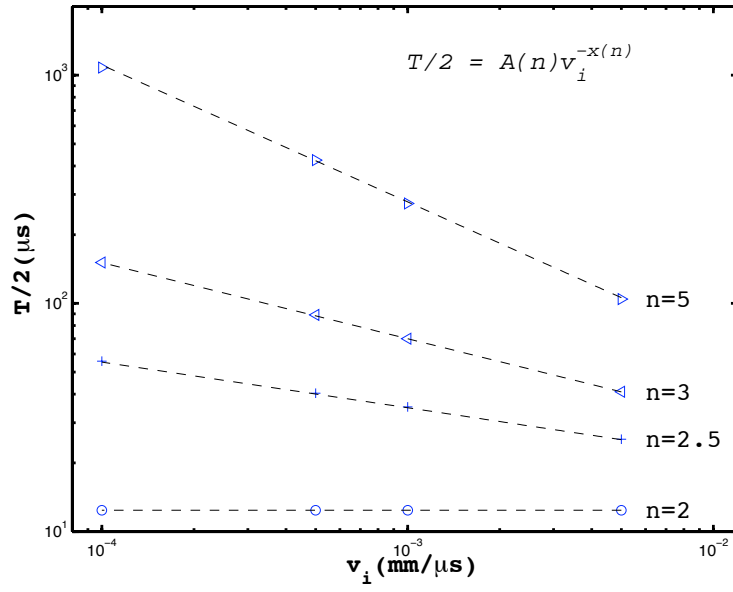


Figure 1.4: Half-periods plotted as a function of  $v_i$  for various values of  $n$ . Each superimposed fit has the form given by  $T/2 = A(n)v_i^{-x(n)}$  (dashed). For each  $n$  the values of  $A, x$  are plotted in Figure 1.5.

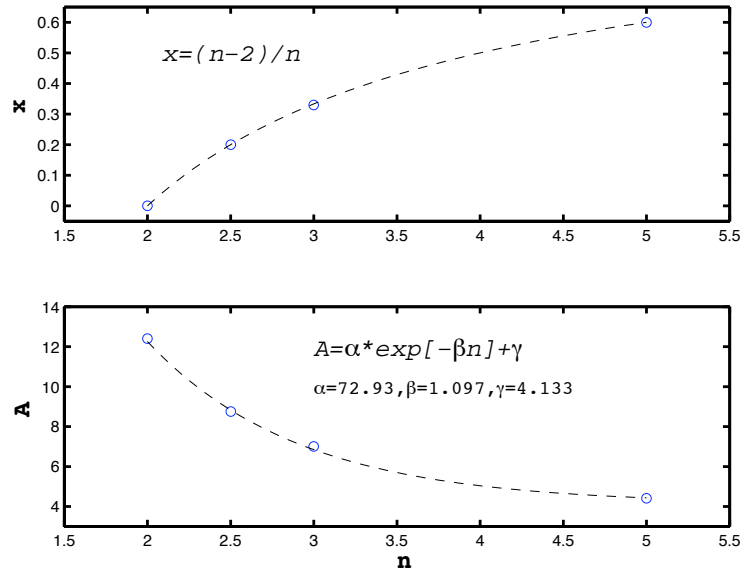


Figure 1.5: Coefficients  $x, A$  from Figure 1.4 plotted vs.  $n$  and fitted with appropriate functions in support of generalized expression for  $T/2$ .

1.7 depicts these points in a cartoon which qualitatively reproduces the velocities, positions, and compression or overlap of the the head and tail particle. Note that negative motion implies movement towards the left of figure 1.7.

It is clear that the dynamics have become much more complex just by adding an additional particle. As one moves from position A to B, the head particle gives up its energy to the tail, becoming maximally compressed at position C in panel (b) — denoted by a zero crossing in panel (a). Nearly vertical and horizontal lines in panel (a) denote one particle accelerating rapidly while the other travels at a small, and nearly constant, velocity. The only way this can happen is if the particles lose contact. That is the overlap vanishes,  $\delta \leq 0$ . These instances are visible in figure 1.8 which plots the overlap as a function of time during the interval seen in Figures 1.6, and 1.7. The ordinate is normalized by 10 mm which is the length of the combined particles' radii. Loss of contact is clearly seen in figure 1.7 for cases G,J, and the start of F. The consequence is momentary faster particle velocities as there is no opposition to the motion.

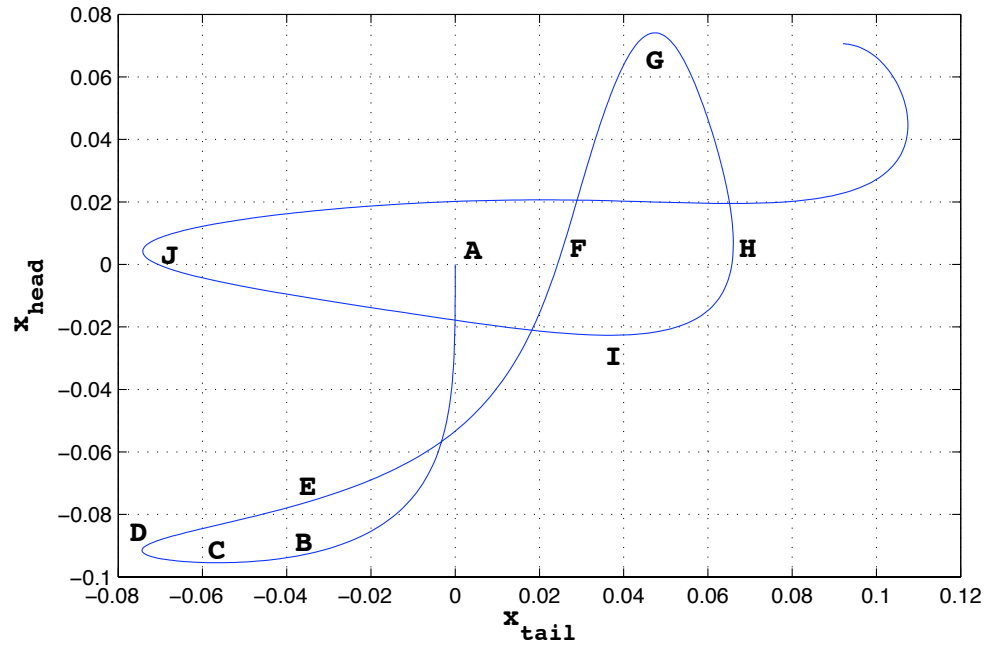
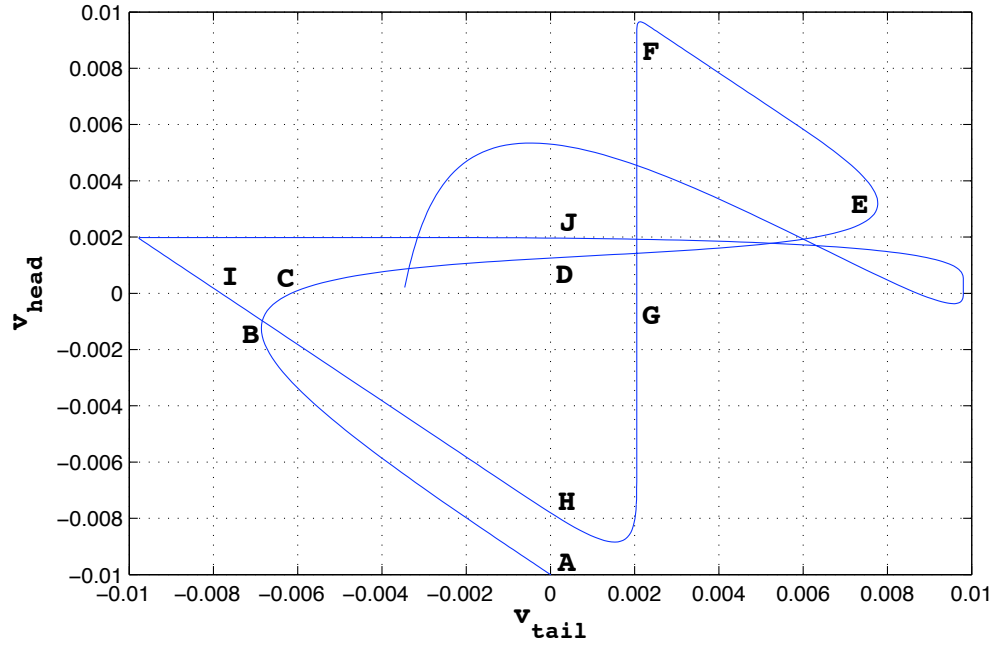


Figure 1.6: Velocity and position phase diagrams for the two particle system. Dynamics are shown for the first  $120 \mu\text{s}$  with corresponding points of interest identified. Note that maximum velocities do not necessarily correspond to crossing the  $t = 0$  positions.

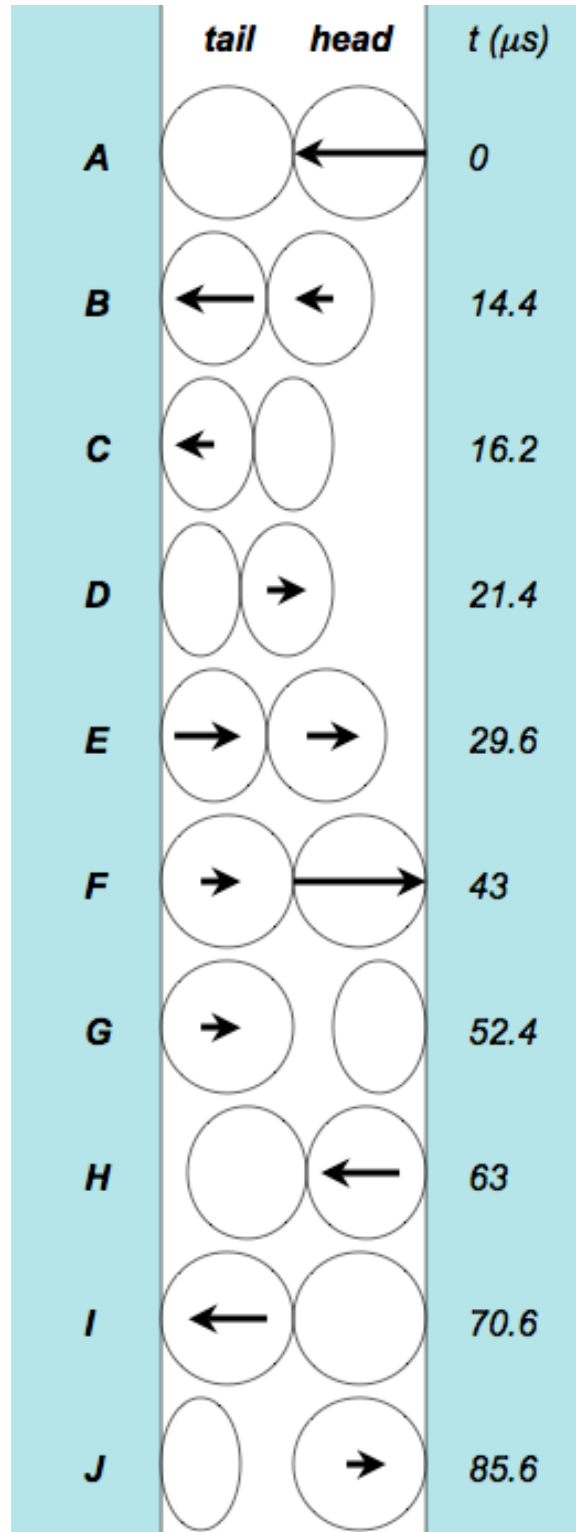


Figure 1.7: Cartoon depicting the evolving two particle system. Refer to figure 1.6 for locations in phase space.

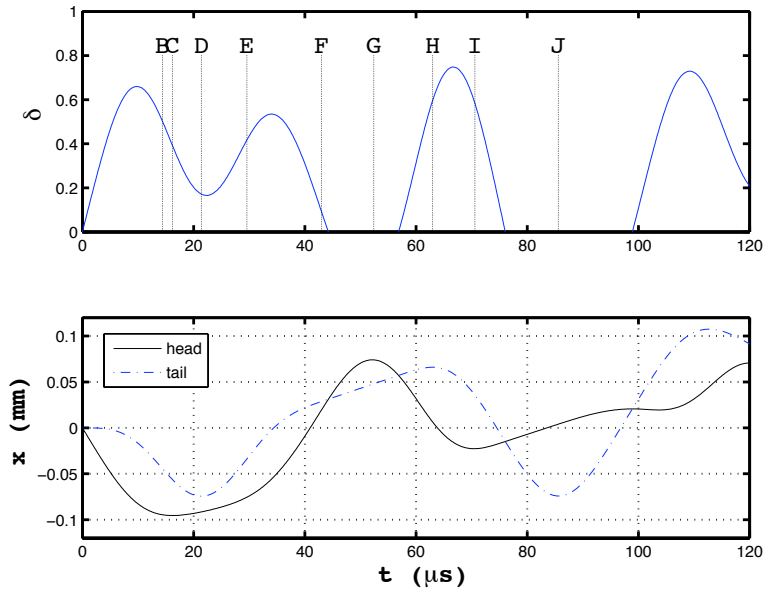


Figure 1.8: Overlap,  $\delta$ , as a function of time for the particle-particle interface in the  $N = 2$  system.  $\delta$  is represented as a percentage of the two spheres combined radii since it is normalized by 10 mm ( $2R_i$ ).



# Chapter 2

## The Simple Tapered Chain (STC)

### 2.1 Introduction

This chapter presents an in-depth and greatly extended study of TCs originally carried out by Pfannes<sup>80</sup>. The results and sections of this chapter were reported by Doney and Sen<sup>25,26</sup> and presented at the 2005 American Physical Society's topical meeting of shock compression in condensed matter in Baltimore, MD. Specifically this work focuses on the ability to spread impulses out in time and space rather than analyzing solitary wave propagation which is typically the dominating topic. Section 2.2 addresses the hard-sphere approximation, with and without a term accounting for energy loss at each collision. Section 2.3 looks at the numeric solution in terms of temporal behavior as well as normalized kinetic energy (KE) and force parameter spaces. That section also includes a discussion of how these systems partition energy. This is followed by a generalization of the systems' characteristic fluctuations and the approach to a state referred to as quasi-equilibrium. The chapter concludes with a mathematical fit to describe the normalized energy mitigation as a function of  $q, \omega$ .

### 2.2 Hard-Sphere Approximation

Hard-sphere approximations differ from the numerically simulated systems in two major ways. The first is that, for the former, the chain is not bounded by fixed rigid walls. As a result, energy will not continue to be transmitted up and down the chain. The second is that the potential becomes infinite ( $n \rightarrow \infty$ ) and as a consequence, the energy packet is only 1 grain in width. The system therefore propagates energy as independent collisions and is congruent to the model proposed by Wu<sup>121</sup>. By generating an iterative form of the conservation equations, one can arrive at an expression for the normalized kinetic energy (KE),  $E_K = KE_{out}/KE_{in}$ . This ratio will be the primary variable determining the absorptive quality of TCs.

The simple tapered chain (STC) is displayed in figure 2.1. To generate an initial disturbance, an input velocity,  $v_i$ , is applied to the rightmost and largest grain with radius  $r_i$ . It propagates to the

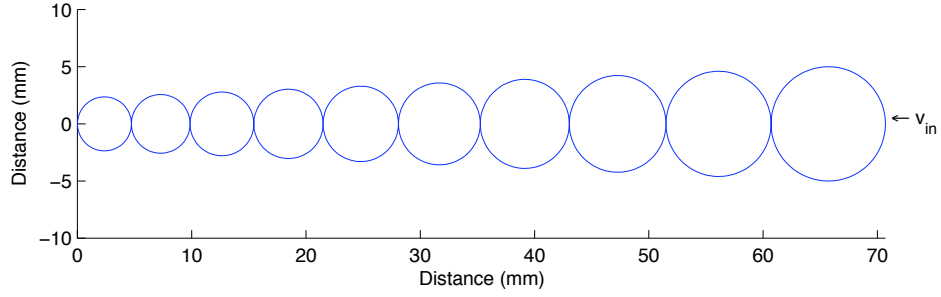


Figure 2.1: Simple tapered chain:  $N = 10$ ,  $q_s = 8\%$ ,  $L = 70.7$  mm,  $r_i = 5$  mm. The rightmost particle is grain  $i$ , its nearest neighbor is,  $i + 1$ , etc.

left, encountering an (initially) stationary grain of radius,  $r_{i+1}$ . The radius of the  $(i + 1)$  particle may be reduced to  $(1 - q)r_i$ . This tapering  $q$  will be constant along the entire length of the chain. During the transmission of the impulse along the chain, there may be energy losses and we consider two cases described in the following subsections.

### 2.2.1 Lossless STC Hard-Sphere Approximation

Ignoring any energy loss during a collision, we perform a STC hard-sphere approximation. Masses and radii are expressed as

$$r_{i+1} = r_i - r_i q_s = (1 - q_s)r_i = \epsilon r_i$$

$$m_i = \rho V_i = \frac{4}{3}\pi r_i^3 \rho = \eta r_i^3 \quad (2.1)$$

$$m_{i+1} = \eta r_{i+1}^3 = \eta \epsilon^3 r_i^3, \quad (2.2)$$

where  $\epsilon = 1 - q_s$ . Evaluating the conservation of momentum, with a single prime denoting post collision values and the initial condition that the  $(i + 1)$  particle is stationary before a collision ( $v_{i+1} = 0$ ), all  $\eta$  cancel and we obtain

$$\begin{aligned} m_i v_i + m_{i+1} v_{i+1} &= m_i v'_i + m_{i+1} v'_{i+1} \\ r_i^3 v_i &= r_i^3 v'_i + \epsilon^3 r_i^3 v'_{i+1} \\ v_i &= v'_i + \epsilon^3 v'_{i+1}, \end{aligned} \quad (2.3)$$

where equations (2.1, 2.2) have been used. Following the same procedure for the conservation of energy while ignoring the factor of one-half yields,

$$v_i^2 = v_i'^2 + \epsilon^3 v_{i+1}'^2. \quad (2.4)$$

Letting  $A = \epsilon^3 v_{i+1}'$  we can rewrite equation (2.3) in terms of  $v_i'$  and substitute the resulting expression into equation (2.4),

$$\begin{aligned} v_i^2 &= (v_i - A)^2 + A v_{i+1}' \\ &= v_i^2 - 2A v_i + A^2 + A v_{i+1}' \\ 2v_i &= A + v_{i+1}' \\ \frac{v_{i+1}'}{v_i} &= \frac{2}{1 + \epsilon^3}. \end{aligned} \quad (2.5)$$

Note that for one collision

$$\begin{aligned} \frac{KE_{out}}{KE_{in}} &= \frac{KE_{i+1}'}{KE_i} = \frac{m_{i+1}}{m_i} \left( \frac{v_{i+1}'}{v_i} \right)^2 = \epsilon^3 \left( \frac{v_{i+1}'}{v_i} \right)^2 \\ &\therefore \frac{KE_{i+1}'}{KE_i} = \frac{4\epsilon^3}{(1 + \epsilon^3)^2}. \end{aligned} \quad (2.6)$$

For  $N$  particles there will be  $N - 1$  collisions, each of which have the ratio in equation (2.6).

Therefore, the normalized KE,  $E_K$ , for the lossless STC hard-sphere approximation is given as

$$E_K = \left\{ \frac{4[1 - q]^3}{(1 + [1 - q]^3)^2} \right\}^{N-1}. \quad (2.7)$$

### 2.2.2 Lossy STC Hard-Sphere Approximation

The same approximation can be performed with some amount of energy loss,  $\tilde{E}_L$ , per collision.

Consequently, the momentum equation (2.3) is unchanged, but equation (2.4) becomes

$$v_i^2 = v_i'^2 + \epsilon^3 v_{i+1}'^2 + \tilde{E}_L. \quad (2.8)$$

One then obtains a more complicated expression replacing equation (2.5):

$$\frac{v'_{i+1}}{v_i} = \frac{2 - \frac{\tilde{E}_L}{\epsilon^3 v_i v'_{i+1}}}{1 + \epsilon^3}. \quad (2.9)$$

We can make the substitution,  $\tilde{E}_L \propto v_i v'_{i+1}$  or  $\tilde{E}_L = E_L v_i v'_{i+1}$ , where  $E_L$  is the constant of proportionality. This adjustment yields

$$\frac{v'_{i+1}}{v_i} = \frac{2\epsilon^3 - E_L}{\epsilon^3(1 + \epsilon^3)}.$$

The corresponding result for the normalized KE for  $N$  particles is

$$E_K = \left\{ \frac{[2(1-q)^3 - E_L]^2}{(1-q)^3 [1 + (1-q)^3]^2} \right\}^{N-1}. \quad (2.10)$$

In the limit  $E_L = 0$ , equation (2.10) reduces to the lossless case, equation (2.7), as one would expect.

Note that results are independent of initial velocity and size of the grains.

### 2.2.3 KE Parameter Space for STC Hard-Spheres

Figure 2.2 highlights the behavior of equation (2.10) for  $0 \leq q \leq 0.1$ ,  $3 \leq N \leq 20$  and selected  $E_L$ . Results indicate a greatly decreasing output of energy for modest values of  $E_L$ . The decay of  $N$  also takes on an exponential decay. Behavior of the tapering,  $q$ , resembles sigmoidal or gaussian decay and approaches linear behavior with decreasing  $N$ . This can be seen in equations (2.7) and (2.10) and is expected since for  $N = 1$  there are no collisions and  $q$  becomes meaningless (it is defined for a particle *and* its neighbor).

Interestingly, if the initial velocity is supplied to the smaller end of the TC, one also observes shock absorption similar to the system in figure 1, albeit with less efficiency. In this case, subsequent particles are growing in size, i.e.,  $r_{i+1} = (1+q)r_i$ . Equations (2.7) and (2.10) are modified accordingly, and the result for a lossless system is illustrated in figure 2.3. Apparently, both configurations mitigate a propagating pulse. Note that the range of axes in the figures are different.

## 2.3 Numeric Solution

Simulations were performed for  $3 \leq N \leq 20$  and  $0 \leq q, \omega \leq 0.1$ .

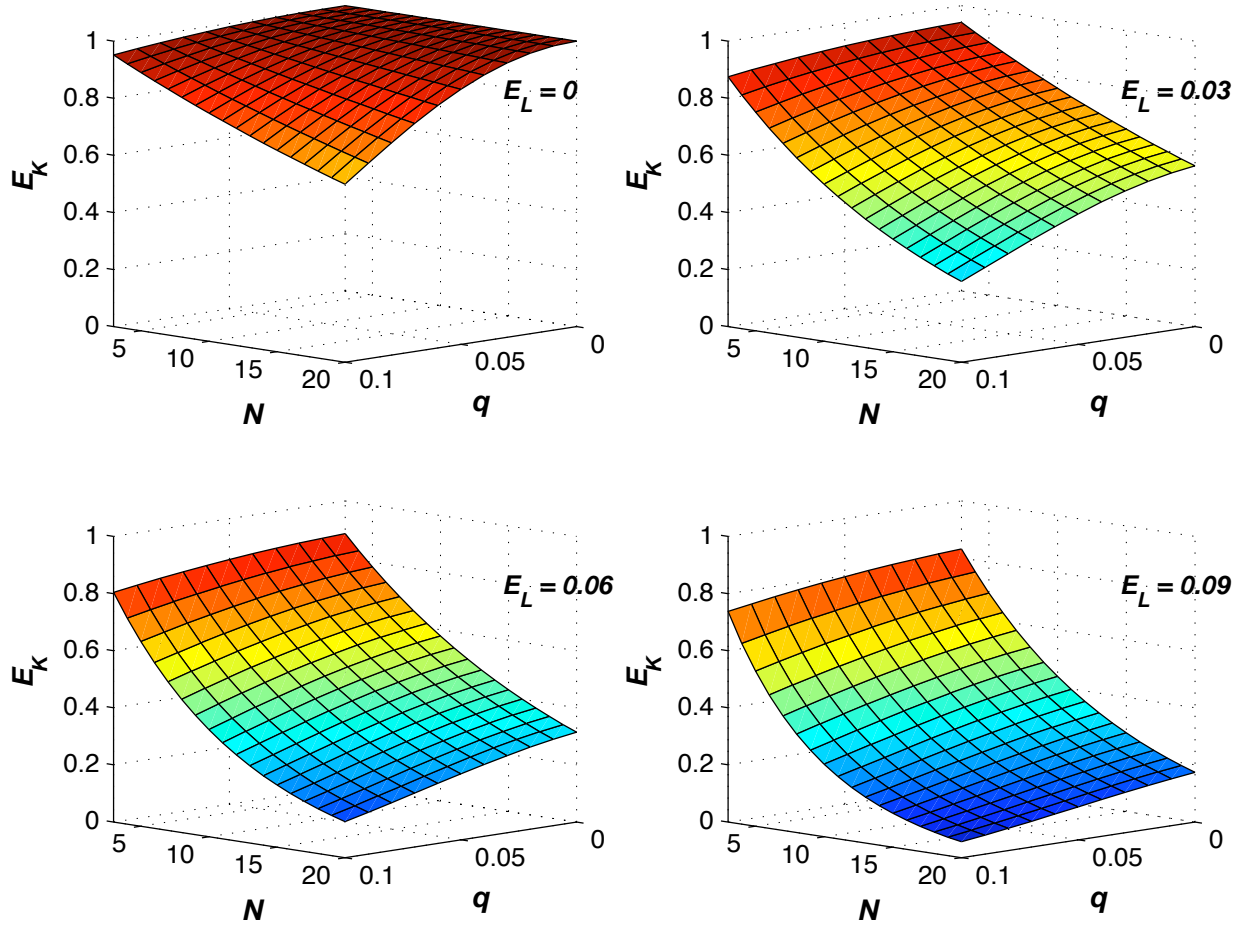


Figure 2.2: Normalized  $E_K(N, q, E_L)$  parameter space for the STC hard-sphere approximation.  $N$  varies from 3 to 20 and  $q$  from 0% to 10%.

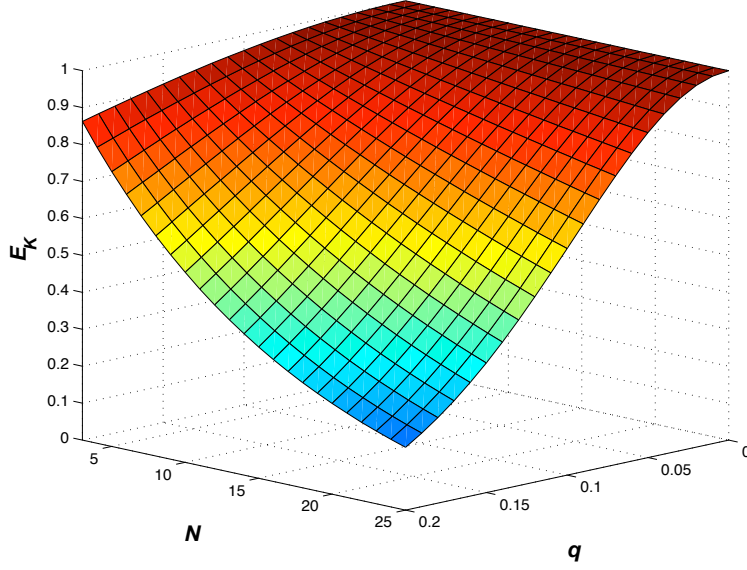


Figure 2.3: Normalized  $E_K(N, q)$  parameter space for the STC hard-sphere approximation where initial velocity is supplied to the smaller end of the chain.

### 2.3.1 Temporal Behavior

Figures 2.4, 2.5 sketch the temporal behavior of the smallest grain for several  $q$  in a STC where  $\omega = 0.05$  and  $N = 15, 20$ , respectively. For clarity, these plots only represent the first half of the total simulation time. Note the decreasing scale of kinetic energy in each underlying panel in both figures. This may initially appear counterintuitive: because KE scales as  $v^2$  and  $m^1$  one might expect it to increase with larger tapering due to the higher velocities. However,  $m \propto r^3 \sim (1 - q)^3$  and this dominates. Width of the peaks — which is related to particle velocities — are functions of  $q$  and  $N$ . As  $q$  increases, the initial peaks are shifted to earlier times so signal transmission is therefore faster. Higher velocities also imply more collisions and therefore that many more restitutive phases.

Note that in both cases, a single, well-defined pulse has been turned into low amplitude noise by increasing the tapering in the system. To better understand the dynamics, we can observe the behavior of several juxtaposed grains near the boundary.

Figure 2.6 highlights the absolute positions, velocities, and kinetic energies for the last five grains (particles 11-15) in a chain. In particular, let us examine the chains represented by the top and bottom subplots of figure 2.4: monodisperse and 10% tapering, respectively. Particle 15 is the last grain and is in contact with the boundary. The subplots on the left represent the monodisperse chain where each grain has  $r = 5$  mm. The right half corresponds to a chain with a tapering of 10% so that particles 11-15 have radii 1.74, 1.57, 1.41, 1.27, and 1.14 mm, respectively. Negative

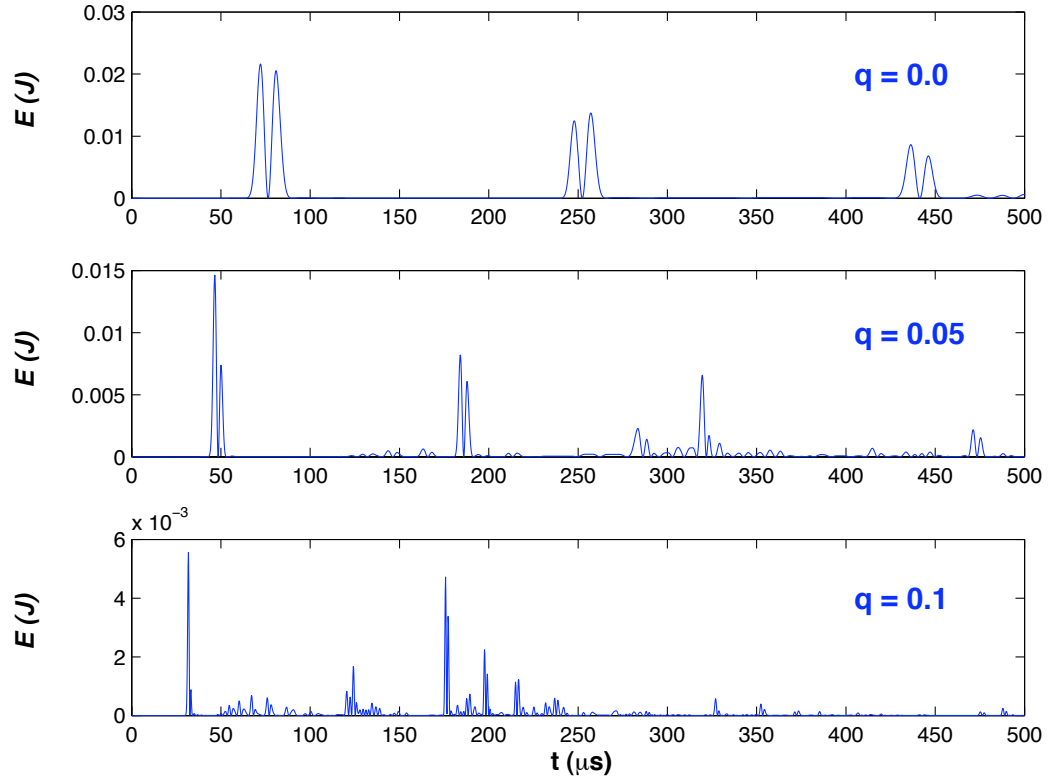


Figure 2.4: KE as a function of time for the smallest particle in a chain with  $N = 15$ ,  $\omega = 0.5$ . Each plot is evaluated for a different tapering with initial kinetic energy as 0.0838 J.

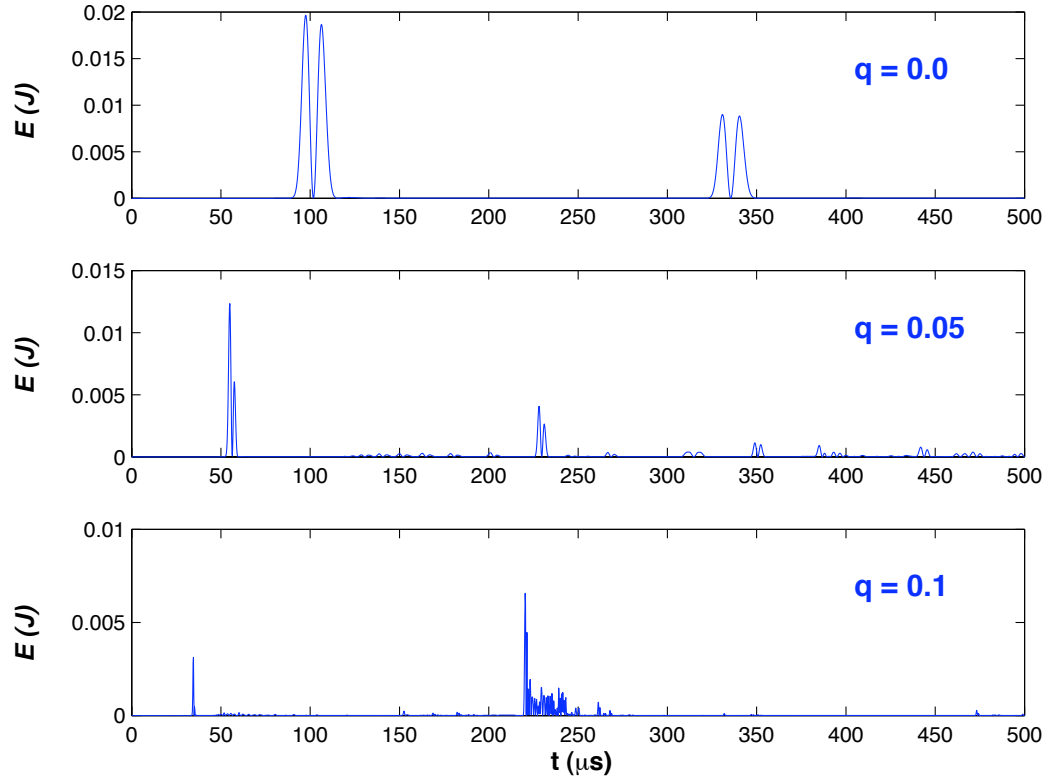


Figure 2.5: KE as a function of time for the smallest particle in a chain with  $N = 20$ ,  $\omega = 0.5$ . Each plot is evaluated for a different tapering with initial kinetic energy as 0.0838 J.



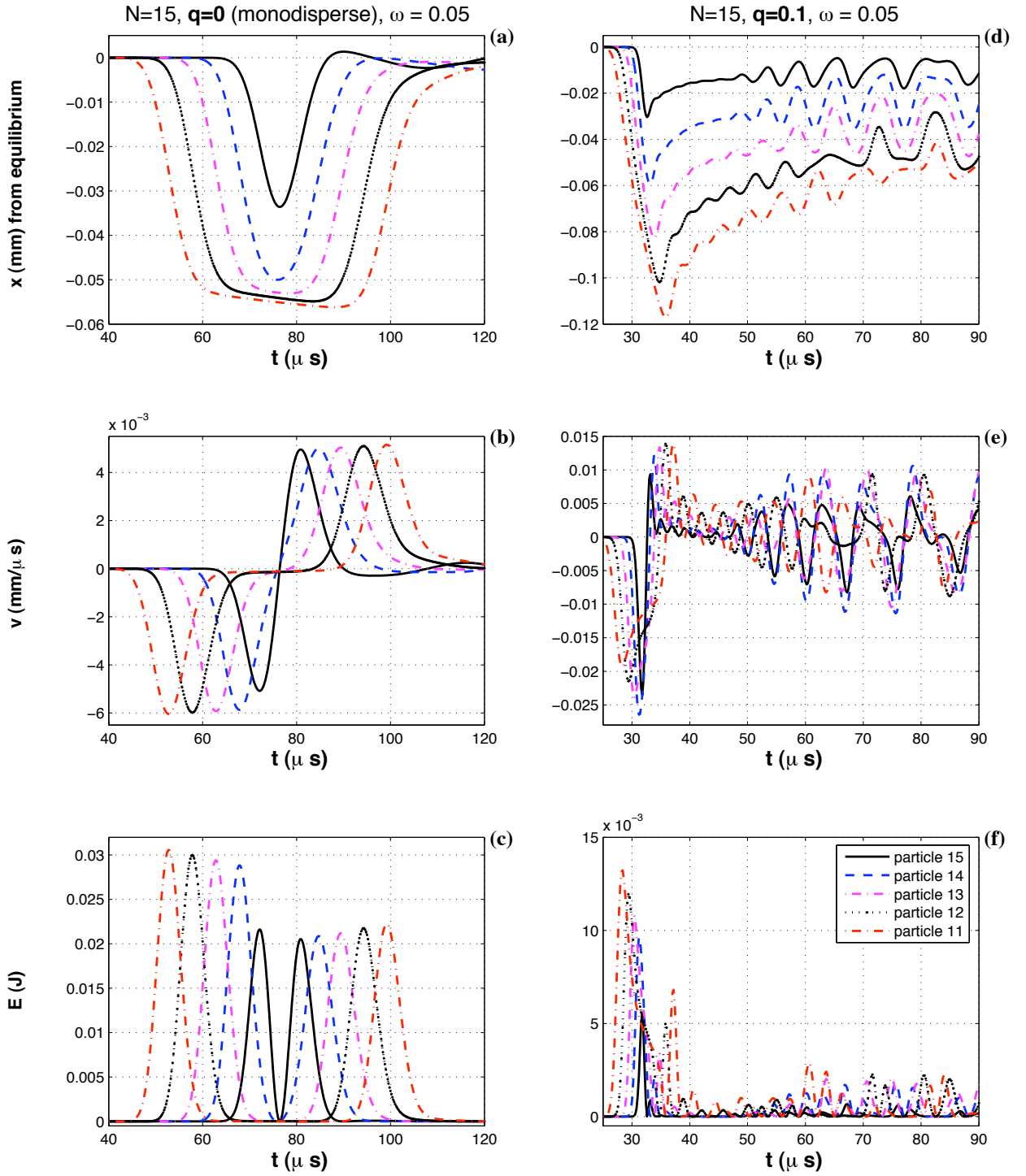


Figure 2.6: Absolute positions, velocities, and kinetic energies for particles 11-15. Particle 15 is the last grain and is in contact with the boundary. The subplots (a-c) represent the monodisperse chain where each grain has  $r = 5$  mm, while (d-f) corresponds to a chain with a tapering of 10% so that particles 11-15 have radii 1.74, 1.57, 1.41, 1.27, and 1.14 mm, respectively. These subplots illustrate when the grains in question first receive the incident impulse. Note the earlier time of arrival for  $q = 0.1$  since velocities are higher (up to a factor of 3 in the plots). For panels (d-f) the dynamics have been extended beyond initial incidence and reflection.

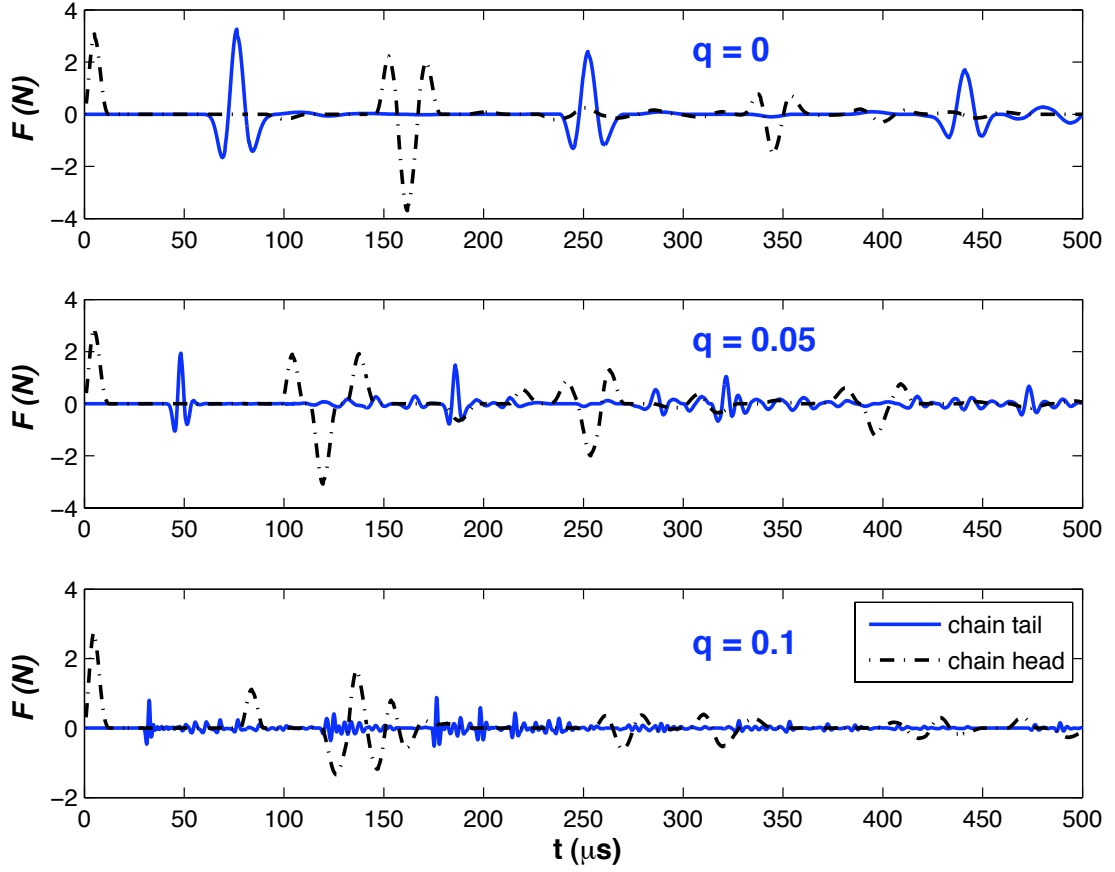


Figure 2.7: Each of the plots depict force as a function of time for the tail and head particles in a chain with  $N = 15$ ,  $\omega = 0.5$ . The value of the tapering increases for successive plots and is denoted by the label  $q$ . Negative forces imply acceleration towards the smaller end of the chain.

velocities and displacement imply motion towards the end of the chain.

For the monodisperse chain, the last five particles first receive and reflect the propagating impulse between 40-120  $\mu\text{s}$ . It also appears that for the monodisperse chain, there is about 5  $\mu\text{s}$  of compression for a given grain before it noticeably responds to the contact force and accelerates away. Observe particle 11 acting upon particle 12 in panel (b) for example. Note that after another 5  $\mu\text{s}$  particle 11 hits its peak velocity which is just about the time particle 13 starts to respond to the impulse.

When looking at the peak KE of particle 13 occurring at 62.5  $\mu\text{s}$ , energy is primarily shared among its two nearest neighbors such that most of the kinetic energy of the system is shared among 3 adjacent particles. The actual number, while still contested, is closer to 5 or 7, since there is a small, but measurable amount of energy in the next layer of nearest neighbors. This is true for any interior particle and is in agreement with Manciu, *et. al.*<sup>59,60</sup>. These solitary waves (SW) — the “envelope” of the five grains in question — represent localized energy that maintain their width yet decrease in amplitude after colliding with a boundary. The decrease of the tail particle’s velocity is a result of the modified potential at the boundary.

At approximately 77  $\mu\text{s}$ , nearly all energy is briefly stored as elastic potential energy. Simultaneously, particles 14 and 15 are maximally displaced from their equilibrium position while particles 11-13 are still slowly compressing towards the boundary. A close examination about this time shows that the fourteenth grain is the first particle to reverse direction due to the restoring force of the last particle. Acceleration plots indicate more clearly that this happens while the tail particle is still being compressed with the boundary.

The big picture of energy propagation then consists of several regimes. In the microscopic sense one could describe the elastic waves emanating from the contact region and reflecting within any particular grain. Mesoscopic features have been the current focus of these plots and observations — that is, bulk motion of a grain. And the macroscopic picture would be the solitary (longitudinal) wave formed by several grains and discussed in previous work.

For the highly tapered chain ( $q = 0.1$ ) on the right hand side of Figure 2.6, the last five particles first receive and reflect the propagating impulse in about half the time as the monodisperse case. As particles 11-14 are accelerated towards the end, their maximum speed increases due to their smaller masses. Particle 11 accelerates at about 25  $\mu\text{s}$  and compresses particle 12 for nearly 2  $\mu\text{s}$  before it starts to move. Shortly thereafter, particle 11 slows down at about 28  $\mu\text{s}$  due to the contact force with its neighbor, particle 12, and additional contact forces with particles 13-15. This is also true for down range particles 12 and 13; however, the accelerations (not pictured) are enhanced as one moves closer to the boundary.

What stands out dramatically in panel (f) is the absence of complete energy transmission. All particles shown have a measurable amount of energy when the tail particle rebounds at about  $32.5 \mu\text{s}$  which is absent in the monodisperse chain. The displacement plot shows all grains biased towards the tail of the chain from the equilibrium position. Each minima corresponds to a maximum in their elastic potential energy. Because these occur at slightly skewed times, subsequent collision-compression oscillations occur which are much more visible in the following  $50 \mu\text{s}$  (not pictured). It is difficult to draw many conclusions from such a complicated landscape. However, it is expected that no solitary wave is present in such chains: the dispersion due to tapering is too great.

When one records the force or energy at the end of the tapered chain with a sensor of some sort, the patterns recorded vary for  $N$  and  $q$  as these plots suggest. As the tapering increases, the pattern changes from a well-defined and periodic pulse to noise. This trend is visible for increasing  $q$  in Figures 2.4, 2.5 and represents the thermalization that we are looking to exploit in various applications.

### 2.3.2 KE and F Parameter Space Behavior

The effectiveness of TCs can be measured based on the normalized kinetic energy  $E_K$  and force surfaces formed by varying  $N$ ,  $q$ , and  $\omega$ , thereby creating many tapered chain configurations. Specifically, we form the ratio,  $E_K = KE_{out}/KE_{in}$ , where  $KE_{out}$  is the first peak felt by the last grain and  $KE_{in}$  is unchanged. Analogously,  $F_{out}$  is the first *minimum* felt by the last grain since the direction of a negative force is into the wall or force sensor. The algorithm to pick out the first turning point for each of these is straightforward. Since  $KE(t)$  is a column vector, one can iterate through each element until the first occurrence of  $(i + 1) < i$  is true. In that case,  $i$  represents the peak. For force we compare against  $(i + 1) > i$ . Actually, normalization is a critical component in determining the effectiveness of TCs and has been given a more thorough discussion in Appendix E.

Figure 2.8 highlights the numerical results for  $KE(N, q, \text{constant } \omega)$ . The gaussian and exponential dependence on  $q$  and  $N$ , respectively stand out immediately. These KE surfaces represent STC chains that thermalize more than half the incident energy introduced into the system. For example, the least effective shock mitigating geometry that we’ve simulated here reduces the output kinetic energy to approximately 40% of the input which is shown in panel (a) where  $N = 3, q = 0$ . The “missing” energy is distributed among the other grains as kinetic and potential. Note that results are independent of initial grain size. For monodisperse chains ( $q = 0$ ), there is asymptotic behavior as  $N$  increases. That is, when  $\omega = 0$  for monodisperse chains, KE becomes a constant. This result

is consistent with observations by Sen, *et. al.*<sup>96</sup> that approximately 15 grains are required for the solitary wave to become fully established. This then propagates indefinitely (in our ideal setup) so that additional particles for  $\omega = q = 0$  have little to no effect. As restitution is adjusted to higher values, the decompressive force is reduced to  $(1 - \omega)\%$  of the compressive force. Consequently, even the monodisperse chains become lossy for increasing  $N$ .

For small chains there are few collisions, so restitutive losses do not play a very big role. The same is true for the amount of tapering. If one holds  $q$  fixed at a small value and increases  $N$ , the chain is *almost* monodisperse. The mismatches are insignificant enough that localized energy can propagate and only over large  $N$  does it break up. This translational symmetry breaking was also reported by and is in agreement with Nakagawa, *et. al.*<sup>72</sup>. Coupled with restitutive losses, the longest and most tapered chains quickly lose energy through the massive number of collisions occurring. As a shock mitigating technology however, one wants to maximize the thermalization even for small chains since there may not be the luxury of large volumes in certain applications (hence the improved chain design presented in chapter 3).

A similar surface can be plotted representing the normalized force for various tapered chains. This is visible in Figure 2.9 and is similar to the corresponding KE plots. Again, the functional form of  $N$  appears as a one or two phase exponential, but the gaussian nature of  $q$  is less obvious and can be approximated linearly throughout the parameter space. In general, the magnitude of  $F_N$  appears to be twice that of  $E_K$ .

The KE numerical results can be compared to the hard sphere approximation by plotting their difference (Figure 2.10). Comparisons that include losses are not evaluated. One difference between the two parameter spaces that stands out occurs for small  $N$ . As one traces out a path along constant  $q = 0$  and increasing  $N$ , the numerical results (Fig. 2.8a) show a quick decrease in  $E_K$  which then approaches an asymptote. We suspect that this is due to the width of input pulse being longer than the distance to the boundary. This does not occur in the hard-sphere approximation since independent collisions preclude that possibility.

### 2.3.3 Energy Partition

The partitioning of energy in a multi-bodied, dynamical system is a helpful tool in understanding the behavior of discrete systems. For instance, it provides a measure of how much of the system is in motion versus its response to the potential. Energy information about the whole TC system can be evaluated by summing the kinetic and potential contributions of each bead. In all cases, we have

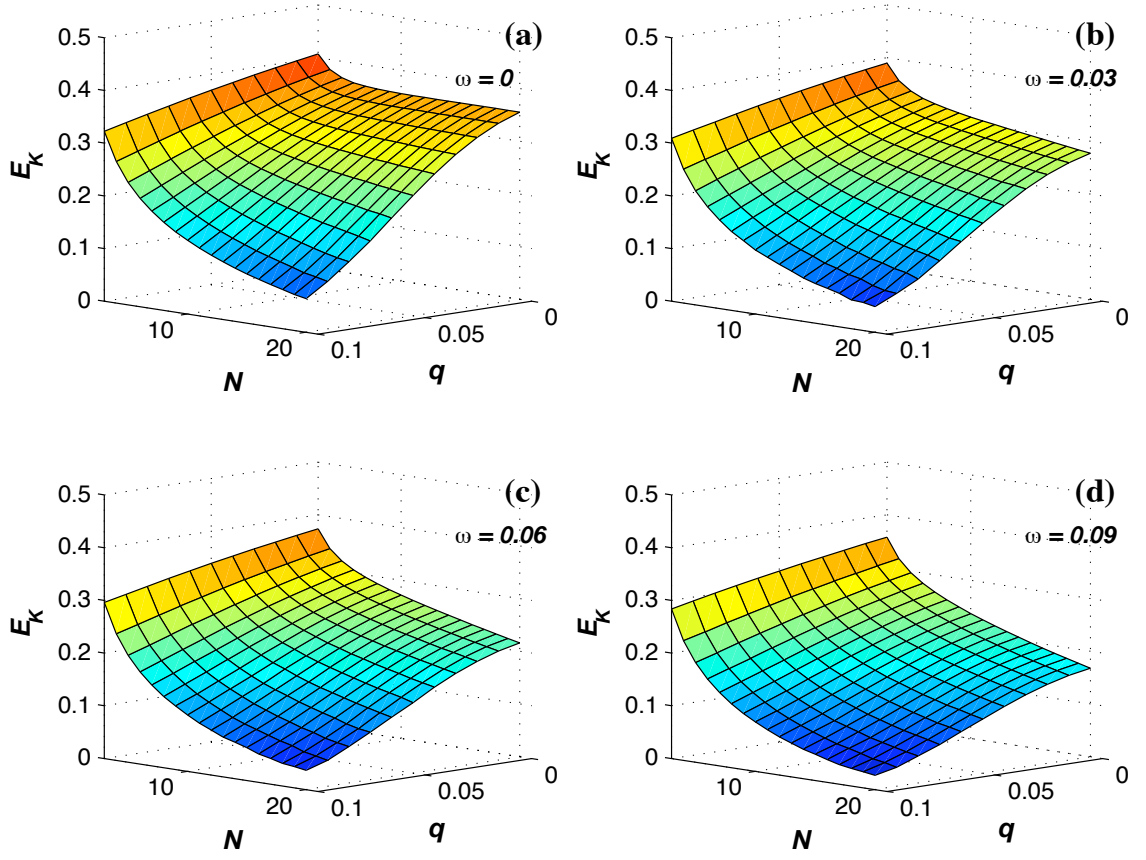


Figure 2.8: Numerical solution of  $E_K(N, q)$  parameter space for constant  $\omega$

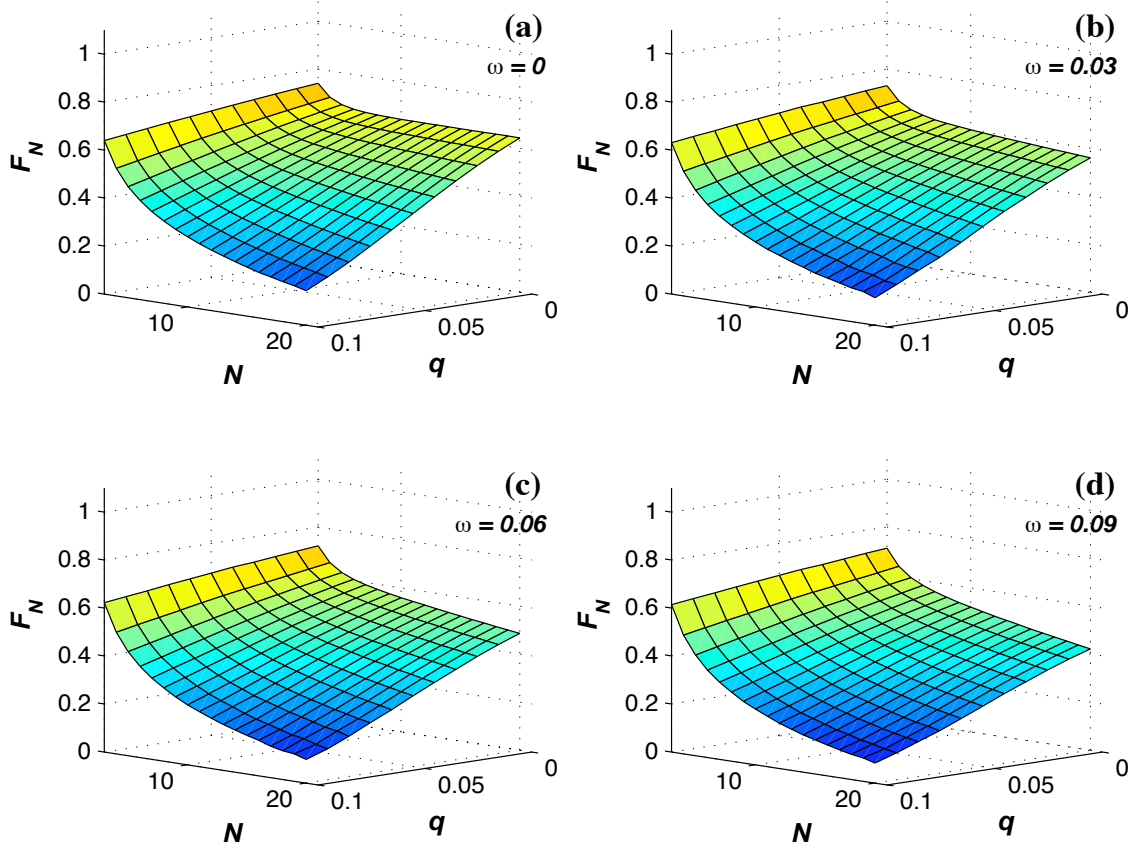


Figure 2.9: Numerical solution of  $F(N, q)$  parameter space for constant  $\omega$

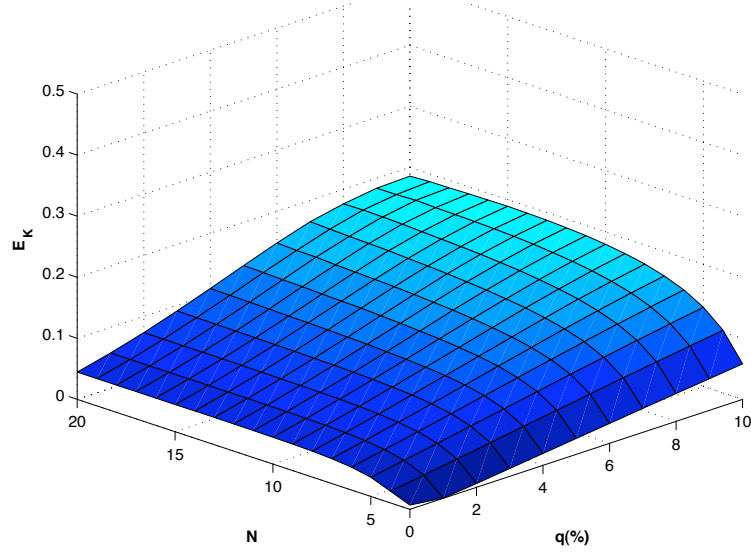


Figure 2.10: Difference plot of the lossless KE parameter spaces for the hard-sphere approximation (Figure 2.2a) and numerical solution (Figure 2.8a). Note that the azimuthal view has been rotated 180 degrees for clarity.

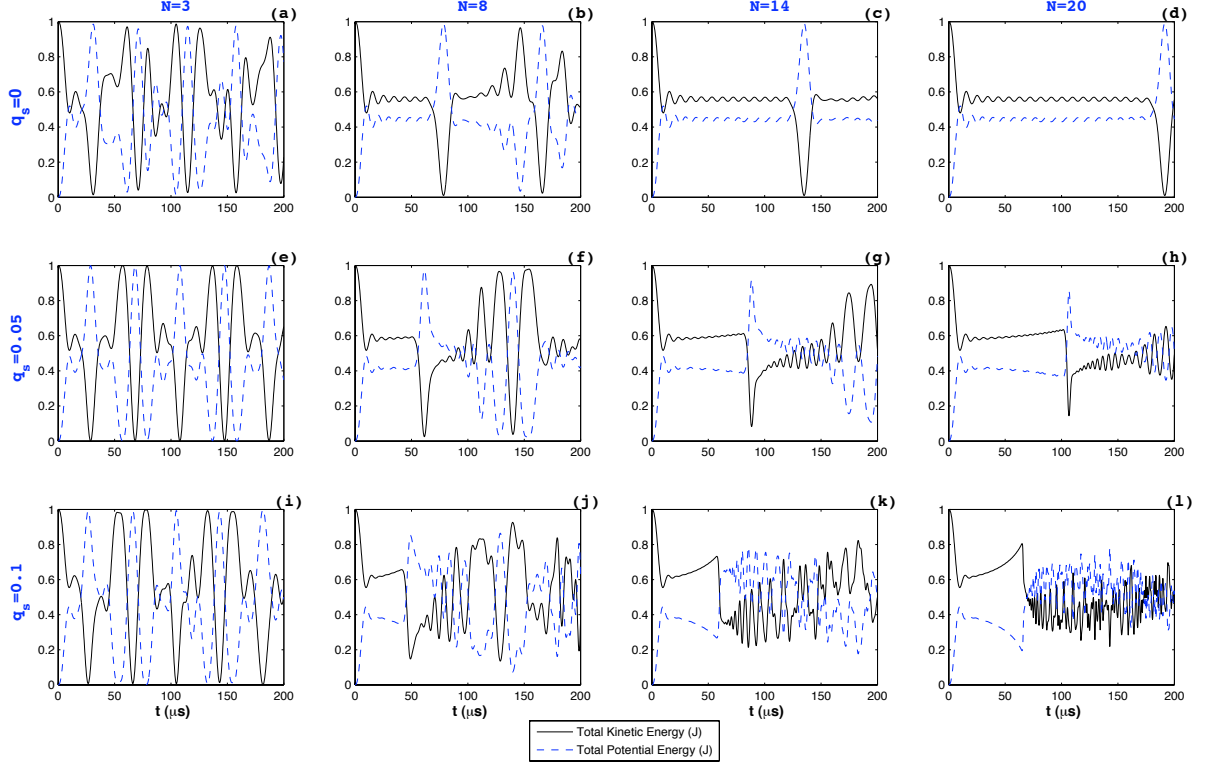


Figure 2.11: Energy partitioning for STCs where  $N = \{3, 8, 14, 20\}$  represents the number of spheres and  $q_s = \{0.0, 0.05, 0.1\}$  is the tapering. Noisy plots resembling panel  $l$  indicate shock absorbing systems while those similar to panel  $j$  transmits an impulse as a solitary wave — essentially without loss. Panels  $a$ - $c$  represent efficient energy conversion systems.

seen that energy sharing among particles is rapid and remains nonlocalized. Here attention is paid to the energetic response of the system with some consideration to individual particle velocities. Note that  $q$  is now being written as  $q_s$  to distinguish it from results that will be presented in Chapter 3. Therefore  $q = q_s$  represents the tapering in a STC.

Energy partitioning in the STC is displayed as twelve subplots in figure 2.11 where each plot element represents a chain with  $N = \{3, 8, 14, 20\}$  and  $q_s = \{0, 0.05, 0.1\}$ . For clarity, only the first fifth of simulation time is shown. Many interesting features, visible in the plots, can be discussed qualitatively where it appears that simple chains can be loosely categorized into three energy regimes: solitary wave systems (small  $q_s$ , large  $N$ ), shock absorption systems (large  $q_s$ , large  $N$ ), and strongly oscillating systems (small  $N$ ). For smaller systems, it is still unclear how exactly the system behaves when the width of the solitary wave,  $w_s$ , is smaller than the size of the system,  $N$ .

The simplest case to consider is that of panel (d) as it has been presented before<sup>80</sup> and represents a monodisperse chain of 20 grains. It is clear in this instance that energy is partitioned into 55-57%



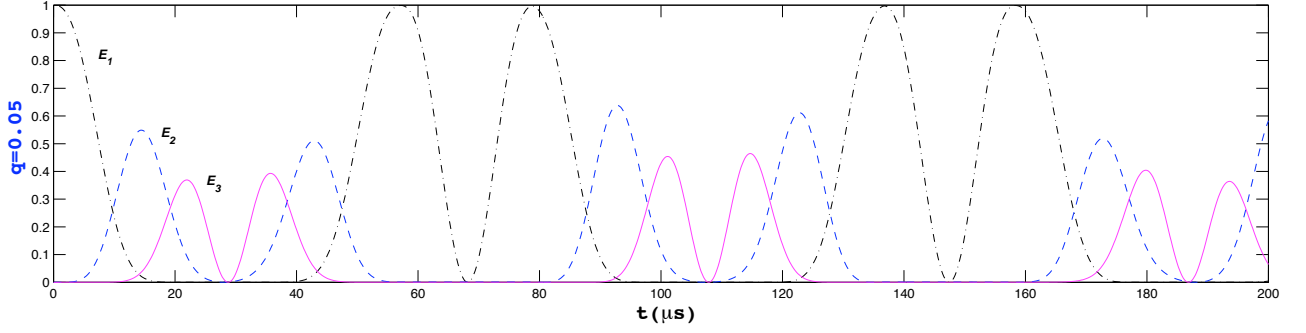


Figure 2.12: Normalized KE for  $N = 3, q_s = 0.05$ .  $E_1$  represents the head of the chain and input;  $E_2$  is the central bead; and  $E_3$  is the tail. Note the periodicity of the system resulting in a recurrence time of just under  $80 \mu s$ .

kinetic and 45-43% potential. An inspection of grain speeds reveal that the first several particles retain some residual velocity before a SW can form — which also holds true for every plot in the figure.

Holding  $N = 14$  fixed and increasing  $q_s$  results in faster particles as one moves down the chain as well as wave broadening. This is visible in panels (g,h,k,l) as an increasing ramp whose slope is steeper with increasing  $q_s$  and smoothening of the sinusoidal modulations, respectively. Compare this with the wave broadening among multiple grains with increasing  $q_s$  seen in figure 2.13. Interaction with the boundary follows and in some cases, the energy envelope increases because most particles have already reversed direction. Close inspection reveals that trailing particles can catch up and kick leading particles into higher energy states. In panels (k,l) rapid oscillations, or thermalization, is visible. This is an indication of increasing “randomness”<sup>111,119</sup> of motion and spreading of the energy in time and space — a prerequisite for impulse decimation.

As one moves to shorter chains, where  $w_s > N$  like those in panels (a,e,i), nearly complete conversion of energy frequently takes place. Wave reflection therefore has begun before full transmission of the incident pulse would normally reach the boundary of a longer chain. Increasing  $q_s$  for  $N = 3$  appears to enhance the energy conversion efficiency. In fact, panel (b) is particularly alluring given its quasi-periodicity. Amplitude of the intermediate weak peaks vary based on  $q_s$  and represent energy transfer through the center bead. This behavior throughout the simulation suggests the possibility of nonlinear modes<sup>115</sup>. Figure 2.12 provides a glimpse into future work on the subject where the normalized KE of each particle is superimposed as a function of time. The recurrence time — or period of the system,  $\tau$  — is just under  $80 \mu s$ , and decreases slightly with every cycle. It’s not clear whether there exists a critical value  $q_c$  that admits a constant recurrence time. Increased values of  $q_s$  tend to attenuate  $E_1$ . Note also the lack of equipartition for this system.

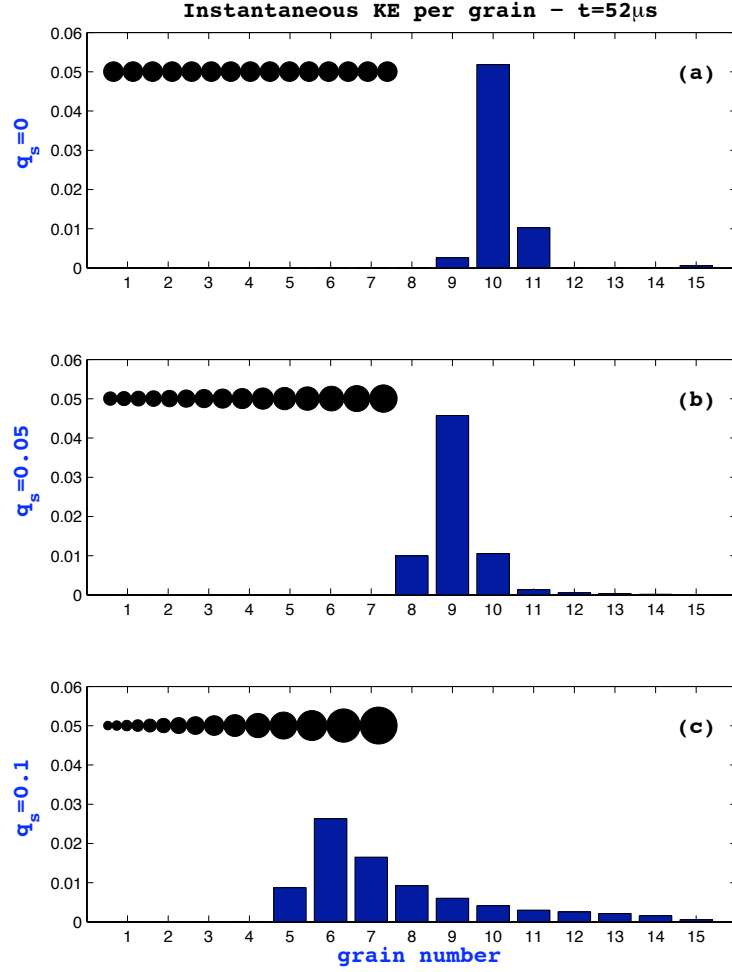


Figure 2.13: Instantaneous kinetic energy per grain for  $N = 15, t = 52 \mu s$  and selected tapering.

Additionally, one can take a mesoscopic view and investigate how STC systems break down the energy per grain. Observe figure 2.13 where the instantaneous kinetic energy is plotted per grain for  $N = 15, t = 52 \mu s$  and a selection of tapering values. In these plots, the incident impulse moves from right to left. Panel (a) represents the monodisperse chain and the localization of energy is apparent as the SW is constructed. Why does it take so many particles before a SW is constructed? Note from Figures 2.11(b-d) that it takes a finite amount of time — or equivalently, distance — for the system to partition energy according to the virial theorem (see section 2.3.4) which for  $n = 2.5$  implies  $\langle KE \rangle = 0.55$ . This means that even for inertially matched spheres, some residual energy is left at the head of the chain. Panels (b,c) again illustrates the effect of tapering which spreads the energy out among grains. For the latter, the distribution before interacting with a boundary appears geometric. It is clear that a SW cannot exist in such chains because of the large dispersion.

An even more illuminating series of images can be generated which shows the energy landscape for all particles in the chain at all points in time. This is illustrated in figure 2.14. This series of plots highlights the propagation of a pulse in time (horizontal axis) through the chain of grains (numbered vertically) for several values of tapering,  $q_s = \{0, 0.02, 0.04, 0.06, 0.08, 0.1\}$ . In each case,  $N = 20$ . Kinetic energy is displayed and has been magnified several times in order to pick out the smaller amplitude backscattering and wave phenomena. For the monodisperse chain, one can clearly see the SW propagate, with negligible loss and backscattering for these early times. It is easy to see that the SW velocity is approximately,  $1 \text{ mm}/\mu\text{s}$ , this is in contrast to the delta function impulse in grain number 20 of  $10 \text{ mm}/\mu\text{s}$  — recall that some residual energy is left over in the first several grains. This velocity decreases ever so slightly per cycle as the SW is destroyed and recreated imperfectly<sup>99</sup> at the boundaries. As  $q$  increases, trapped energy is seen by the light horizontal bars in panels (e,f) preceding  $100 \mu\text{s}$ . What's also very interesting to note here is the increasing magnitude of backscattering during the return phase to particle 20. With increasing  $q$ , energy transfer is hindered during the momentum transfer. Starting with panel (d) at  $100 \mu\text{s}$ , many subsequent waves of lower velocity towards the head of the chain are visible. At  $500 \mu\text{s}$ , organized waves emerge that only propagate through the smaller half of the chain (top half of panels). This effect also occurs for larger  $q$  in panels (e,f) but more quickly — after the first interaction with the boundary. In these last panels, the emergence of organized additional wave motion was unexpected.

### 2.3.4 The Approach to Quasi-equilibrium

What is the equilibrium state for a nonlinear system? For that matter, what is it for a strongly nonlinear system with no restoring terms such as the Hertz potential? These questions have been addressed by previous researchers with emphasis on FPU systems as discussed in section 1.2.2. Here we outline an approach that leads to an interesting state referred to as quasi-equilibrium (qeq) where the system exhibits some traits of being in equilibrium. It is found that (1) the eventual state of the system appears to be initial condition dependent — this is opposite the expectation of an equilibrium state; (2) the distribution of velocities of the system is roughly a gaussian - so a maxwellian distribution of velocities is found — this is expected in an equilibrium phase; (3) TC systems appear to have sustained fluctuations that deviate significantly from equilibrium.

## Velocity Distributions

For a dilute gas in equilibrium, constituent particles exhibit a maxwellian (or gaussian) velocity distribution<sup>84</sup>. One can therefore measure whether a similar system has reached equilibrium by binning the velocities of each particle and observing whether the profile is that of a gaussian — as figures 2.15, 2.16 do for  $N = 4, 20$ , respectively. In these panels, there are 50 bins ranging from  $-0.01$  to  $0.01$  mm/ $\mu$ s where the vertical axes represents the count per bin. Note that each panel automatically adjusts the number of counts. In both cases, particle 1 represents the end of the chain and particle  $N$  represents the head where the initial impulse was applied. In addition, simulation time was extensive: 10 ms. For earlier times, the profiles differed markedly from a gaussian. The plots show that with fewer particles, it is more common to find higher velocities, that is they don't decay significantly. For large  $N$  however, velocities decay to the point of a super-abundance near the mean value — note the large increase of counts. It was expected that boundary particles would stand-out in their profiles; however, interior and boundary particles appear indistinguishable in this representation. Something that is missing from these plots is the temporal dependence — that is, how long does it take to reach such profiles?

## Equipartition

The next issue that can be addressed is whether or not one has equipartition of energy. The virial theorem<sup>37,47,103</sup> describes the average kinetic and potential energy in a system. If the force can be derived from a potential of degree,  $n$ , then the virial theorem becomes,

$$\begin{aligned} \frac{1}{2}n < PE > &= < KE > \\ < KE > &= \frac{n}{(n+2)} \end{aligned} \quad (2.11)$$

where the normalized total energy,  $E = 1 = < KE > + < PE >$ , has been used to eliminate  $< PE >$ . This is the expected mean value of KE *for the system*. Note that  $n = 2$  is the only case where the energy is equally divided between potential and kinetic. Thus, in the strictest sense of the word, equipartition has been achieved. One can compare results from the simulation to these expectations. Figure 2.17 illustrates the average KE as a function of  $N$  for several values of  $n$ . It should not be surprising that  $< KE >$  is independent of  $N$  since it has no explicit dependence in the Hamiltonian. Figure 2.23 demonstrates that the simulational results agree with what one would expect from equation (2.11).

If equation (2.11) is equally distributed to each particle in the system, then for a system approaching equilibrium one might expect

$$\langle KE \rangle_n = \frac{n/(n+2)}{N}, \quad (2.12)$$

per particle. These values are measured in figures 2.19, 2.20, and 2.21 at 100, 500, and 1000  $\mu s$ , respectively. Each plot represents a matrix of subplots for several STCs where  $N = \{3, 8, 14, 20\}$  and  $q = \{0, 0.05, 0.1\}$ . The horizontal axis in each panel represents the specific grain and the vertical is the normalized energy. The red line indicates the theoretical expectation given in equation (2.12). As the sequence is observed in time between the figures, it is clear that short chains with large  $q$  do not equally divide energy (recall figure 2.12) as described by equation (2.12). Even for extended times, longer chains do not always reach this limit either — particularly for grains adjacent to the boundary and  $q = 0.05$  for example.

## Fluctuations

The mean value of KE alone doesn't say much about the system. It is therefore of interest to measure the fluctuations about this mean and their decay with increasing  $N$ . The evaluation of fluctuations however, is usually reserved for large systems. While the STCs we are considering only have up to  $N = 100$  particles, it is the number of timesteps in the simulation that is actually being considered; and that quantity is large with 50000 elements.

The fluctuations represent a nearly continuous value (dictated by the size of the time step),  $F(t) = KE(t) - \langle KE \rangle$ . To keep the value positive definite it is written as,  $F(t) = \sqrt{(KE(t) - \langle KE \rangle)^2}$  and figure 2.22 illustrates the results for several chains:  $F(t, n, N = 100, q = 0)$ . For increasing  $n$  it appears that the mean value of the fluctuations,  $\langle F \rangle$ , is growing. In addition, the time to reach the boundary is increasing which is denoted by the peaks. The latter observation suggests that the spheres become increasingly *soft* with  $n$  which is counterintuitive since one obtains the hard-sphere approximation as  $n \rightarrow \infty$ . What is happening? The answer lies in Figure 1.3(c). Recall that this figure plots the force versus position, or compression, for a single grain in the  $n = 2, 2.5$  potentials. Note that the displacement isn't large enough such that the Hertz force overtakes the Hookean-like force. As a result, for increasing  $n$ , the potentials become increasingly soft — as Figure 1.1 indicates — for small displacements (i.e. those less than 1). That is the reason why for increasing  $n$ , interactions appear softer even though theoretically, one is approaching the hard-sphere limit —

recall figure 1.2. The mean value of the fluctuations can be calculated by the following,

$$\langle F \rangle = \sum_{i=\Delta t}^{N_{\Delta t}} \frac{F_i(t)}{N_{\Delta t}}$$

where  $F_i(t)$  is the instantaneous value of  $F$ ,  $\Delta t = 0.2\mu\text{s}$  is the timestep, and  $N_{\Delta t} = 50000$  is the number of timesteps.

One would expect the fluctuations to approach zero as  $N$  tends to infinity<sup>47</sup> since there are more particles to distribute the energy over with increasingly smaller changes about the mean. The current data however, indicates that this may not be the case for overlap potentials. It is found that  $\langle F \rangle$  plateaus at a value that is a function of  $n$  — see for example figure 2.23(a). Specifically, for  $n = 2$  and  $n = 2.5$  differences between data is small when one looks at  $\langle F \rangle$  and it was found that in both cases,  $\langle F \rangle$  is about the same and decreasing in  $N$ . Thus, the distinction in whether or not  $\langle F \rangle \rightarrow 0$  is hard to make when  $n = 2$  and  $n = 2.5$ . It is pretty clear however that when  $n > 2.5$ ,  $\langle F \rangle$  appears to stabilize. Thus, these systems seem to have sustained fluctuations that deviate significantly from equilibrium. The reason why this happens is because the solitary waves that carry energy span several particles and their width is controlled by  $n$ . Thus, any two particles don't quite carry the same energy on average at any given time. It was believed then that when  $q > 0$ ,  $\langle F \rangle$  would approach zero since one is forcing thermalization by breaking down the solitary waves. This is not quite so however and it remains a topic for future investigation.

In order to characterize how  $F$  changes, one can measure  $\langle F \rangle$  as a function of  $n$ . Therefore, figure 2.23(a) plots the decay of  $\langle F \rangle = \langle F(n, N) \rangle$ . Each set of data appears to follow a function of the form,

$$\langle F \rangle = A(n)e^{-k(n)N} + B(n), \quad (2.13)$$

where Prism<sup>71</sup> has been used for the nonlinear regression analysis in determining the values of  $A, B, k$  for each  $n$ . Here,  $A$  represents the maximum amplitude above the saturation  $B$  while  $k$  governs the phase (or half-life) of the exponential decay. Note based on the trend in the data, this model doesn't allow  $\langle F \rangle \rightarrow 0$  in the limit of  $N \rightarrow \infty$ . Instead it saturates at  $B$ . It is possible though for  $B \rightarrow 0$ ; however  $N$  isn't sufficiently large for that to potentially occur. For  $n = 2, 2.5$ ,  $\langle F \rangle$  appears to continue to drop, although our maximum value of  $N$  would need to be increased to prove this assertion. For the range in data however, equation (2.13) fits the data well.

To obtain expressions for how the parameters  $A, B, k$  vary as functions of  $n$ , they have been plotted in figure 2.23(b-d). In panel (b),  $k$  appears scattered and independent of  $n$ . For simplicity,

we therefore will use its mean value,  $\langle k \rangle \sim 0.3$ . Panels (b,c) however, appear to follow an exponential decay with plateau and sigmoid, respectively. With the coefficients selected by Prism as a best fit with narrow 95% confidence intervals, the relations are given as,

$$\begin{aligned} A(n) &= 0.2052e^{-0.1898n} + 0.04246 \\ B(n) &= -0.07877 + \frac{0.1563 + 0.07877}{1 + \exp[(3.673 - n)/2.216]}. \end{aligned} \quad (2.14)$$

What's interesting is that  $A(n = 2)$  and  $B(n = 2)$  are not represented well by the fit as seen in panels (c,d). This is odd considering that, in regard to  $B$ , the data points along the plateau in panel (a) for  $n = 2, 2.5$  are nearly identical. When equations (2.14) and  $\langle k(n) \rangle = 0.3$  are combined with equation (2.13) one obtains a full expression for the decay in fluctuations as functions of  $n$  and  $N$ . The results are plotted in Figure 2.24 where values for  $n = 2$  have been excluded since they fall outside the model's applicability ( $n \geq 2.5, 1 \leq N \leq 100$ ). The data is well-fitted by the model and allows one to interpolate the fluctuations in the average KE of a system governed by the overlap potential,  $\delta^n$ , for various  $n$  and  $N$ . Because the initial condition of  $v_i = 10\text{m/s}$  only compresses grains such that larger  $n$  leads to softer grains, it would be useful to expand (2.13) to take into account  $v_i$ . Note that the values of  $F(t)$  have been obtained over very long simulation time,  $10^4\mu\text{s}$ , yet the fluctuations about  $\langle KE \rangle$  of the system remain measureable.

### Quasi-equilibrium

For an isolated system to be in equilibrium it implies that dynamic properties of that system do not change with time<sup>107</sup>. Take for example  $\langle KE \rangle$ , it was seen in the previous section that while some systems may reach a generalized or mixed equipartition, their mean values of  $\langle KE \rangle$  still fluctuate in time quite considerably. This was quantified in equation (2.13). An equilibrium state would require the fluctuations to vanish, yet we observe them to saturate at a nonzero value even over long simulation times. When one additionally takes into account that STC chains have gaussian velocity distributions, it seems that such systems display some properties of equilibrium, but not all of them. This curious state is referred to as quasi-equilibrium (qeq) and is a very recent discovery<sup>69,99,100</sup>.

One way to characterize this state is to measure the relaxation time to qeq. With increasing  $N$ , energy spreads out and consequently so do the maximum velocities. Rather than looking at the velocity distributions per grain therefore, we can record the absolute maximum velocity,  $|v_{max}|$  of any grain in a chain per timestep—or over some interval of timesteps—and plot that as a function of time. This is illustrated in figure 2.25 which plots  $|v_{max}|$  as a function of time for  $N = 16, 18, 20, 50$ .

Note that when the velocities decay, they saturate to some value. The relaxation time to qeq,  $\tau_{qeq}$ , therefore, is when that saturation occurs with negligible change over time. Characterization of the time is difficult however because it is calculated from a fitting function based on data which has a significant amount of scatter. In a first attempt to measure,  $\tau_{qeq}$ , the results proved inconclusive as the energy relaxation of the system needs to be better characterized as to reduce the amount of scatter. What follows is a description of the technique which will form the basis of future work on the subject.

The decay can be fitted to a Gaussian whose peak or mean is centered on  $t = 0$  such that the fitting function is

$$Y = A + Be^{\left[\frac{1}{2}\left(\frac{t}{\sigma}\right)^2\right]}, \quad (2.15)$$

where  $A, B, \sigma$  are variables to be fit (by Prism); however in each attempt, very poor residuals were obtained due to the large scatter in the data. The fit appeared accurate for  $N = 18, 20$ ; however it was less than certain for  $N = 16, 50$ . In particular, for  $N = 16$ , there is only a small difference in  $t = 0, 10000$  values — the chain could be too short for such measurement.

When a fit is established, one can measure  $\tau_{qeq}$  by measuring the difference in subsequent elements in the  $v_{max}$  vector. When that value drops below a certain threshold, the remaining differences are negligible and the system has reached qeq. This is expressed as,  $v_{max}(i+1) - v_{max}(i) \leq v_c$  and based on the plot of these differences as a function of time (not pictured), one can chose  $v_c = 1 \cdot 10^{-7}$  mm/ $\mu$ s. Results were strongly dependent of the determination of  $\sigma$  as well as the interval of timesteps over which values of  $v_{max}$  were selected.

Is there a minimum  $N$  for which qeq requires? What is the role of  $n$ ? Can the relaxation time,  $\tau_{qeq}$  be written in terms of these variables? Are these results based on our attempts to characterize qeq using solid, liquid, or gas equilibrium conditions — recall that granular materials exhibits phenomenology of multiple states of matter. Does the stabilization of  $\langle F \rangle$  for  $n > 2.5$  imply a sufficiently good hard-sphere model? It is clear that much work still needs to be done investigating this topic.



## 2.4 Mathematical fit of KE parameter space

Coming back to shock mitigation capability, a mathematical fit for the  $KE = KE(\omega, q, N \gtrsim 10)$  parameter space is proposed and has the form:

$$E_K(\omega, q) = A e^{Bq^C} e^{D\omega^E} \quad (2.16)$$

which corresponds to a two-dimensional Weibull distribution. Due to the gaussian and exponential natures of  $q$  and  $\omega$ , respectively, the form in equation (2.16) then is well suited when the exponents are restricted to  $C > 1$  and  $E \leq 1$ . For simplicity we set  $E = 1$  and  $C = 3/2$ . The coefficients  $B$  and  $D$  were evaluated using 4th order polynomial fits and the scaling coefficient  $A$  is essentially the point  $E_K(N, \omega = q = 0)$ . It turns out that a second order fit was not sufficiently robust and a higher order fit yielded marginal gains at the cost of mathematical encumbrance.

Additionally, this model currently lacks the rigor sufficient for planar behavior in the limit of small  $N$ . It is unclear at this point if  $N$  can be completely decoupled from  $\omega$  and  $q$  and written as an additional exponential modification. In all likelihood, the coefficients  $B$  and  $D$  would be written as functions of  $N$ .

In evaluating the fits, it was found that  $KE(\omega, q, N = 20)$  is described quite well by:

$$E_K(\omega, q) = 0.35544 \cdot e^{[-1.5055 \cdot 10^{-5} q^4 + 4.016 \cdot 10^{-4} q^3 - 3.981 \cdot 10^{-3} q^2 + 0.0147 q - 0.05435] q^{3/2}} \cdot e^{[4.144 \cdot 10^{-5} q^4 + 1.955 \cdot 10^{-3} q^3 - 0.03962 q^2 + 0.02887 q - 8.341] \omega} \quad (2.17)$$

It is compelling to rewrite (2.17) in the more suggestive form:

$$E_K(\omega, q) \sim e^{\alpha q^{11/2}} e^{\beta q^{9/2}} e^{\gamma q^{7/2}} e^{\delta q^{5/2}} e^{\epsilon q^{3/2}} \dots \quad (2.18)$$

$$\sim e^{\alpha q^{(n+3)}} e^{\beta q^{(n+2)}} e^{\gamma q^{(n+1)}} e^{\delta q^n} e^{\epsilon q^{(n-1)}} \dots \quad (2.19)$$

where the powers of  $q$  have been adjusted to be written as a series in  $n$ . The occurrence of an apparent series in  $n$  is quite striking. Note that in (2.17) for increasing strength of  $q$ , the coefficients decrease by orders of magnitude. These weaker weightings are mandatory since they are arguments in the exponential and decay of KE would occur too quickly were their value too high. Additionally, note the mixed term  $q\omega$  in (2.17). This is indicative of a many-body effect: one cannot have restitution in a single particle chain since, by definition, it requires at least two to evaluate the loading and unloading.

Figure 2.26 compares the numerical results and the model for the case of  $N = 20$ . The results are practically indistinguishable except for the minor timestep errors in the simulation which lead to the roughness in the difference plot for large  $q$ . For this large value of  $N$  and  $q$ , the tail particle is rather small and has a large velocity. The time step is such that kinetic energy plots lose their accuracy because the algorithm picking the 1st peak is seeing less smoothness in the  $\text{KE}(t)$  space. As such, the model provides a better assessment for the state of the system.

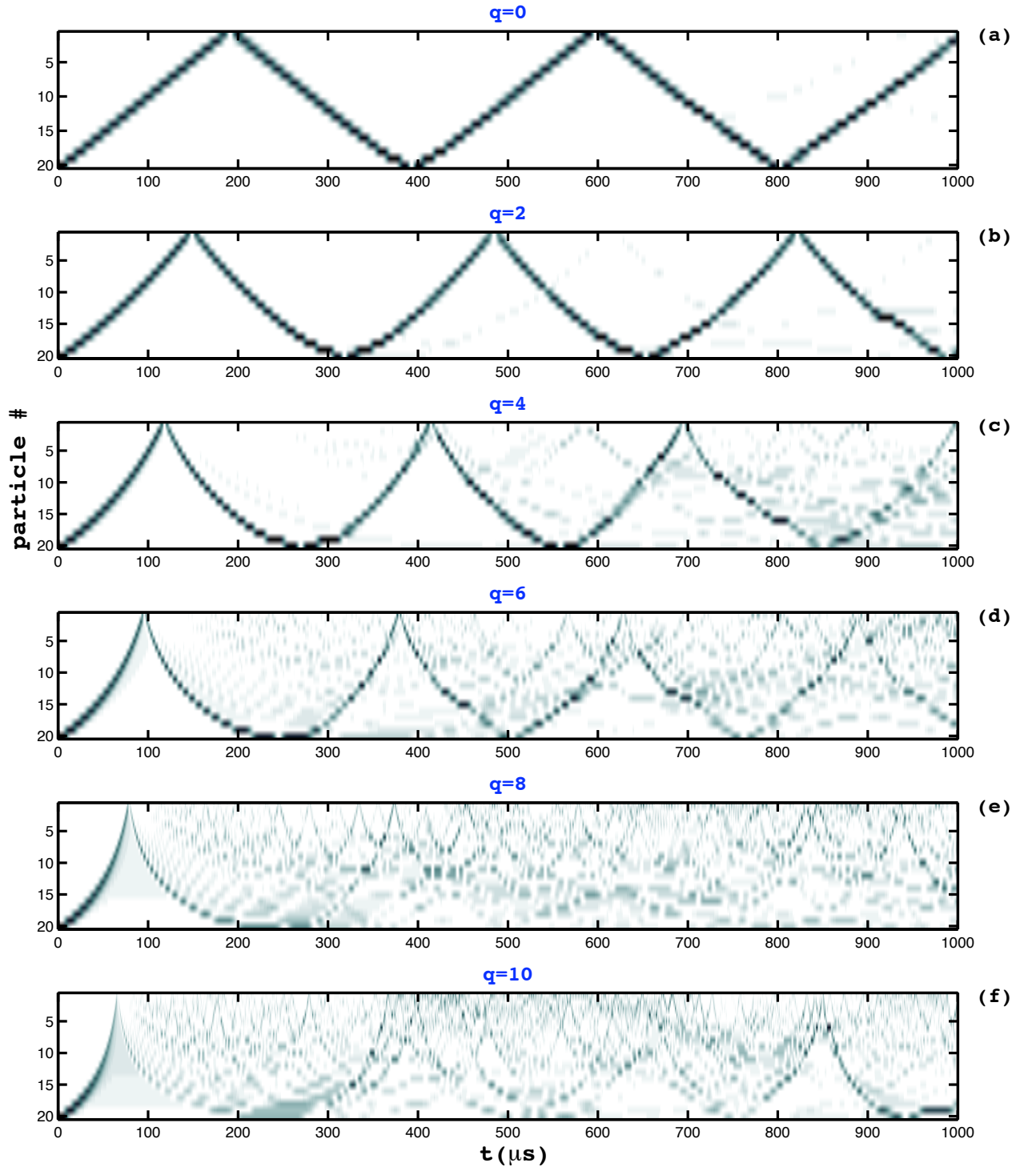


Figure 2.14: Normalized kinetic energy landscape. Vertical axes represents the particle id while the horizontal axis is time out to  $1000 \mu s$ .

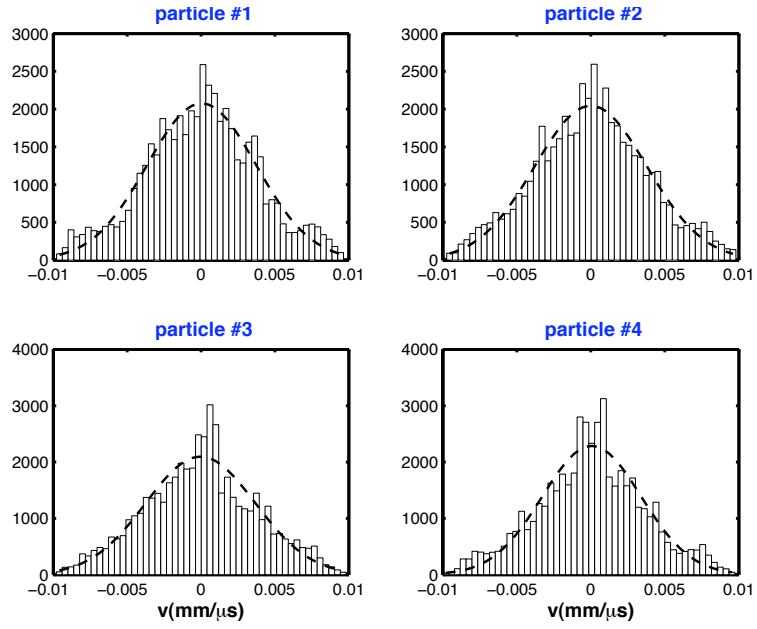


Figure 2.15: Velocity distribution with superimposed Gaussian fit for each particle in a STC with  $N = 4, q = 0$ . Particle 1 represents the end of the chain and particle 4 represents the head where the initial impulse was applied.

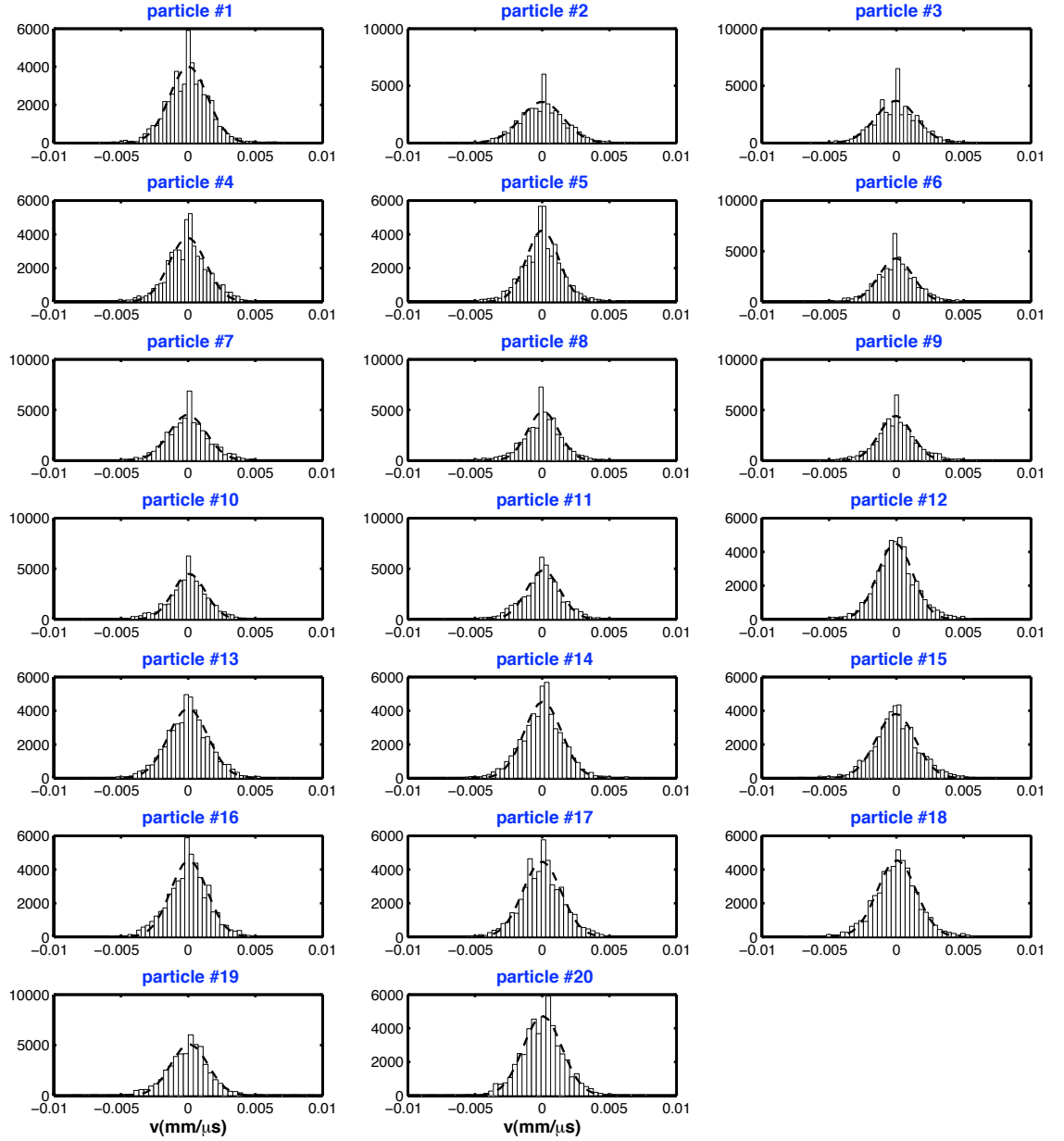


Figure 2.16: Velocity distribution with superimposed Gaussian fit for each particle in a STC with  $N = 20, q = 0$ . Particle 1 represents the end of the chain and particle 20 represents the head where the initial impulse was applied.

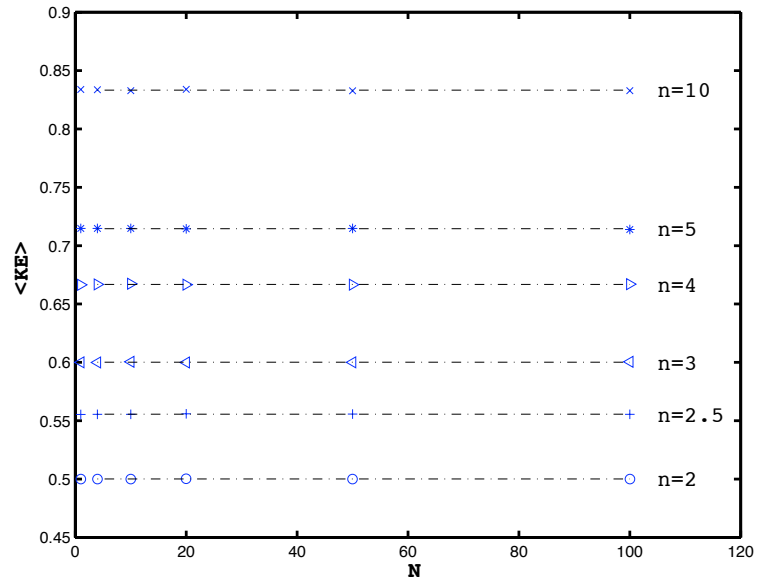


Figure 2.17: Average kinetic energy of the system as a function of  $n$  and  $N$ .

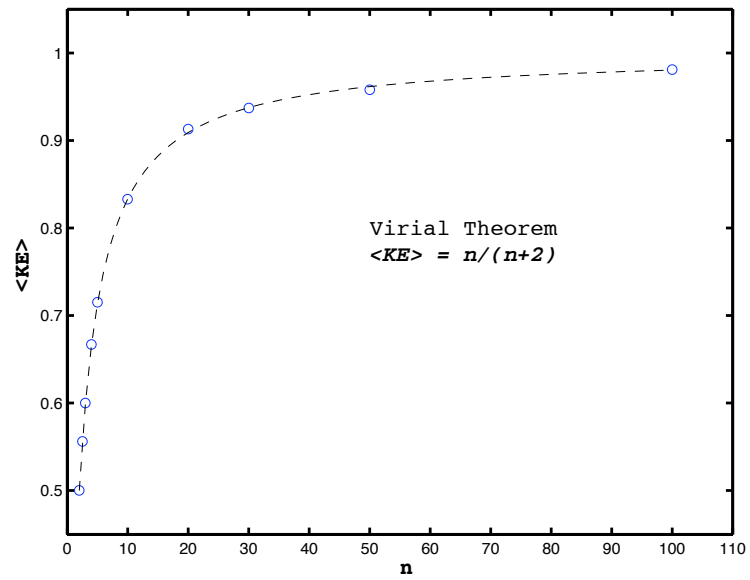


Figure 2.18: Average kinetic energy of the system determined from simulation (circles) and theoretical expectation by the Virial Theorem (dashed).

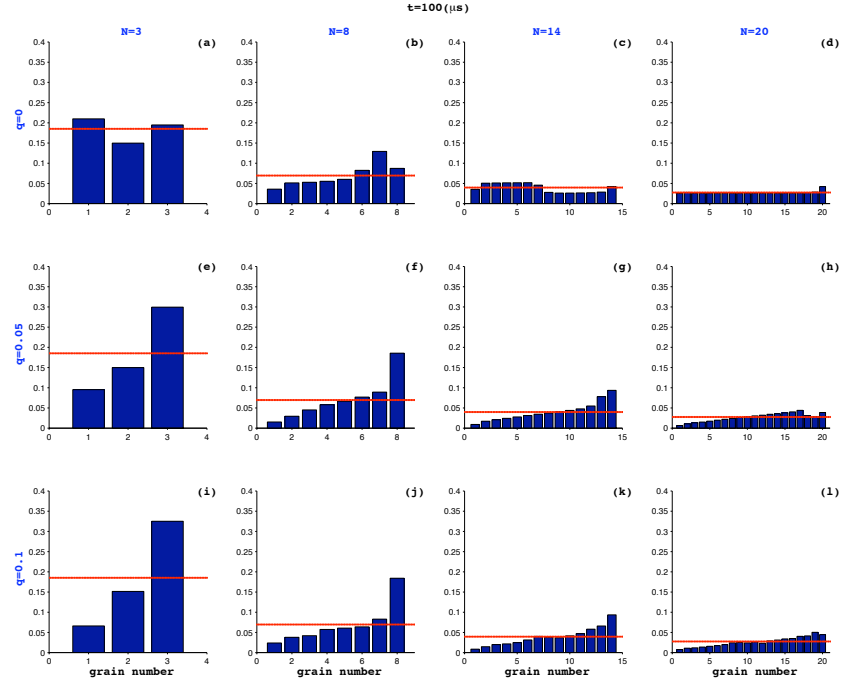


Figure 2.19: Partition of energy by grain number for several STCs where  $N = \{3, 8, 14, 20\}$  and  $q = \{0, 0.05, 0.1\}$  at  $t = 100\mu s$ . The red line indicates the theoretical expectation that  $\langle KE_n \rangle = \frac{n/(n+2)}{N}$ .

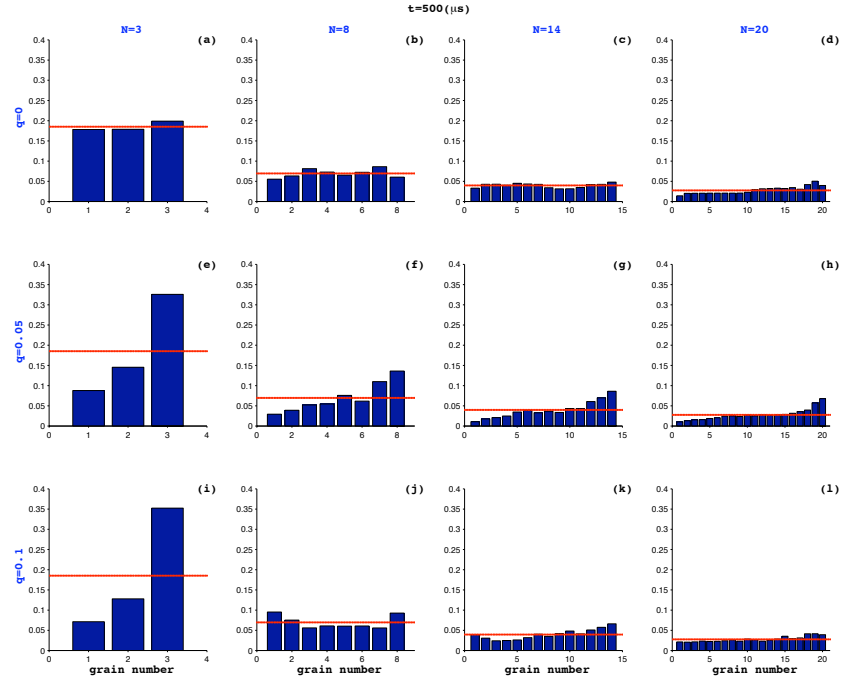


Figure 2.20: Partition of energy by grain number for several STCs where  $N = \{3, 8, 14, 20\}$  and  $q = \{0, 0.05, 0.1\}$  at  $t = 500\mu s$ . The red line indicates the theoretical expectation that  $\langle KE_n \rangle = \frac{n/(n+2)}{N}$ .

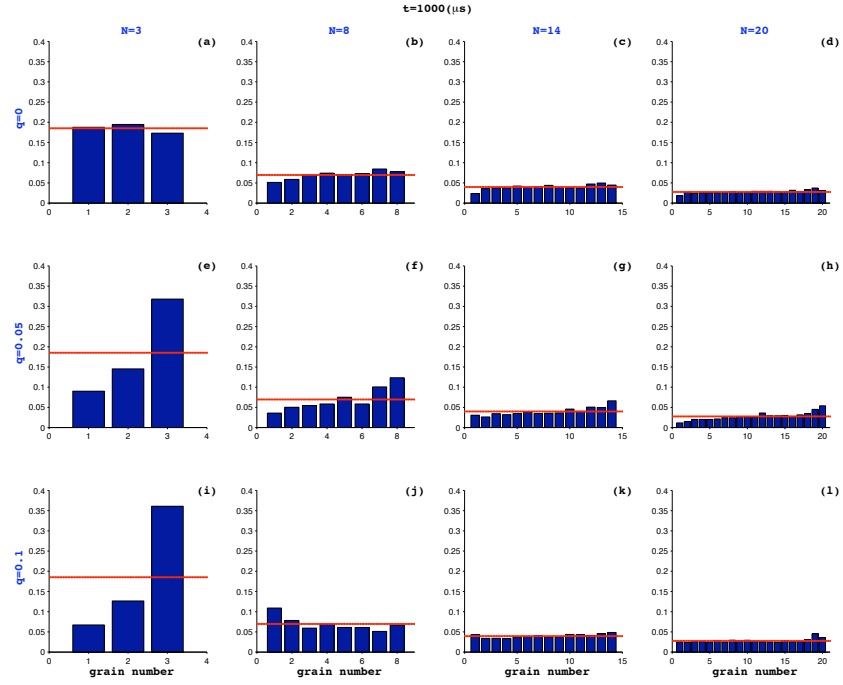


Figure 2.21: Partition of energy by grain number for several STCs where  $N = \{3, 8, 14, 20\}$  and  $q = \{0, 0.05, 0.1\}$  at  $t = 1000 \mu s$ . The red line indicates the theoretical expectation that  $\langle KE_n \rangle = \frac{n/(n+2)}{N}$ .



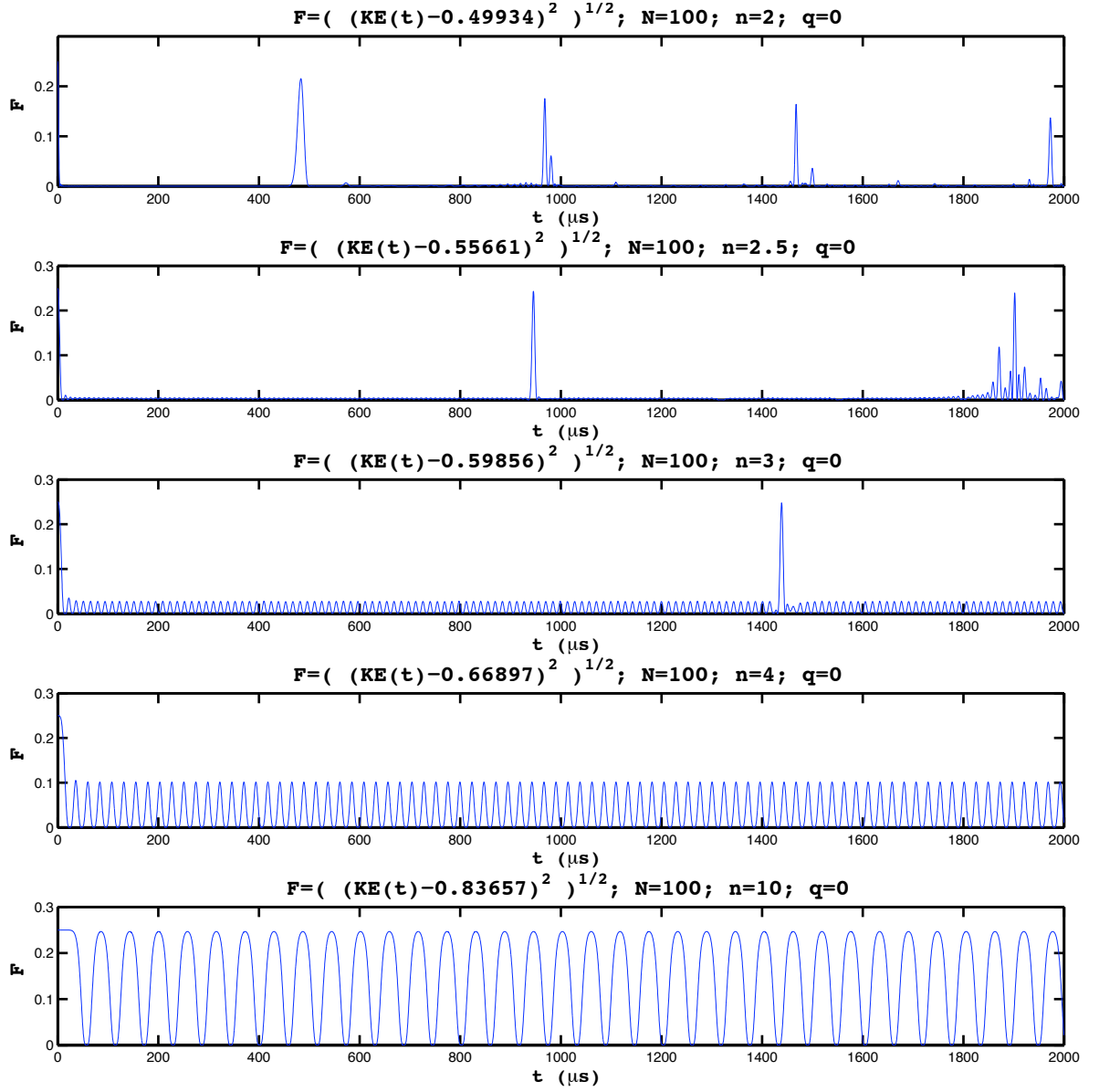


Figure 2.22: Fluctuations as a function of time and  $n$  for  $N = 100, q = 0$ .

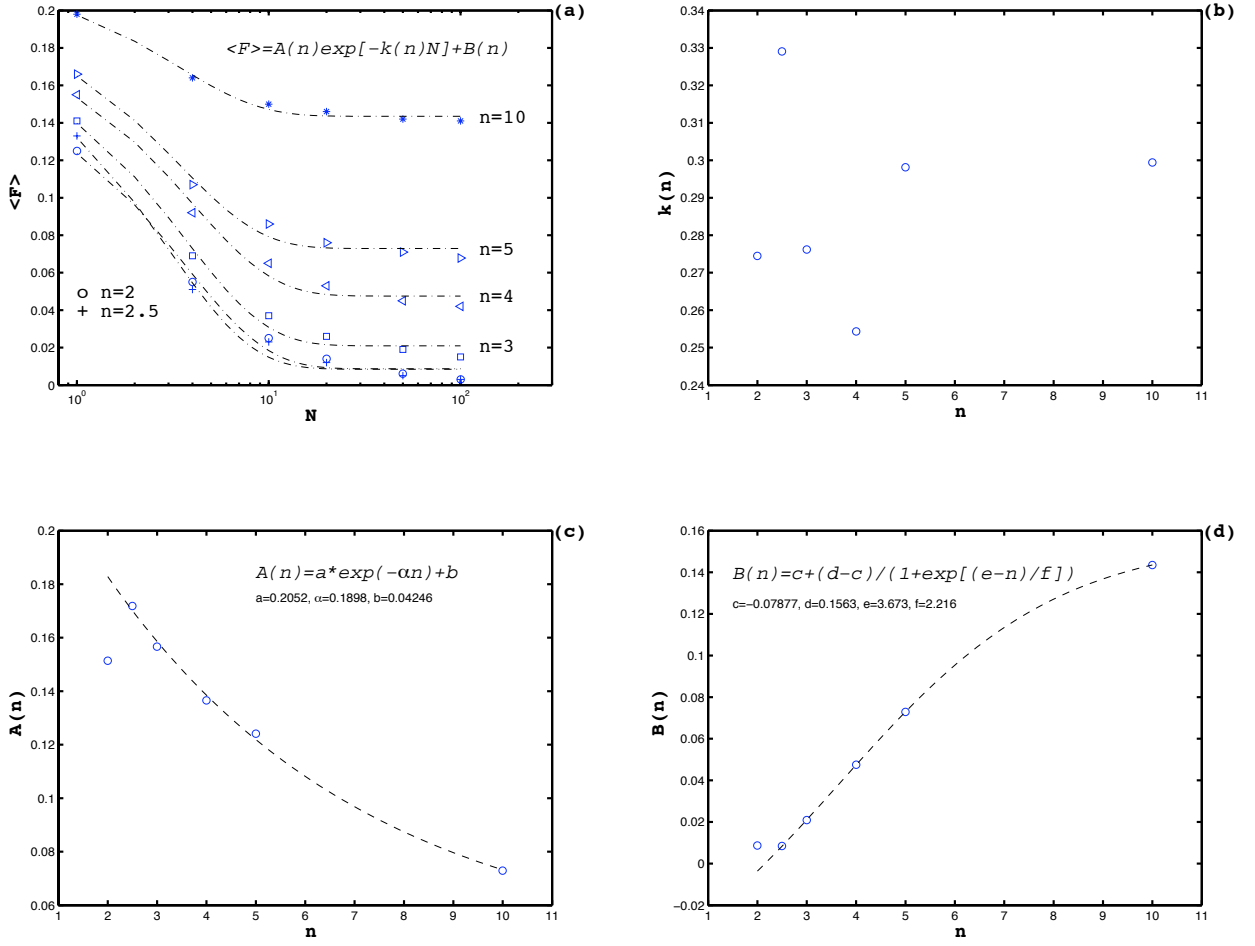


Figure 2.23: (a) Variation of  $\langle F \rangle$  with  $N$  for various  $n$  and fitting function. (b) Variation (scatter) of  $k$  with  $n$ . (c) Variation of  $A$  with  $n$  and corresponding fitting function. (d) Variation of  $B$  with  $n$  and corresponding fitting function.

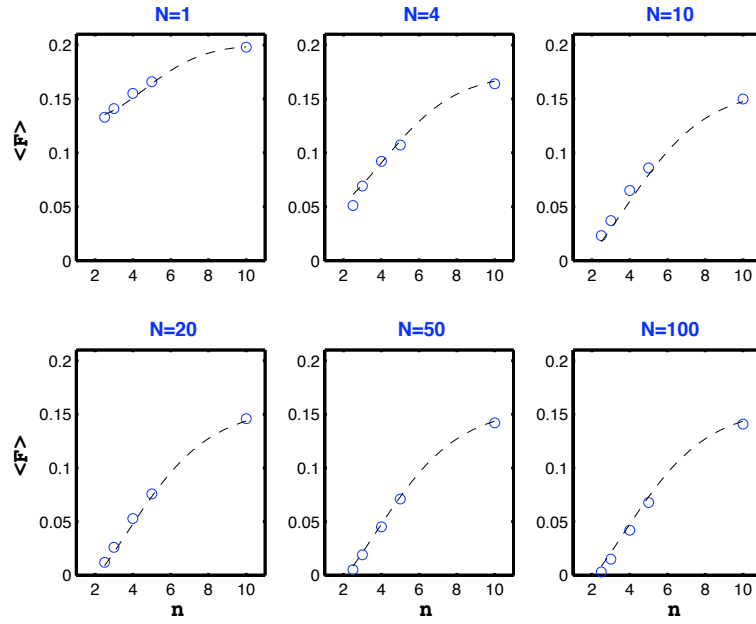


Figure 2.24:  $\langle F \rangle$  as a function of  $n$  for various  $N$  determined from simulation (circles). Derived fitting function  $\langle F \rangle = \langle F(n, N) \rangle$  is superimposed (dashed) in each panel.  $n = 2$  data is excluded as it doesn't fit the function.

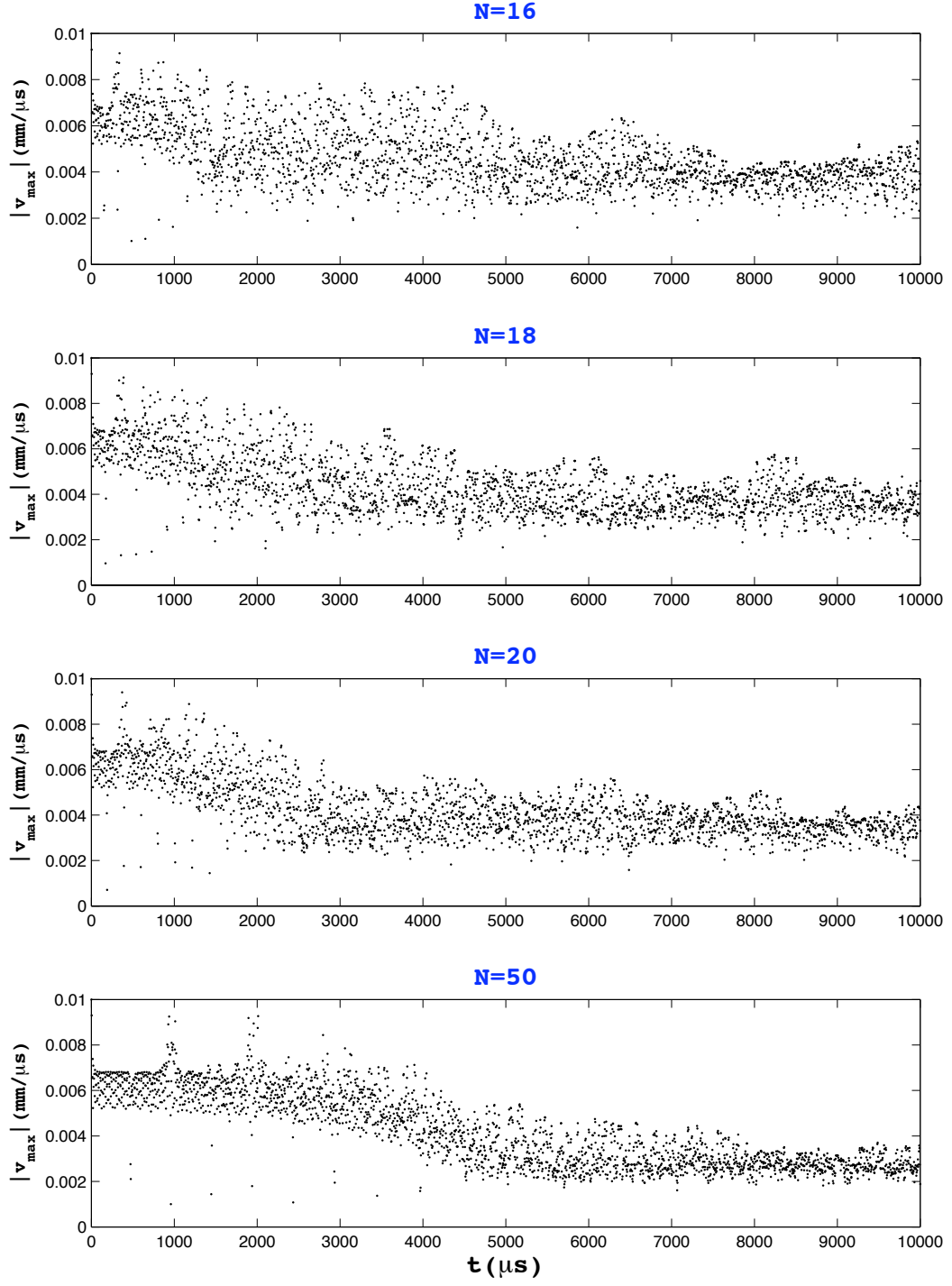


Figure 2.25:  $|v_{\max}|$  as a function of time for  $N = 16, 18, 20, 50$ .

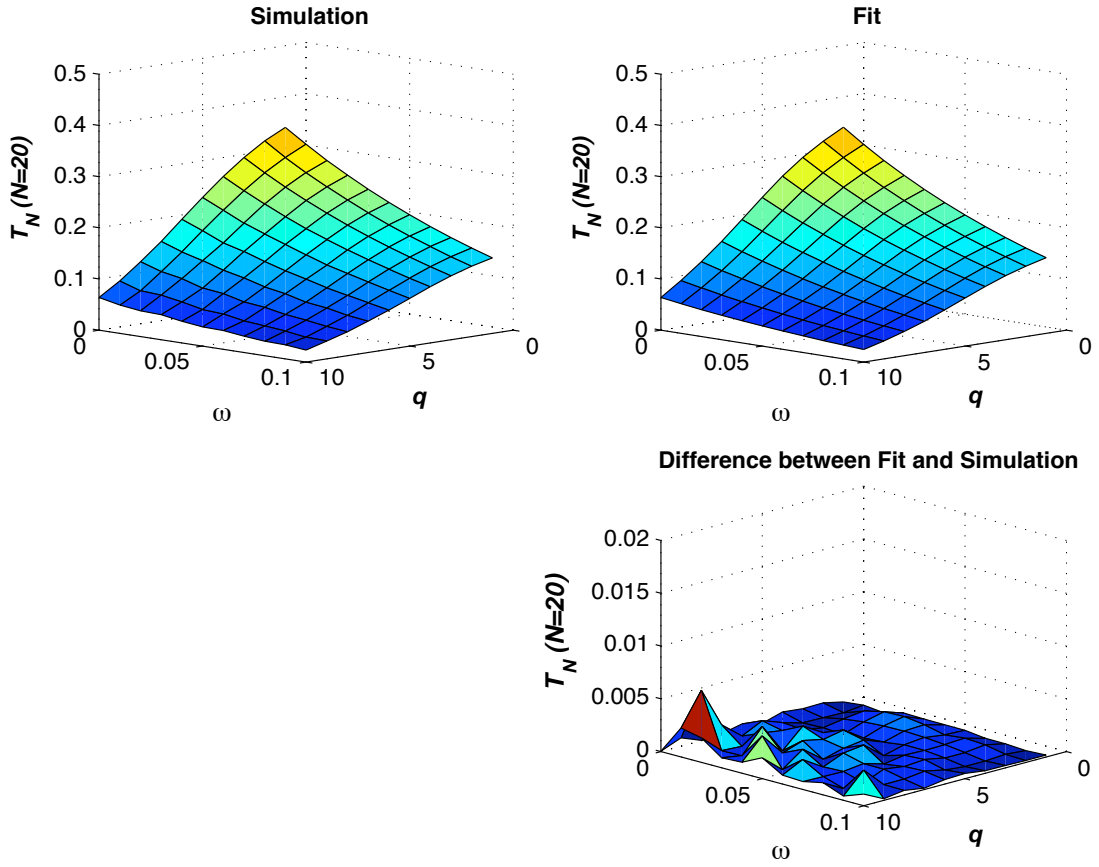


Figure 2.26: The Simulated and Modeled STC.

## Chapter 3

# The Decorated Tapered Chain (DTC)

### 3.1 Introduction

The content of this chapter was reported by Doney and Sen<sup>27,28</sup> in *Physical Review Letters*. The DTC (Figure 3.1) can be assembled from the STC by introducing a single-sized interstitial grain of radius,  $r_{even}$ , between every member of the STC. We constrain the system to an odd number of particles such that the grains that form the ends of the STC are still the outer members in the DTC. Additionally, we presume that these interstitial grains will be equal to or smaller than the smallest member of the STC (which has radius  $r_N$ ); therefore,  $r_{even} = fr_N$ , where  $0 < f \leq 1.0$ —although the flexibility is already built in for  $f$  to be any size.

It is immediately clear that the grain size mismatch changes as a function of position along the DTC. This is in stark contrast to the STC where successive grains are always smaller (or larger) by the same amount. It is possible then to have DTC chains that appear to resemble monodisperse chains for only a portion of the chain.

Section 3.2 derives the HSA and a fascinating limiting case for the DTC. Normalized KE parameter spaces are also presented. These results are followed in section 3.3 by the numeric solution to the EOM which includes a discussion on energy partitioning. Supporting plots highlighting the instantaneous energy breakdown per grain for a variety of chains in 10  $\mu s$  intervals is provided in Appendix D.

### 3.2 Hard-Sphere Approximation

In deriving an approximation for the DTC, the process is more cumbersome and the conservation equations for mass and energy are carried out for several terms until a pattern emerges. Our primary interest is in deriving an expression for the normalized kinetic energy,

$$E_K = \frac{KE_{out}}{KE_{in}} = \frac{m_N}{m_1} \left( \frac{v'_N}{v_1} \right)^2 = \frac{m_N}{m_1} \left\{ \left( \frac{v'_N}{v'_{N-1}} \right) \cdots \left( \frac{v'_{i+2}}{v'_{i+1}} \right) \left( \frac{v'_{i+1}}{v'_i} \right) \cdots \left( \frac{v'_2}{v_1} \right) \right\}^2. \quad (3.1)$$

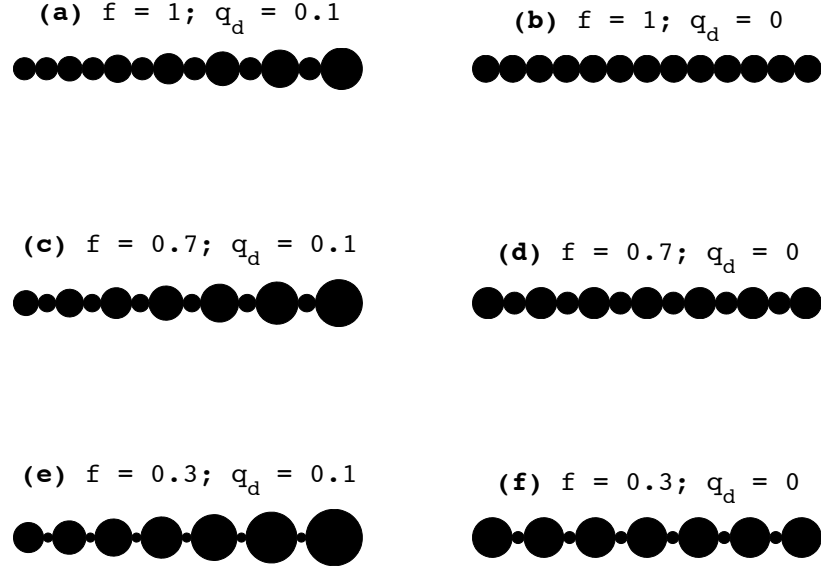


Figure 3.1: Several example DTCs created by varying  $f$  and  $q_d$  for constant  $N = 13$ .

Note that tapering in the DTC,  $q_d$ , is defined differently than for the STC. Thus,  $r_{i+2} = (1 - q_d)r_i$ . We will eventually look for forms of  $v'_{i+1}/v_i$  and then generalize for  $N$  particles or  $(N - 1)$  collisions. First, the relationship among masses and radii must be evaluated. Assembling the radii, we have starting with the largest bead,

$$\begin{aligned}
 r_i & \\
 r_{i+1} &= f r_N \\
 r_{i+2} &= r_i - q_d r_i = (1 - q_d) r_i = \epsilon r_i \\
 r_{i+3} &= f r_N \\
 r_{i+4} &= r_{i+2} - q_d r_{i+2} = (1 - q_d) r_{i+2} = \epsilon^2 r_i \\
 r_{i+5} &= f r_N \\
 r_{i+6} &= r_{i+4} - q_d r_{i+4} = (1 - q_d) r_{i+4} = \epsilon^3 r_i \\
 &\vdots \\
 r_{N-1} &= f r_N \\
 r_N &= r_{N-2} - q_d r_{N-2} = (1 - q_d) r_{N-2} = \epsilon^{(N-1)/2} r_i
 \end{aligned}$$

The major equations for radii are therefore

$$\begin{aligned} r_N &= \epsilon^{(N-1)/2} r_i \\ r_{(i+1),(i+3),\dots,(N-1)} &= f \epsilon^{(N-1)/2} r_i \end{aligned} \quad (3.2)$$

Recall for masses that  $m_i = \rho V_i = \frac{4}{3} \pi r_i^3 \rho = \eta r_i^3$ . Note that since  $\eta$  is just a constant and will cancel once the conservation equations are put into use, we will ignore it from now on. Expressions for  $m_i$  then become,

$$\begin{aligned} m_i &\sim \epsilon^0 r_i^3 \\ m_{i+1} &\sim r_{i+1}^3 = A r_i^3 \\ m_{i+2} &\sim \epsilon^3 r_i^3 \\ m_{i+3} &\sim r_{i+3}^3 = A r_i^3 \\ m_{i+4} &\sim \epsilon^6 r_i^3 \\ &\vdots \\ m_{N-1} &\sim r_{N-1}^3 = A r_i^3 \\ m_N &\sim \epsilon^{3(N-1)/2} r_i^3 \end{aligned} \quad (3.3)$$

where  $A = f^3 \epsilon^{3(N-1)/2}$ . These relations can now be used to set up the conservation equations. Beginning with momentum and assuming that each subsequent particle in the chain begins at rest, one can solve for the first five collisions. Primes and double-primes indicate post-collision states. A primed quantity denotes the first post-collision state of a sphere. That subsequent sphere will serve as the input to the next collision. To keep track of its velocity after the second collision, it is denoted by a double-prime and will eventually be eliminated. With  $\epsilon = (1 - q_d)$ ,

$$m_i v_i = m_i v'_i + m_{i+1} v'_{i+1} \quad \rightarrow \quad \boxed{v_i = v'_i + A v'_{i+1}} \quad (3.4)$$

$$m_{i+1} v'_{i+1} = m_{i+1} v''_{i+1} + m_{i+2} v'_{i+2} \quad \rightarrow \quad \boxed{A v'_{i+1} = A v''_{i+1} + \epsilon^3 v'_{i+2}} \quad (3.5)$$

$$m_{i+2} v'_{i+2} = m_{i+2} v''_{i+2} + m_{i+3} v'_{i+3} \quad \rightarrow \quad \boxed{\epsilon^3 v'_{i+2} = \epsilon^3 v''_{i+2} + A v'_{i+3}} \quad (3.6)$$

$$m_{i+3} v'_{i+3} = m_{i+3} v''_{i+3} + m_{i+4} v'_{i+4} \quad \rightarrow \quad \boxed{A v'_{i+3} = A v''_{i+3} + \epsilon^6 v'_{i+4}} \quad (3.7)$$

$$m_{i+4} v'_{i+4} = m_{i+4} v''_{i+4} + m_{i+5} v'_{i+5} \quad \rightarrow \quad \boxed{\epsilon^6 v'_{i+4} = \epsilon^6 v''_{i+4} + A v'_{i+5}} \quad (3.8)$$

$\vdots$



From the pattern in equations (3.4-3.8), (3.4) can be rewritten as  $\epsilon^0 v'_i = \epsilon^0 v'_i + A v'_{i+1}$ . An evaluation of energy conservation yields the same form as equations (3.4-3.8) except velocities are squared:

$$v_i^2 = v_i'^2 + A v_{i+1}'^2 \quad (3.9)$$

$$A v_{i+1}'^2 = A v_{i+1}''^2 + \epsilon^3 v_{i+2}'^2 \quad (3.10)$$

$$\epsilon^3 v_{i+2}'^2 = \epsilon^3 v_{i+2}''^2 + A v_{i+3}'^2 \quad (3.11)$$

$$A v_{i+3}'^2 = A v_{i+3}''^2 + \epsilon^6 v_{i+4}'^2 \quad (3.12)$$

$$\epsilon^6 v_{i+4}'^2 = \epsilon^6 v_{i+4}''^2 + A v_{i+5}'^2 \quad (3.13)$$

⋮

Next, combine equations (3.4-3.8) and (3.9-3.13) to eliminate the double-primed terms and form the velocity ratios:  $\frac{v'_{i+1}}{v_i}$ ,  $\frac{v'_{i+2}}{v'_{i+1}}$ , etc. Beginning with (3.4), isolate  $v'_i$  and square it to obtain  $v_i'^2 = v_i^2 - 2A v_i v'_{i+1} + A^2 v_{i+1}'^2$ . Next, substitute this into (3.9) and rearrange to obtain  $\frac{v'_{i+1}}{v_i}$ . This is then repeated for equations (3.5,3.10), (3.6,3.11), etc. to obtain the following ratios:

$$\frac{v'_{i+1}}{v_i} = \frac{2\epsilon^0}{A + \epsilon^0} \quad (3.14)$$

$$\frac{v'_{i+2}}{v'_{i+1}} = \frac{2A}{\epsilon^3 + A} \quad (3.15)$$

$$\frac{v'_{i+3}}{v_{i+2}} = \frac{2\epsilon^3}{A + \epsilon^3} \quad (3.16)$$

$$\frac{v'_{i+4}}{v'_{i+3}} = \frac{2A}{\epsilon^6 + A} \quad (3.17)$$

⋮

where hindsight has allowed us to insert terms of  $\epsilon^0$  in (3.14). With an eye fixed on (3.1), results may be merged. Thus

$$\frac{v'_N}{v_1} = \left(\frac{v'_2}{v_1}\right) \dots \left(\frac{v'_{i+1}}{v_i}\right) \left(\frac{v'_{i+2}}{v'_{i+1}}\right) \dots \left(\frac{v'_N}{v'_{N-1}}\right) \quad (3.18)$$

$$= \underbrace{\left(\frac{2\epsilon^0}{A+\epsilon^0}\right)\left(\frac{2A}{\epsilon^3+A}\right)}_{N=3} \underbrace{\left(\frac{2\epsilon^3}{A+\epsilon^3}\right)\left(\frac{2A}{\epsilon^6+A}\right)}_{N=5} \underbrace{\left(\frac{2\epsilon^6}{A+\epsilon^6}\right)\left(\frac{2A}{\epsilon^9+A}\right)}_{N=7} \quad (3.19)$$

$\vdots$

The ratio can be put into closed form to obtain,

$$\therefore \frac{v'_N}{v_1} = \prod_{j=1}^{(N-1)/2} \left(\frac{2\epsilon^{3(j-1)}}{A+\epsilon^{3(j-1)}}\right) \left(\frac{2A}{\epsilon^{3j}+A}\right) \quad (3.20)$$

$$= 2^{N-1} A^{(N-1)/2} \prod_{j=1}^{(N-1)/2} \left(\frac{\epsilon^{3(j-1)}}{A+\epsilon^{3(j-1)}}\right) \left(\frac{1}{\epsilon^{3j}+A}\right) \quad (3.21)$$

Turning to the mass ratios and using expressions from (3.3), it appears that most terms cancel:

$$\frac{m_N}{m_1} = \left(\frac{m_2}{m_1}\right) \dots \left(\frac{m_{i+1}}{m_i}\right) \left(\frac{m_{i+2}}{m_{i+1}}\right) \dots \left(\frac{m_N}{m_{N-1}}\right) \quad (3.22)$$

$$= \left(\frac{A}{\epsilon^0}\right) \left(\frac{\epsilon^3}{A}\right) \left(\frac{A}{\epsilon^3}\right) \left(\frac{\epsilon^6}{A}\right) \dots \quad (3.23)$$

leading to the simple expression,

$$\frac{m_N}{m_1} = \epsilon^{3(N-1)/2} \quad (3.24)$$

One can now identify the normalized kinetic energy (3.1) by squaring (3.21) and combining it with (3.24) to form,

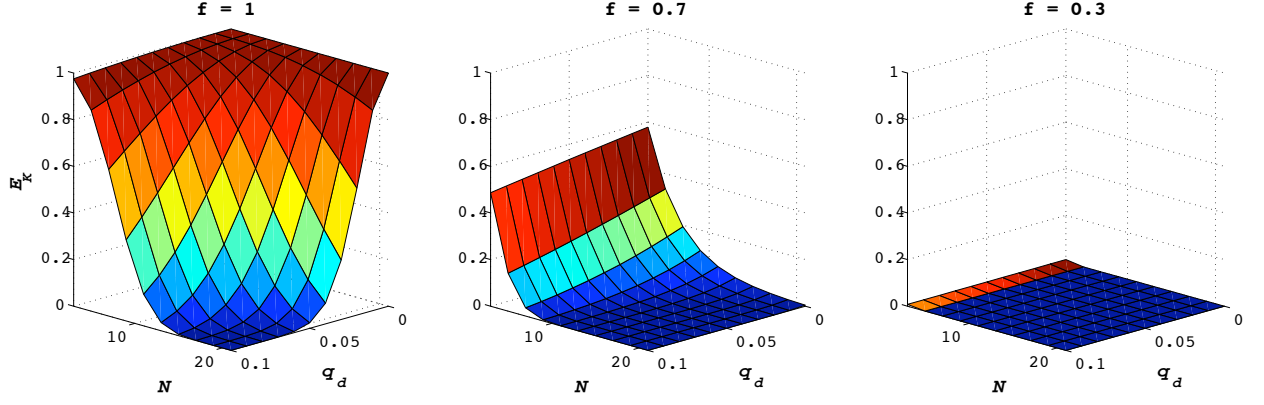


Figure 3.2: Normalized kinetic energy surfaces,  $E_K \equiv K_{OUT}/K_{IN}$ , for the decorated chain under the hard sphere approximation as functions of the number of spheres,  $N$ , fractional size of interstitial sphere,  $f$ , and tapering,  $q_d$ .

$$E_K^{(dtc)} = (4A\epsilon^{3/2})^{(N-1)} \left\{ \prod_{j=1}^{(N-1)/2} \frac{\epsilon^{3(j-1)}}{(A + \epsilon^{3(j-1)})(\epsilon^{3j} + A)} \right\}^2. \quad (3.25)$$

These results are plotted in Figure 3.2. The effects of the interstitial sphere are remarkable when compared to the simple chains in figure 2.2(a). For a modest value,  $f = 0.7$ , it takes very few particles to reduce the outgoing kinetic energy considerably.  $E_K^{(dtc)}$  decays as a gaussian or sigmoid with increasing  $q_d$ , and exponentially with increasing  $N$ .

It is difficult to draw any physical intuition from (3.25). However, a very curious and astonishing result occurs in the limit  $q_d = 0$ :

$$E_K^{(dtc)}|_{q_d=0} = \left( \frac{4f^3}{[f^3 + 1]^2} \right)^{N-1}. \quad (3.26)$$

This limit is equivalent to equation (2.7) under the exchange  $f \iff (1 - q_s)$ .

It is clear that  $f = 1$  should imply  $q_s = 0$  since they both generate monodisperse chains. That this equivalency goes beyond that special case is quite unexpected. One can now begin to see the incredible effect  $f$  has on the energy mitigation capability when an infinite potential is invoked: for  $f = 0.3$  — a typical value we might consider — the equivalent tapering in the simple chain would be  $q_s = 0.7$ . This value is 7 times larger than any system we had previously considered and could be a significant system integration challenge. Visually, for hard-spheres, the energy mitigation capability of the simple chain shown in Figure 2.1 ( $q_s = 0.1$ ) is identical to that for a decorated chain similar to that shown in Figure 3.1(b) but with  $q_d = 0, N = 10, f = 0.9$ .

### 3.3 Numeric Solution

#### 3.3.1 KE Parameter Space Behavior

Figure 3.3 highlights the computational results for the decorated chain. Recall that the inertial mismatch between neighboring grains in decorated chains change as a function of position along the chain. This is what is believed to be the cause of a ripple in the surface of the  $E_K$  plots that propagate toward the origin as  $f$  decreases. As one might expect, such behavior is a function of  $N$ ,  $q_d$ , and  $f$ . The effect vanishes for  $f \leq 0.6$ , approximately. At about this threshold, the interstitial grain is not much smaller (less massive) than the grains toward the end of the chain. The explanation is that as an impulse propagates, energy transmission becomes increasingly efficient due to smaller inertial mismatches — a prerequisite for admitting solitary waves. Thus the system changes from a shock absorber to shock transmitter. This effect however must compete with compressive effects in some manner since no such behavior is present for hard spheres even though it too has a position-dependent inertial mismatch.

The hard sphere approximation grossly exaggerates the shock mitigation capability of the decorated chain. Additionally, it doesn't pick up the surface feature resulting from a competition between particle overlap nonlinearity and variable inertial mismatches between neighboring grains. Thus a hard-sphere analysis is inadequate for the DTC. Simulations suggest that for  $f = 0.3$ ,  $N = 5$ ,  $q_d = 0.1$  (panel f), one can disperse energy within the chain such that only about 10% of that put into the system is transmitted to the end with the initial pulse.

#### 3.3.2 Energy Partition

A simple view of energy partitioning in the DTC is not possible given the vast number of possible chain configurations, belittling those of the STC. Changing  $N$  has a much more severe impact on the results because, by design, it affects the results everywhere in the chain. For example, if we take the mass ratio of interstitial grains for  $N = 21$  and  $N = 11$  chains, with  $q_d$  and  $f$  identical, the results scale astonishingly:  $m_{N=21}/m_{N=11} \propto (1 - q_d)^{15}$ ! For large tapering,  $q_d = 0.1$ , interstitial grains in a chain with  $N = 21$  have about one-fifth the mass as their counterparts where  $N = 11$ .

Rather than focusing on the system, it is of interest to probe how a DTC partitions the energy among particles as an impulse propagates. Figure 3.4 illustrates the instantaneous kinetic energy per grain for various configurations at  $t = 52\mu\text{s}$  where  $q_d = \{0, 0.05, 0.1\}$  and  $f = \{1.0, 0.7, 0.3\}$ . Also included in each panel is a silhouette of the specific chain and the total kinetic energy of the

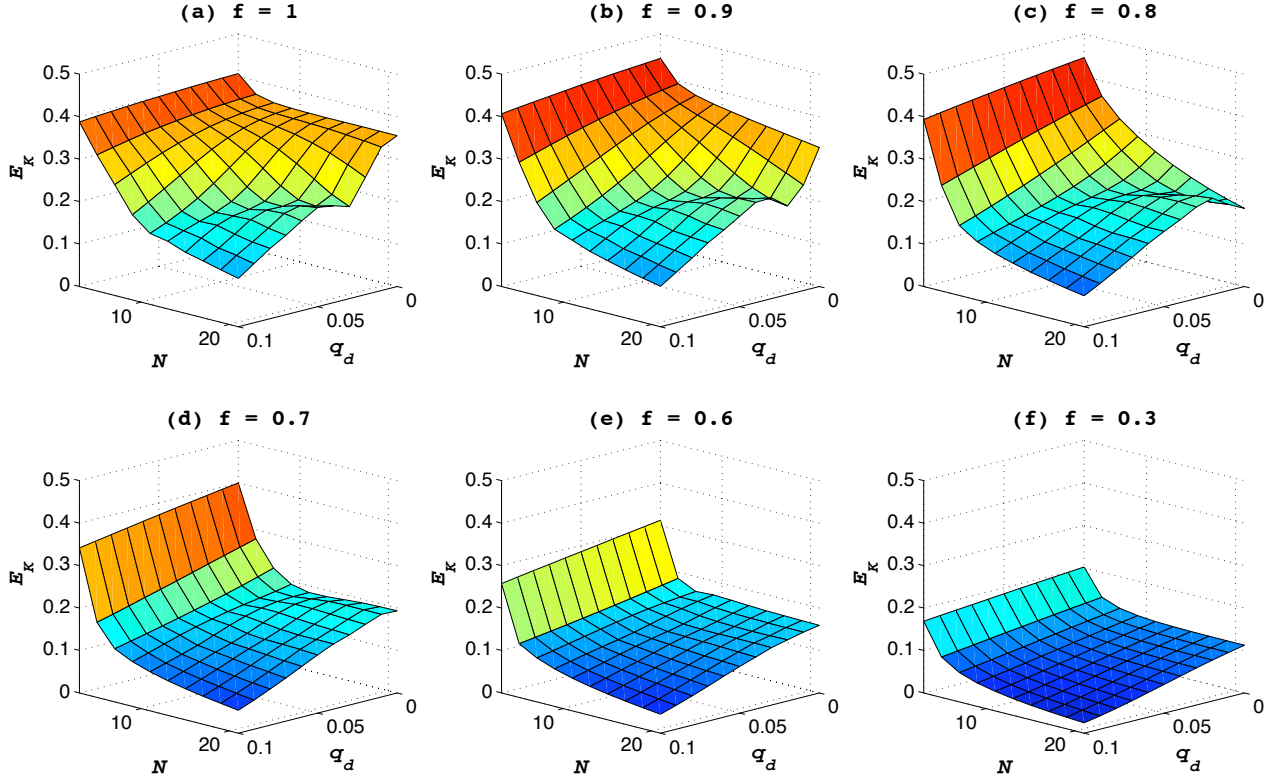


Figure 3.3: Numerically-produced normalized kinetic energy surfaces,  $E_K \equiv K_{OUT}/K_{IN}$ , for the decorated chain as functions of the number of spheres,  $N$ , fractional size of interstitial sphere,  $f$ , and tapering,  $q_d$ . Several sample chains are identified in panels (d-i).

system as a function of time. The black disk indicates the current simulation time. It should be noted that panel (a) is identical to figure 2.13(a) since they are both monodisperse chains. A cursory glance of all panels reveal that the effect of  $q_d$  is to spread the impulse out over many grains in a manner similar to the STC. And secondly, when decreasing  $f$  the energy appears to be distributed to the larger, non-interstitial (odd numbered) grains. It is hypothesized that additional, neighboring interstitial spheres would further separate the energy along the chain. What this also appears to do is turn the DTC into, effectively, a binary collision system since the amplitudes of interstitial spheres is quite superficial. Also of note is that the speed of energy transmission appears more dependent on  $q_d$  than  $f$ .

The division of energy into the larger grains for small  $f$  appears to be a result of their larger masses, rather than the increased “rattling” of interstitial spheres. For example, the mass ratio between grains 15 and 14 in panel (i) is about 0.004. This value becomes more matched as one approaches grains 1 and 2 which has a ratio of about 0.03. Even though the even-numbered grains

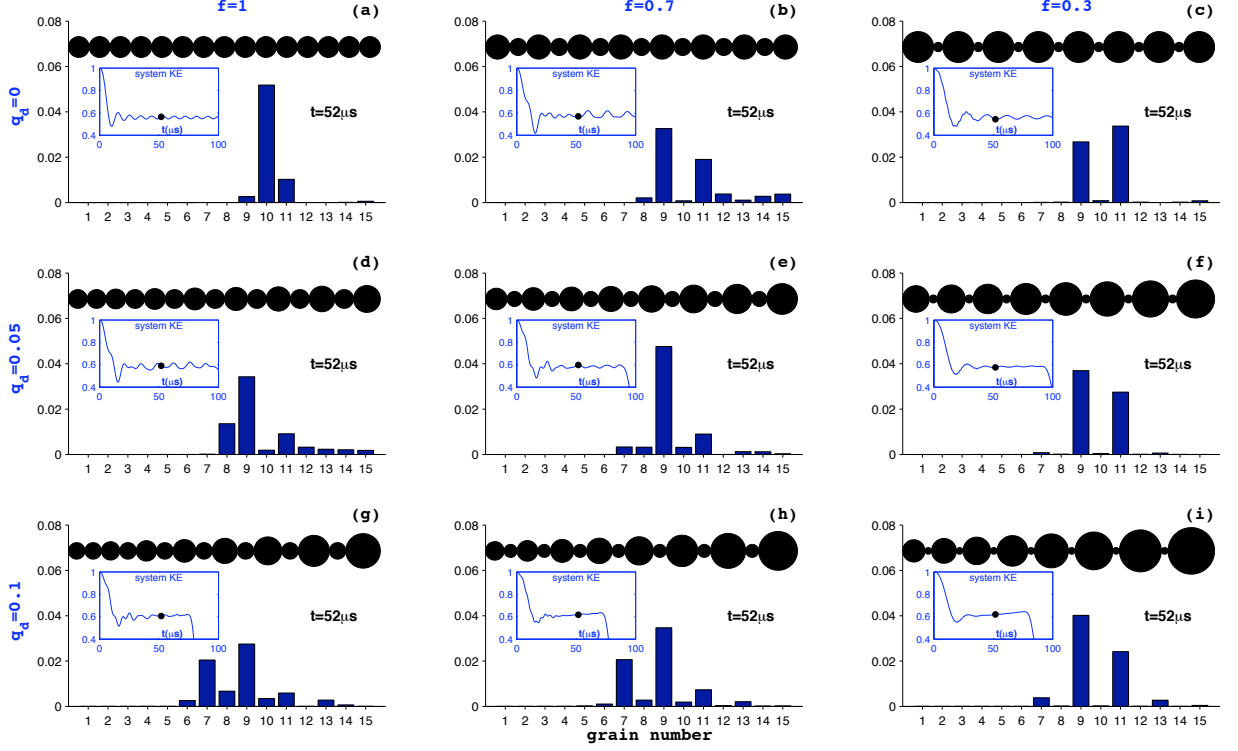


Figure 3.4: Instantaneous kinetic energy per grain for various DTC configurations at  $t = 52\mu\text{s}$  where  $q_d = \{0, 0.05, 0.1\}$  and  $f = \{1.0, 0.7, 0.3\}$ .

have a much higher velocity than their larger neighbors, kinetic energy only scales as  $v^2$  versus  $m \sim r^3$ . The smaller system kinetic energy plots in each panel reveals the complicated nature of the system—a consequence of the competition among  $f, q_d, N$ . The dynamics tend to be more smooth for small  $f$  because of the smaller role played by interstitial spheres to the total system energy. One area that still needs investigating is possibility of multiple grains overlap for very small  $f$ . In this case, the EOM would need to be modified to take into account the next layer of neighbors.

Panels (b,c) may not necessarily admit SWs, but localized energy propagation does occur. In both cases, the amplitude dampens, in agreement with Manciu<sup>59</sup>—this is more obvious with larger  $N$  (not pictured). Panels (f,i) quickly spread out the energy because of the finite tapering which is also the reason for an increasing KE ramp (shown in the inset). However, tapering  $q_d$  now must compete with  $f$  as results vary significantly among other panels. A thorough analysis of that rivalry has not yet been investigated.

It is instructive to observe in time, how waves propagate through such systems. Appendix D shows a sequence of these plots in  $10\mu\text{s}$  intervals. One can flip through the pages so that they appear animated.

## Chapter 4

# Hydrocode Simulations of Tapered Chains

There are two reasons that stand out when considering the simulation of TCs in a hydrodynamics code (hydrocode). The first is in probing the regime where plastic, and therefore permanent, deformation can occur. Secondly, it represents the next step towards the development of a potential TC armor panel. This brief chapter describes preliminary efforts in running such 2D and 3D simulations. These results were presented at the March 2006 meeting of the American Physical Society in Baltimore, MD.

ALEGRA<sup>18,79,110</sup>—or Arbitrary Lagrangian and Eulerian General Research Application—is a massively parallel, finite element hydrodynamics code with modular physics capability developed by Sandia National Laboratories. The general procedure for running such simulations consists of mesh generation, simulation, and post-processing. The first step is performed using CUBIT<sup>22</sup> which discretizes the computational space. At each node, the conservation equations are solved using ALEGRA. Finally, visualization is performed using Ensight<sup>17</sup>. While the manuals of the code are publicly available, the software itself is export-controlled.

Both lagrangian and eulerian meshes have been considered for 3D and 2D meshes, respectively. In the latter case, material advects through a stationary mesh<sup>1</sup>. This is in contrast to the Lagrangian framework where the material is the mesh. An inherent difficulty in running Eulerian calculations, is that mixed cells are endemic to the mesh. That is, any cell can be occupied by more than 1 material: part air, part water for example. As time progresses and the material advects through the mesh, a code needs to keep track of that boundary between materials which has to be determined at a resolution finer than the mesh. This is known as interface tracking (IT) or interface reconstruction (IR). Currently, ALEGRA supports<sup>16</sup> three schemes: SLIC<sup>2</sup>, SMYRA<sup>3,8</sup>, and NEW SMYRA. Results from simulations should be independent of the mesh (“mesh convergence”) as well as the IT scheme, much in the way that physics is independent of a coordinate system. In Lagrange

---

<sup>1</sup>More specifically, there is a lagrange step where the mesh deforms to follow the material and then is mapped back into the eulerian mesh

<sup>2</sup>Simple Line Interface Calculation

<sup>3</sup>Sandia Modified Young’s Reconstruction Algorithm

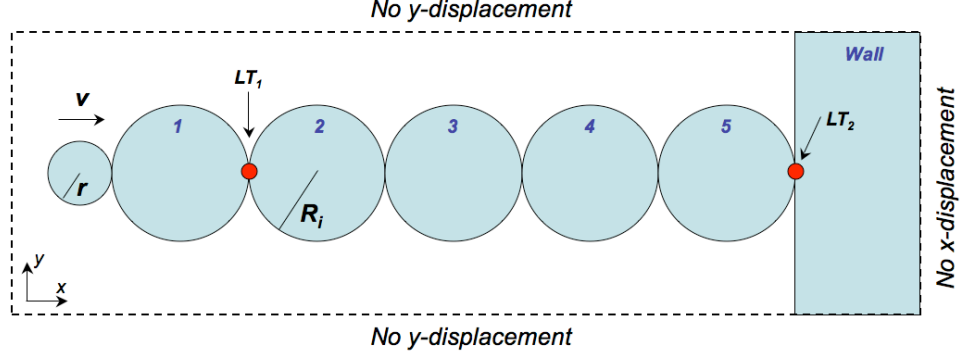


Figure 4.1: Computational domain and problem setup for the ALEGRA simulation.

frameworks, there are no mixed cells — so it is the preferred method assuming deformations are not too large to cause element inversions.

Properties of inert and reactive materials and equations of state have been evaluated semi-empirically for the past half-century. Many of those results are available as tabular databases and can be read by various computer codes. The SESAME EOS is one such behemoth and used frequently in hydrocode simulations. One also needs a material strength model and the Johnson-Cook<sup>16</sup> model is common,

$$Y = [A + B\epsilon^N][1 + C \ln(\max(0.002, \dot{\epsilon}))] \left( \frac{T - T_r}{T_m - T_r} \right)^m$$

where the  $A, B, C, N, m, T$  parameters are material dependent,  $\epsilon$  is the equivalent plastic strain, and  $T_r, T_m$  are the room and melt temperatures, respectively. The values of these constants have been evaluated for a great many materials. Note that all material models are not created equal. Some models perform well through phase transitions for example, while others may not, i.e. Mie-Grüneisen.

## 4.1 2D Eulerian ALEGRA simulations

The initial effort consisted of inserting copper disks into a 2D eulerian mesh with cartesian symmetry. This implies that the problem is really that of infinitely long cylinders since the symmetry is translational along the  $z$ -axis. Copper disks were used because the elastic-plastic behavior in the SESAME model is well-characterized (even across multiple phases) and has been utilized for quite some time. Figure 4.1 highlights the problem setup. The geometry consists of a 5-particle monodis-



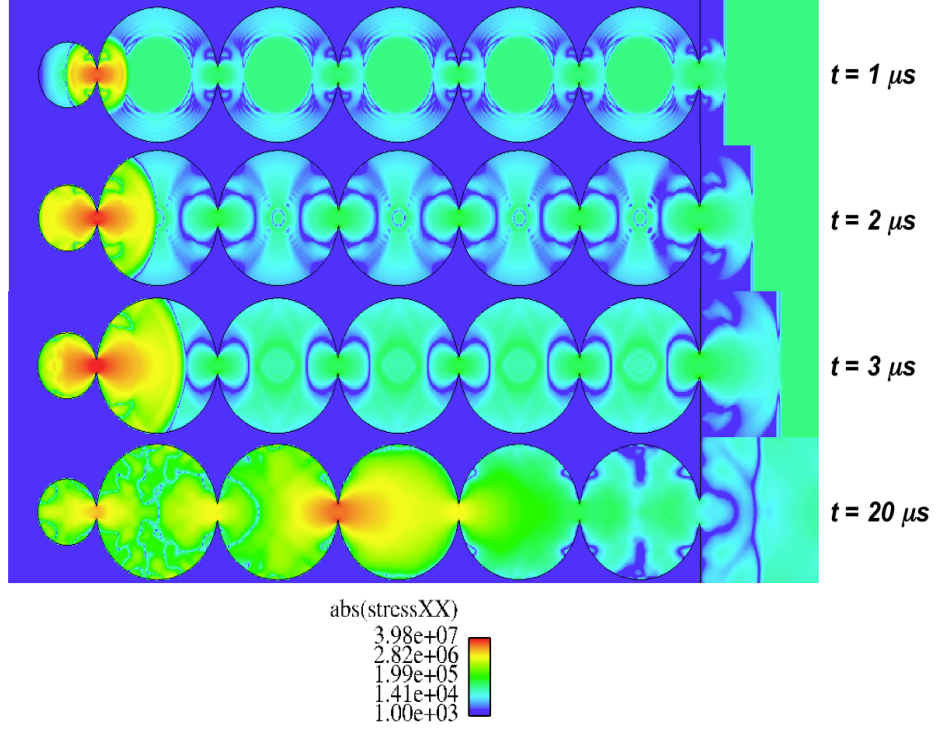


Figure 4.2: Evolution of  $|\sigma_{xx}|$ . Color scale is logarithmic.

perse chain adjacent to a large wall. Grain 1 is impacted by a smaller sphere moving to the right with velocity,  $v$ . The purpose of  $LT_1$  is to measure the grain-grain interaction and obtain a value for  $\delta^n$  while  $LT_2$  can record force. The incorporation of such Lagrange tracer particles — which move with the material — allows the user to track various quantities over time without worrying about displacement. This problem is ideal for a first series of verification and validation studies that could be based on the work of Rossmannith and Shukla<sup>91</sup>. The following steps would be required: increase the number of spheres, add a gravitational field and change the material parameters. For the case of increasing zig-zag obliquity, the disks would need to be put between walls whose distance changes with the angle of obliquity.

Preliminary results of a test simulation, where  $|\sigma_{xx}|$  — the absolute normal component of stress along  $x$  in units of Pascals, are shown in Figure 4.2. The input velocity is about  $2.5 \text{ mm}/\mu\text{s}$  and the color scale is logarithmic. The regions in the top 3 panels — in what looks like ringing — are believed to be artifacts of an improper lower boundary in the color map. It is therefore most likely numerical noise. What is clear however, is that the shock propagation adds a level of fidelity not available in the analysis of earlier chapters.

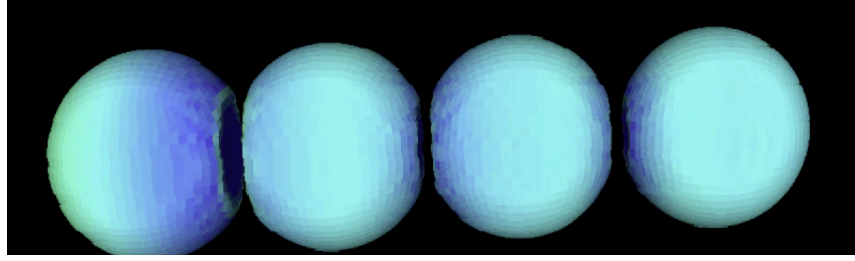


Figure 4.3: Basic 3D simulation of a TC. Note that the bulk behavior of the spheres is consistent with expectation even though dynamics take place on a elemental or nodal basis. A small amount of plastic flow is visible.

## 4.2 3D Lagrangian ALEGRA simulations

More interesting to the research and where the effort is now focused, is the simulation of a 3D alignment of spheres. The jump in complexity however is quite considerable and requires the incorporation of a global contact model. The contact mechanics package ALEGRA utilizes is known as ACME<sup>13</sup>. This area is probably the most critical in setting up the problem and therefore the one that will require the most care.

In the 3D environment, individual spherical meshes are created and positioned similar to how a tapered chain is parameterized. An initial simulation was run to verify that sphere velocities increase along a chain when finite tapering is introduced. That result is presented in figure 4.3 where  $N = 4, q \sim 0.05$ . In the animation, it is clear that the velocity of the right-most particle is larger than the trailing spheres. The same is true for the penultimate sphere, etc. Also visible is a decreasing amount of deformation in the spheres as one moves rightward. In this sense, the spheres have absorbed energy even though plastic flow is evident. What's important to point out is that even though interactions are being performed on a nodal or elemental basis where the latter is of arbitrary size, the bulk behavior of the system is consistent with expectations. Upon close inspection one can gauge the resolution of the mesh. For these problems, there are 50 azimuthal divisions and 6 radial divisions — corresponding to 1200 elements — per particle. The CUBIT script which creates the spherical meshes is listed in appendix F while the ALEGRA input script, which specifies the relevant physics is listed in appendix G. Note that in both cases the real input for both CUBIT and ALEGRA is much larger. Both scripts have utilized a package known as APREPRO which is a preprocessing utility that allows one to incorporate algebraic expressions.

It was useful to quantitatively compare the results between numerically solving the EOM from chapter 2 and ALEGRA solutions. An exact match was not expected since the latter has barely been tested and refined. Figure 4.4 reflects this. Both simulations consisted of a TC where

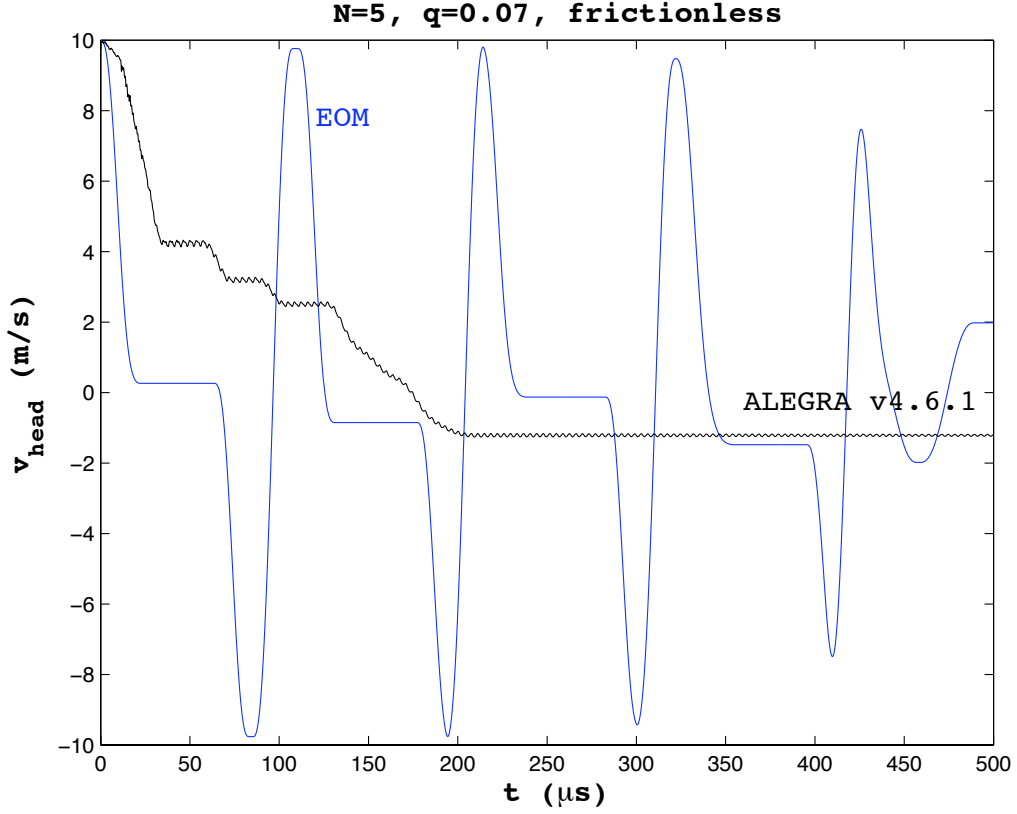


Figure 4.4: Velocity of the head particle as a function of time for both EOM and ALEGRA simulations where  $N = 5, q = 0.07$  and restitutive losses are neglected.

$N = 5, q = 0.07$ . In the case of the EOM problem, restitutive losses were neglected. None were specifically inserted into the contact model for the 3D simulation; however, it is unclear whether there is a nonzero default value. In addition, the boundary conditions are not the same as the EOM problem. In fact, no boundary conditions along the direction of motion were specified, so the particles can continue indefinitely — which is why the ALEGRA curve shows a saturation that continues unabated. Also, it is unclear why there is a step-like decay. It is very possibly that mesh-resolution is playing a role where the number of radial elements would have the biggest impact. Another point is that the material models are different between the two cases. While many metals can be approximated by a Poisson ratio of 0.33, their strengths can vary substantially.

As an example of the capabilities of the code and the last simulation performed to date, the initial velocity was substantially increased to 500 m/s. Snapshots of the results are visible in figure 4.5. In these panels, color is scaled linearly by velocity with dark blue representing spheres at rest. The amount of deformation is significant and permanent. Again, these spheres are copper and

simulations have not yet been performed with other metals. In the last panel, the copper “pancakes” are still moving at approximately 250 m/s.

As a final note, many interesting questions can now be asked and explored with the use of ALEGRA. While testing of the systems and proper and careful setup still need to be performed, there is now the capability to investigate the combined effects of many TCs. Antiparallel arrangements can be inserted into the mesh and surrounded by other metals, insulators, etc. These can be encased by various alloys of steel and struck with a flyer plate (see figure 5.1). The resulting force can be measured on the output by surface tools in the visualization software. In addition, (virtual) tracer particles can be put at arbitrary locations to monitor local effects. The possibilities are actually quite staggering — stay tuned.

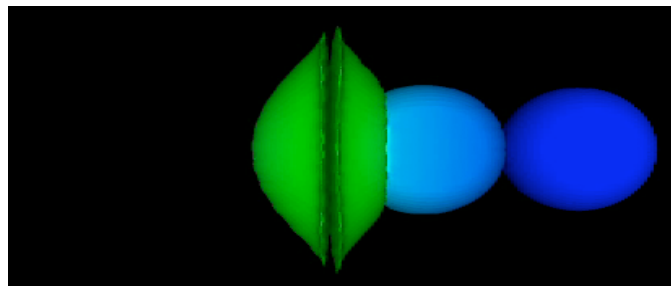
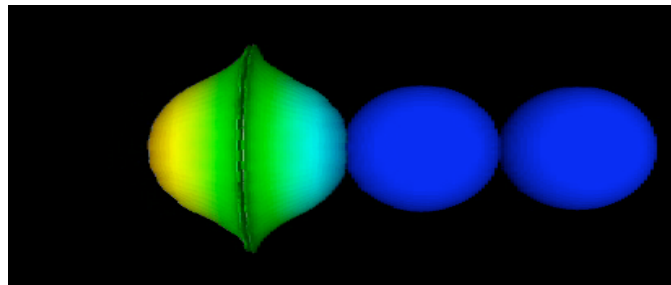
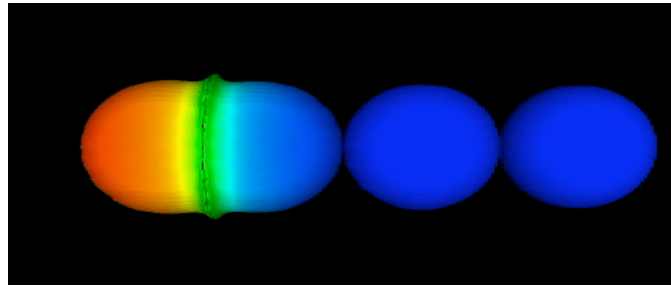
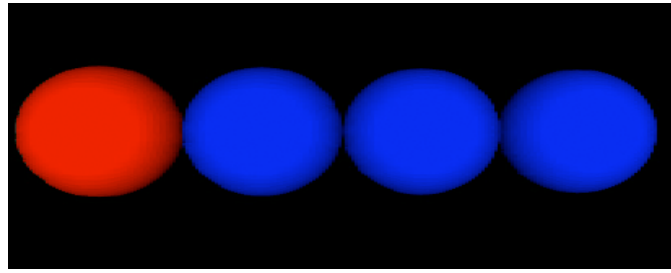


Figure 4.5: Time elapsed sequence where the initial velocity of the left-most grain has been increased to 500 m/s (red). The remaining spheres are initially stationary (blue).

# Chapter 5

## Closing Remarks

On March 12, 2006, Joe Ray — a close family friend, employee of Buncombe County in Asheville, NC, and an explosives ordnance specialist — was clearing mines for civilian and coalition traffic in Asadabad, Afghanistan during Operation Enduring Freedom. The up-armored humvee that was carrying him, Sgt. Kevin Akins, Spc. Joshua Hill, and Sgt. Anton Hiett of the 391st Engineer Battalion<sup>4,12</sup> was hit by a stationary and camouflaged improvised explosive device. No one survived. Such vehicles are overmatched by the seemingly endless quantity of explosive that can be put into such contemptible devices. It is just one example — and a personal one — where there will *always* be a need to improve our ability in absorbing blast energy. While the technology that has been discussed in this dissertation is not claiming to be able to mitigate the meganewtons of force that such blasts can generate, it represents the basic research which hopefully paves the way for us to get there. To that end, we have investigated the shock mitigation and nonlinear dynamical properties — as it pertains to the partition of energy — of tapered metal spheres arranged in one-dimensional arrays.

The analysis has been carried out where two chain geometries are of particular interest: the simple tapered chain (STC: figure 2.1) and the decorated tapered chain (DTC: figure 3.1). These systems exhibit strongly nonlinear behavior due to the Hertz potential which has been used to govern the contact mechanics in solving the equations of motion for each sphere. The dynamics and shock mitigation properties of each chain have been analyzed as functions of the relevant parameters. These are constant for each chain and are defined as the number of spheres, the tapering, and the coefficient of restitution. For the DTC, there is an additional parameter,  $f$ , which governs the size of interstitial spheres used to increase the inertial mismatch between neighboring grains. The following conclusions with a short summary is offered.

**Both chain geometries decimate impulses substantially.**

It is clear from the experiments performed by others and the simulations and data presented here that both the STC and DTC decimate impulses. Further, the DTC can outperform the STC in fewer spheres, making it desirable in applications where little space is available. The primary mechanism responsible is symmetry breaking, or inertial mismatches between neighboring grains. Essentially, momentum and energy remain trapped in the donor sphere thus spreading an impulse out in time and space as it propagates through a chain. This is repeated at each interface where there is a mismatch. For equally-sized spheres, solitary waves (SW) propagate and symmetry is maintained except at the boundary. Once the boundary is reached, the SW is reconstructed, but imperfectly. That left-over energy goes into the creation of secondary solitary waves (SSW) which have the same width, but travel at smaller velocities due to the small amplitudes. This process continues indefinitely. In the DTC, the effect of  $q_d$  is to spread the impulse out over many grains in a manner similar to the STC. Secondly, the role of decreasing  $f$  is to distribute energy to the larger, non-interstitial grains. By increasing the number of interstitial grains, it is hypothesized that energy would continue to spread out and remain trapped in the larger grains. This has applications for redirecting the energy if those sites were sufficiently coupled to some transit channel — making the problem 2D or 3D. One could also potentially increase dissipation with clever selection of materials.

**A hard-sphere approximation is valid for the STC but invalid for the DTC.**

Normalized energy and force surfaces were evaluated to measure each chain's trapping ability. In considering the STC, results indicate that there is a sigmoidal or gaussian decay on  $q$  and an exponential dependence on  $N$ . This trend is consistent with the results from numerically solving the equations of motion. For the DTC however, the hard-sphere analysis and numerical solution are markedly different in terms of the former missing phenomenology and greatly over-predicting energy absorption.

**The DTC hard-sphere approximation reduces to the STC in a special limit.**

It was quite surprising that in the limit  $q_d = 0$ , equation (3.25) — which describes the shock absorption quality of a DTC for  $N, q, f$  — reduces to equation (2.7) under the exchange  $f \iff (1 - q_s)$ . This says that a hard-sphere chain, consisting of an alternating series of radii (where  $r_{small} = f r_{large}$ ), has the kinetic energy absorption equivalency of a STC with tapering  $q_s$ .

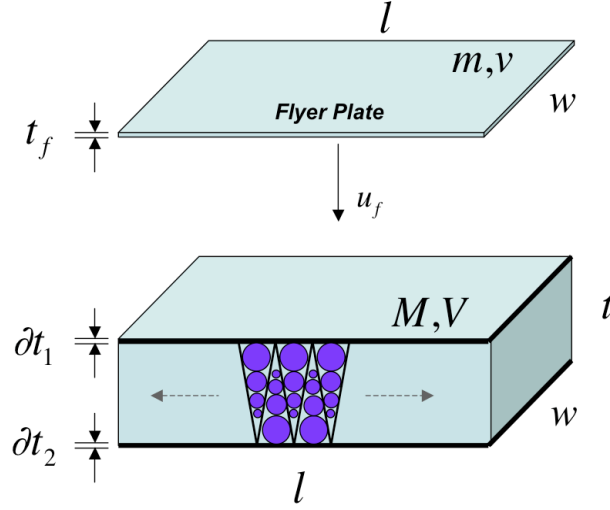


Figure 5.1: Schematic of what a tapered chain armor panel might look like.

**A tapered chain “armor panel” can be designed which consists of anti-parallel arrays of chains.**

Results indicate that impulses are attenuated regardless of the direction of propagation in a STC, therefore one could design a tapered chain “armor panel” by placing anti-parallel arrays within a supporting matrix. In that sense, the collective abilities of hundreds of such TCs could be combined. A schematic is outlined in figure 5.1. The quantities illustrated were used in order to obtain an estimate<sup>26</sup> of the specific absorbed energy of the panel and yielded results that are on the order of other technologies (i.e. up to 80 J/g). The value for the mass of the panel,  $M$ , however is highly subjective and the research needs to proceed to a more advanced experimental state in order to refine the calculation.

**Initial 3D simulations of STCs hint at continued energy absorption well beyond purely elastic behavior.**

Initial 3D, lagrangian simulations have begun using the modern and “massively” parallel hydrodynamics code, ALEGRA, developed by Sandia National Laboratories. Results suggest that while an increased impulse leads to plastic deformation, there are indications of continued energy absorption. Verification and validation studies as well as calibration of the global contact model needs to be performed.



**An expression for the period of a single particle in the overlap potential has been evaluated.**

Equation (1.11) quantifies the period of a single particle in the overlap potential, of arbitrary power  $n$  and input velocity,  $v_i$ .

**STCs do not equipartition energy but they do satisfy the virial theorem.**

Equipartition can be spoken of either at a system level or for individual particles. In the former, equipartition is not satisfied, but discrete systems with arbitrary  $n$  in the overlap potential were found to obey the virial theorem. At a particle level, certain chains showed a tendency to equally partition the available KE to all members after sufficient time had transpired.

**Even after long simulation time, STCs still fluctuate about the system's mean kinetic energy. They appear to settle into a quasi-equilibrium.**

While the mean value of KE in STCs was found to obey the virial theorem and particle velocities demonstrate a Gaussian profile, the system settles into a volatile state referred to as quasi-equilibrium. The fluctuations remain quite measurable even over long simulation time and their mean value has been quantified as a function of the number of particles and the exponent in the overlap potential (equation 2.13).

**A great number of questions still need to be investigated.**

In concluding this dissertation, I pose the following research areas for further study beyond the endless topics and questions that the 3D simulations pose.

- A close inspection of figure 2.23(a) for  $n = 2, 2.5$  indicates that equation (2.13) governing the decay in the mean fluctuations may not be sufficiently robust. It would be useful to run the simulations where  $N = 500$  or  $N = 10^3$  to improve the formulation. Also, why does  $\langle F \rangle$  appear to be independent of  $q$ ?
- Daraio<sup>23</sup> has experimentally verified shock absorption in chains where the material properties have been varied. What can be learned from numerical simulations, say for material and size variation?
- Is it possible to exploit the phenomenon of inelastic collapse for shock mitigation purposes?

- What is the proper way to characterize quasi-equilibrium? Should it be based on equilibrium conditions of a particular state of matter or combinations thereof?
- What does the stress-strain curve of a TC look like?
- What is the best filler material in a tapered chain armor panel?

# Appendix A

## STC Code from Pfannes<sup>80</sup>

```
/* PROGRAM taperchain.cpp
```

```
ORIGINAL VERSION: J.M.M. Pfannes
```

```
This program consideres an one dimensional chain of spheres that  
shrink succesively in radius ("tapered chain"). Initially the spheres  
are barely in contact, i. e. they just touch each other and are not  
compressed (zero loading).
```

```
The chain ends at both edges at fixed walls.
```

```
The program calculates the interaction of the system once disturbed  
by an instantaneous (delta) impulse exerted on one end of the chain.  
Restitution both between the spheres and between the edge spheres  
and the corresponding wall can be introduced.
```

```
The program does not consider gravity.
```

```
The EOM are solved with the Velocity Verlet algorithm.
```

```
scale of problem: mm-mg-musec (mimimu)
```

```
in this scale unit of force: 1000 N
```

```
in this scale unit of energy: 1 J
```

```
*/
```

```
#include <cmath>
```

```
#include <iostream>
```

```
#include <fstream>
```

```

#include <cstdlib>
#include <string>
#include <sstream>

using namespace std;

/***** ALTERABLE PARAMETER: *****/
const int nptles=20;    // total number of particles
const double rho=3.2 /* SiC (mg/mm^3) */, D=0.00326603139013 /* (mm^2/N) */;

const double rlarge = 5.0;    // (radius of large ptle (mm))
const double q = 0.0;        // (tapering factor (%))
const double xn = 2.5;        // (exponent in potential)
const double dt = 0.00001;    // (timestepwidth (musec))
const unsigned int nsteps = 100000000; // (# steps integration loop)
const int idiagp = 20000;      // (stepwidth diagnostics)
const int idump = 20000;       // (stepwidth dump)
const double vlin = 0.0;       // (initial v small ptle (mm/musec))
const double vnin = -0.01;     // initial v large ptle (mm/musec))
const double epsilon = 1.0;    // ((1 - restitution factor) all ptles)

/*****

ofstream readme("taperchain.readme");    // global scope fcts
ofstream EnergyImpulse("taperchain.EneImp");

void radii (double rlocal[]) {
    rlocal[nptles-1] = rlarge;
    if (q == 0)                // avoid roundoff errors w/out tapering
        for (int i = 0; i < nptles-1; i++)
            rlocal[i] = rlarge;
    else
        for (int i = 2; i < nptles+1; i++)
            rlocal[nptles-i] = rlocal[nptles-i+1] * (1 - q*0.01);

```

```

}

void masses (double r[], double masslocal[]) {
    const double pi = 4 * atan(1.0);
    const double masslarge = (4.0/3.0) * pi * rlarge*rlarge*rlarge * rho;
    masslocal[nptles-1] = masslarge;
    if (q == 0) // avoid roundoff errors w/out tapering
        for (int i = 0; i < nptles-1; i++)
            masslocal[i] = masslarge;
    else
        for (int i = 0; i < nptles-1; i++)
            masslocal[i] = r[i]*r[i]*r[i] * masslarge / (rlarge*rlarge*rlarge);
}

void strenghtfac (double r[], double alocal[]) {
    alocal[0] = (2.0 / (5.0 * D)) * (sqrt(r[0]));
    alocal[nptles] = (2.0 / (5.0 * D)) * (sqrt(r[nptles-1]));
    if (q == 0) // avoid roundoff errors w/out tapering
        for (int i = 1; i < nptles; i++)
            alocal[i] = (2.0 / (5.0*D)) * (sqrt(0.5*rlarge));
    else
        for (int i = 1; i < nptles; i++)
            alocal[i] = (2.0 / (5.0 * D)) * (sqrt((r[i]*r[i-1])/(r[i]+r[i-1]))));
}

// initialpos prints absolute initial positions, not for calculations
void initialpos (double r[], double xInitiallocal[]) {
    if (q == 0) // avoid roundoff errors w/out tapering
        for (int i = 0; i < nptles; i++)
            xInitiallocal[i] = (2.0*(i+1) - 1) * rlarge;
    else {
        xInitiallocal[0] = r[0];
        for (int i = 1; i < nptles; i++)

```

```

        xInitiallocal[i] = xInitiallocal[i-1] + r[i-1] + r[i];
    }
}

// absolutpos prints absolute positions to ptle files, not for calculations
void absolutpos (double r[], double x[],
double xInitial[], double xAbsolutlocal[]) {
    for (int i = 0; i < nptles; i++)
        xAbsolutlocal[i] = xInitial[i] + x[i];
}

void computeAccelerations (double x[], double a[], double r[],
double acc[], double overbefore[],
double mass[], double& pot) {

    pot = 0.0;          // every call calculates new pot contributions

    for (int i = 0; i < nptles; i++)    // zeroing all acc in every call
        acc[i] = 0.0;                // (= every timestep)

    /***** potential/force between neighboring ptles *****/
    for (int i = 0; i < nptles-1; i++) {
        if (x[i] > x[i+1]) {          // only when overlap
            double over = x[i] - x[i+1];
            double overnm1 = pow(over, (xn - 1.0));
            pot += over * overnm1 * a[i+1];
            double forceBetw = a[i+1] * xn * overnm1;

            double forceFactor;
            if (overbefore[i+1] < over)    // when compressing
                forceFactor = 1.0;
            else forceFactor = epsilon;    // when decompressing
        }
    }
}

```

```

    forceBetw *= forceFactor;

                                                                    // dim acc: force
    acc[i] -= forceBetw;                                           // sign(-): towards smaller x
    acc[i+1] += forceBetw;                                         // sign(+): towards larger x

    overbefore[i+1] = over;                                       // update for next timestep
}
else overbefore[i+1] = 0.0;                                       // reset when no overlap
}

/** potential/force between fixed wall (small, x=0) <-> small ptle **/
if (x[0] < 0) {
    double over = - x[0];
    double overnm1 = pow(over, (xn - 1.0));
    pot += over * overnm1 * a[0];
    double forceSmall = a[0] * xn * overnm1;

    double forceFactor;
    if (overbefore[0] < over)
        forceFactor = 1.0;
    else forceFactor = epsilon;

    forceSmall *= forceFactor;

    acc[0] += forceSmall;

    overbefore[0] = over;
}
else overbefore[0] = 0.0;

/** potential/force between fixed wall (large) <-> large ptle *****/
if (x[nptles-1] > 0) {
    double over = x[nptles-1];

```

```

    double overnm1 = pow(over, (xn - 1.0));
    pot += over * overnm1 * a[nptles];
    double forceLarge = a[nptles] * xn * overnm1;

    double forceFactor;
    if (overbefore[nptles] < over)
        forceFactor = 1.0;
    else forceFactor = epsilon;

    forceLarge *= forceFactor;

    acc[nptles-1] -= forceLarge;

    overbefore[nptles] = over;
}
else overbefore[nptles] = 0.0;

/***** real dim of acc: division by mass *****/
for (int i = 0; i < nptles; i++)
    acc[i] /= mass[i];
}

void velocityVerletStep (double x[], double v[], double acc[],
    double a[], double r[], double overbefore[],
    double mass[], double& pot) {

    for (int j = 0; j < nptles; j++) {
        x[j] += v[j] * dt + 0.5 * acc[j] * dt*dt;
        v[j] += 0.5 * acc[j] * dt;
    }

    computeAccelerations (x, a, r, acc, overbefore, mass, pot);

```



```

    for (int j = 0; j < nptles; j++)
        v[j] += 0.5 * acc[j] * dt;
}

void ptleHeader (ofstream* print, int k) {
    (* print) << "# ptle " << k+1 << ": time (musec)" << '\t' << "x (mm)"
        << '\t' << "v (mm/musec)" << '\t' << "a (mm/musec^2)"
        << '\t' << "kin. E. (J)" << '\t' << "f (kN)" << '\t'
        << "impulse (mg*mm/musec)" << '\t' << "xRelative (mm)" << '\n';
}

void dumpData (double t, double mass[], double v[], double acc[],
    double r[], double x[],          // scope absolutpos
    double xInitial[], double xAbsolut[],
    ofstream* print, int k) {

    double keDumpPt[nptles];    // new arrays for dumping data
    double vDumpPt[nptles];      // since arrays pass by argument
    double accDumpPt[nptles];    // dump data manipulated
    double xDumpPt[nptles];

    keDumpPt[k] = 0.5 * mass[k] * v[k]*v[k];
    if (keDumpPt[k] < 1.0e-20) keDumpPt[k] = 0.0; // set small values to zero

    vDumpPt[k] = v[k];
    if (vDumpPt[k] < 1.0e-20 && vDumpPt[k] > -1.0e-20) vDumpPt[k] = 0.0;

    accDumpPt[k] = acc[k];
    if (accDumpPt[k] < 1.0e-20 && accDumpPt[k] > -1.0e-20) accDumpPt[k] = 0.0;

    xDumpPt[k] = x[k];
    if (xDumpPt[k] < 1.0e-20 && xDumpPt[k] > -1.0e-20) xDumpPt[k] = 0.0;
}

```

```

absolutpos (r, x, xInitial, xAbsolut); // calculate absolute pos.

(* print) << t << '\t' << xAbsolut[k] << '\t' << vDumpPt[k] << '\t'
    << accDumpPt[k] << '\t' << keDumpPt[k] << '\t'
    << accDumpPt[k]*mass[k] << '\t'
    << mass[k]*vDumpPt[k] << '\t' << xDumpPt[k] << '\n';
}

void dumpEnergyImpulse (double t, double kelocal, double telocal, double pot,
double ptotallocal, double mass[], double v[]) {
    kelocal = 0.0;
    ptotallocal = 0.0;
    double absptotallocal = 0.0;           // scope only within function
    for (int j = 0; j < nptles; j++) {
        kelocal += mass[j] * v[j]*v[j];
        ptotallocal += mass[j] * v[j];
        absptotallocal += mass[j] * abs(v[j]);
    }
    kelocal *= 0.5;
    telocal = kelocal + pot;
    double potDump = pot;

    if (kelocal < 1.0e-20) kelocal = 0.0;    // set very small values to zero
    if (ptotallocal < 1.0e-20 && ptotallocal > -1.0e-20) ptotallocal = 0.0;
    if (telocal < 1.0e-20) telocal = 0.0;
    if (potDump < 1.0e-20) potDump = 0.0;
    if (absptotallocal < 1.0e-20) absptotallocal = 0.0;

    EnergyImpulse.precision(16);
    EnergyImpulse << t << '\t' << kelocal << '\t' << potDump << '\t'
    << telocal << '\t' << absptotallocal << '\t'
    << ptotallocal << '\n';
}

```

```

void readmeInfo (double ke, double pot, double te, double ptotat,
double kelin, double kenin, double plin, double pnin,
double r[], double xInitial[], double mass[],
double a[]) {

    readme << '\t' << ":-) *** TAPERCHAIN within walls *** (-:"
<< '\n' << '\n';

    readme << "parameter of this run: " << '\n' << '\n';
    readme << "total number of particles: " << '\t' << '\t' << nptles << '\n';
    readme << "density of particles (mg/mm^3): " << '\t' << rho << '\n';
    readme << "quantity D of particles (mm^2/N): " << '\t' << D << '\n';
    readme << "radius of large ptle (mm): " << '\t' << '\t' << rlarge << '\n';
    readme << "tapering factor (%): " << '\t' << '\t' << '\t' << q << '\n';
    readme << "exponent in potential: " << '\t' << '\t' << '\t' << xn << '\n';
    readme << "timestepwidth (musec): " << '\t' << '\t' << '\t' << dt << '\n';
    readme << "# steps integration loop: " << '\t' << '\t' << nsteps << '\n';
    readme << "stepwidth diagnostics: " << '\t' << '\t' << '\t' << "every "
<< idiagp << " timesteps" << '\n';
    readme << "stepwidth dump: " << '\t' << '\t' << '\t' << "every "
<< idump << " timesteps" << '\n';

    readme << "initial v small ptle (mm/musec): " << '\t' << vlin << '\n';
    readme << "initial v large ptle (mm/musec): " << '\t' << vnin << '\n';
    readme << "restitution factor for all ptles: " << '\t' << 1-epsilon << '\n'
<< '\n';

    readme << "total length of run (musec): " << '\t' << dt * nsteps << '\n';
    readme << "total rows recorded for .EneImp file: " << '\t' << '\t'
<< nsteps/idiagp +1 << '\n';

    readme << "total rows recorded for particle files: " << '\t'
<< nsteps/idump +1 << '\n' << '\n';

    readme << "Initial system info (t=0): " << '\n' << '\n';
    readme << "kin. E. (J)" << '\t' << "pot. E. (J)" << '\t'
<< "tot. E. (J)" << '\t' << "total impulse (mg*mm/musec)" << '\n';

```

```

    readme << ke << '\t' << pot << '\t' << te << '\t' << ptotal
<< '\n' << '\n';

    readme << "kin. E. of small particle (J): " << '\t' << '\t' << ke1in
<< '\n';

    readme << "kin. E. of large particle (J): " << '\t' << '\t' << kenin
<< '\n';

    readme << "impulse of small particle (mg*mm/musec): " << '\t'
<< p1in << '\n';

    readme << "impulse of large particle (mg*mm/musec): " << '\t'
<< pnin << '\n' << '\n';

    readme << "particle radii (mm): " << '\n';
    for (int i=0; i < nptles; i++) {
        readme << r[i] << '\t';
    }
    readme << '\n' << '\n';

    readme << "initial particle positions (mm): " << '\n';
    for (int i=0; i < nptles; i++) {
        readme << xInitial[i] << '\t';
    }
    readme << '\n' << '\n';

    readme << "total length of one dimensional alignment (mm): " << '\t'
<< xInitial[nptles-1] + r[nptles-1] << '\n' << '\n';

    readme << "particle masses (mg): " << '\n';
    for (int i=0; i < nptles; i++) {
        readme << mass[i] << '\t';
    }
    readme << '\n' << '\n';

    readme << "particle interaction strenghts (0.0316*N/mm^(3/2)): " << '\n';
    for (int i=0; i < nptles+1; i++) {
        readme << a[i] << '\t';
    }
    readme << '\n';
}

```

```

int main ( ) {

    double r[nptles], x[nptles], xAbsolut[nptles], xInitial[nptles],
           v[nptles], acc[nptles], mass[nptles], a[nptles+1],
           overbefore[nptles+1], pot;

    /***** functions *****/
    radii (r);
    masses (r, mass);
    strenghtfac (r, a);
    initialpos (r, xInitial);

    /***** output files *****/
    /***** ptle-files *****/
    ofstream print [nptles];
    for (int k = 0; k < nptles; k++) {

        string filename;
        ostringstream buffer;

        buffer << "taperchain_" << k+1 << ".dat";
        filename = buffer.str();

        print[k].open(filename.c_str()); // convert string to char
    }

    for (int k = 0; k < nptles; k++) // header for particles
        ptleHeader(& print[k], k);
    /*****/

```

```

// header for .EneImp file

EnergyImpulse << "# time" << '\t' << "kin. E. (J)" << '\t'
<< '\t' << "pot. E. (J)" << '\t' << '\t'
<< "total E. (J)" << '\t' << '\t'
<< "|(total imp.)| (mg*mm/musec)" << '\t'
<< "total imp. (mg*mm/musec)" << '\n';

/*****/

for (int i = 0; i < nptles; i++) {    // zeroing
    x[i] = 0.0;          // relative particle positions for calculation
    v[i] = 0.0;
    acc[i] = 0.0;
    overbefore[i] = 0.0;
}
overbefore[nptles] = 0.0;
double t = 0.0;

v[0] = vlin;                // mind special input data
v[nptles-1] = vnin;

/***** initial energy info *****/
double ke1in = 0.5 * mass[0] * v[0]*v[0];    // initial kE of edge ptles
double kenin = 0.5 * mass[nptles-1] * v[nptles-1]*v[nptles-1];
double p1in = mass[0] * v[0];    // initial impulse of edge particles
double pnin = mass[nptles-1] * v[nptles-1];

computeAccelerations (x, a, r, acc, overbefore, mass, pot);

// call for initial potential energy

double ke = 0.0;                // checking for initial system energy
double ptotal = 0.0;
for (int i = 0; i < nptles; i++) {
    acc[i] = 0.0;    // reset acc for verlet in case of initial overlap

```

```

    ke += mass[i] * v[i]*v[i];
    ptotal += mass[i] * v[i];
}

ke *= 0.5;

double te = pot + ke;                                // initial total system energy

readmeInfo (ke, pot, te, ptotal, ke1in, kenin, p1in, pnin,
            r, xInitial, mass, a);

/***** begin of timestep loop *****/
for (unsigned int i = 0; i < nsteps+1; i++) {

    t = i * dt;

    velocityVerletStep (x, v, acc, a, r, overbefore, mass, pot);

    /***** check system energy, plot data *****/
    if ((i % idiagp) == 0) {
        dumpEnergyImpulse(t, ke, te, pot, ptotal, mass, v);
    }

    /***** check particle energy, plot data *****/
    if ((i % idump) == 0) {
        for (int k = 0; k < nptles; k++) {
            dumpData(t, mass, v, acc,                // scope dumpData
                    r, x, xInitial, xAbsolut,        // scope absolutpos
                    & print[k], k);
        }
    }
}

} /***** end of timestep loop *****/

readme.close();
EnergyImpulse.close();

```

```
for (int k = 0; k < nptles; k++) // closing particle files
    print[k].close();
}
```



# Appendix B

## DTC Code Modifications

```

/***** ALTERABLE PARAMETER: *****/
int nptles = 3;    // total number of particles
const double f = 0.9;    // fractional size of interstitial grain w.r.t last grain
const double rho=4.42; // TiAlV (mg/mm3)
const double D = 0.01206; // TiAlV (mm2/N)

const double rlarge = 5.0;    // (radius of large ptle (mm))
const double q = 0.0;    // (tapering factor (%))
const double xn = 2.5;    // (exponent in potential)
const double dt = 0.00001;    // (timestepwidth (musec))
const unsigned int nsteps = 100000000; // (# steps integration loop)
const int idiagp = 20000;    // (stepwidth diagnostics)
const int idump = 20000;    // (stepwidth dump)
const double vlin = 0.0;    // (initial v small ptle (mm/musec))
const double vnin = -0.01;    // initial v large ptle (mm/musec))
const double epsilon = 1.0;    // ((1 - restitution factor) all ptles)

/*****

ofstream readme("taperchain.readme");    // global scope fcts
ofstream EnergyImpulse("taperchain.EneImp");

// Generate radii and masses for DTC
void spheres (double rlocal[], double masslocal[]) {
    rlocal[nptles-1] = rlarge; // shifts everything to index starting at zero
    double tapering = 1 - q*0.01;

```

```

    const double pi = 4 * atan(1.0);
    const double masslarge = (4.0/3.0) * pi * pow(rlarge,3) * rho;
    masslocal[nptles-1] = masslarge;
    if (q==0 && f==1.0) // Monodisperse in DTC
    for (int i=0; i<nptles-1; i++) {
rlocal[i]    = rlarge;
masslocal[i] = masslarge;
        }

    else if (q==0) { // Quasi-Monodisperse: Avoid roundoff errors without tapering
        for (int i=1; i<nptles-1; i=i+2) { // Interstitial grains
rlocal[i] = rlarge*f;
masslocal[i] = (4.0/3.0) * pi * pow(rlocal[i],3) * rho;
        }

        for (int i=0; i<nptles-1; i=i+2) { // Non-interstitial grains
rlocal[i] = rlarge;
masslocal[i] = masslarge;
        }
    }

    // non-monodisperse chains
    else {
        for (int i=1; i<nptles-1; i=i+2) { // Find radii of interstitial grains
            rlocal[i] = f*pow(tapering,(nptles-1)/2)*rlarge;
            masslocal[i] = (4.0/3.0) * pi * pow(rlocal[i],3) * rho;
        }

        for (int i=nptles-1; i>=0; i=i-2) { //Find radii of non-interstitital grains
            rlocal[i-2] = rlocal[i] * tapering;
masslocal[i-2] = (4.0/3.0) * pi * pow(rlocal[i-2],3) * rho;
        }
    }
}

void strenghtfac (double r[], double alocal[]) {
    alocal[0] = (2.0 / (5.0 * D)) * (sqrt(r[0]));
}

```

```

    alocal[nptles] = (2.0 / (5.0 * D)) * (sqrt(r[nptles-1]));
    if (q == 0 && f == 1.0) // avoid roundoff errors w/out tapering
        for (int i = 1; i < nptles; i++)
            alocal[i] = (2.0 / (5.0*D)) * (sqrt(0.5*rlarge));
    else
        for (int i = 1; i < nptles; i++)
            alocal[i] = (2.0 / (5.0 * D)) * (sqrt((r[i]*r[i-1])/(r[i]+r[i-1]))));
}

// initialpos prints absolute initial positions, not for calculations
void initialpos (double r[], double xInitiallocal[]) {
    if (q == 0 && f == 1.0 ) // avoid roundoff errors w/out tapering
        for (int i = 0; i < nptles; i++)
            xInitiallocal[i] = (2.0*(i+1) - 1) * rlarge;
    else {
        xInitiallocal[0] = r[0];
        for (int i = 1; i < nptles; i++)
            xInitiallocal[i] = xInitiallocal[i-1] + r[i-1] + r[i];
    }
}

```

# Appendix C

## PERL Code

```
#!/usr/bin/env perl

# This program automates the considerable task of setting up parametric studies on the tapered
# spherical elastic 1-D grain problem. It takes an input file: taperchain29.cpp and searches
# through it replacing the values of epsilon, q, and N in for loops and spitting out a file
# in the appropriate directory. The directories are created on the fly.
# This version uses the updated directories and is looking at initial velocity on the small
# grain.

$w = 0.1;

$FILE_NAME = "taperchain28_w01.cpp";
$SOURCE_DIR = "/home/rldoney";
##$SOURCE_DIR = "/Users/bob/Work/Classes/Spring 2004/Dr. Sen study/runs";
$FILE_IN = "$SOURCE_DIR/$FILE_NAME";
$OUT_DIR = "/nfs/scratch/rldoney/TiAlV/D.SimpleTapered";
##$OUT_DIR = "$SOURCE_DIR/TiAlV/D.SimpleTapered/D.Vin_large/";
$EPSILON_CHK = "const double epsilon ="; # Set pattern to match line with epsilon
$Q_CHK = "const double q ="; # Set pattern to match line with q
$N_CHK = "int nptles="; # Set pattern to match line with N

system("clear"); # clear the screen;

#for($w = 0.0; $w<=0.02; $w+=0.01) { # Restitution
$epsilon = 1.0 - $w; # taperchain.cpp program uses epsilon instead of w directly
print"\n\n::::: w=$w \t epsilon = $epsilon ::::::\n";
```

```

system("date '+DATE: %m/%d/%y%nTIME: %H:%M:%S'");
print"\n";
chdir("$OUT_DIR") or die "Cant open $OUT_DIR";
mkdir("w$w");
chdir("w$w") or die "Cant open $OUT_DIR/w$w";

for($N=3; $N <=20; $N++) {
    mkdir("N$N");
    chdir("N$N") or die "Cant open N$N";

for($q=0; $q <=10; $q++) {
    mkdir("N$N\q$q");
    chdir("N$N\q$q") or die "Cant open N$N\q$q";
    $CURRENT_DIR = `pwd`;
chop($CURRENT_DIR); # remove trailing \n
print"Current Dir: $CURRENT_DIR\n";
$FILE_OUT= "$CURRENT_DIR/$FILE_NAME";
open(FROM, "$FILE_IN") or die "Cant open $FILE_IN: $!";
open(TO, ">$FILE_OUT") or die "Cant open $CURRENT_DIR/$FILE_OUT: $!";
print" ";
system("date '+TIME: %H:%M:%S'");

while(<FROM>) { # Read in the file line by line into $_

    # Replacements (Regular expression matching)
    if($w != 0) {
        s/$EPSILON_CHK \d+\.\.d+/$EPSILON_CHK $epsilon/; # change epsilon
    }

    s/$N_CHK\d+/$N_CHK $N/; # change N
    s/$Q_CHK \d+\.\.d+/$Q_CHK $q\./; # change q

print TO $_; # Write the current line with any changes to TO

```

```

    close T0;
}

close FROM;

# Escape to the shell, compile the file, and run it
# It was unexpected, but we need the ' ' because of the spaces in the path
system ("g++ '$FILE_OUT'");
system ("./a.out");
    chdir("../");
}

    chdir("../");
    print("\n");
}

system("date '+DATE: %m/%d/%y%nTIME: %H:%M:%S'");

```

## Appendix D

# Energy partitioning in the DTC

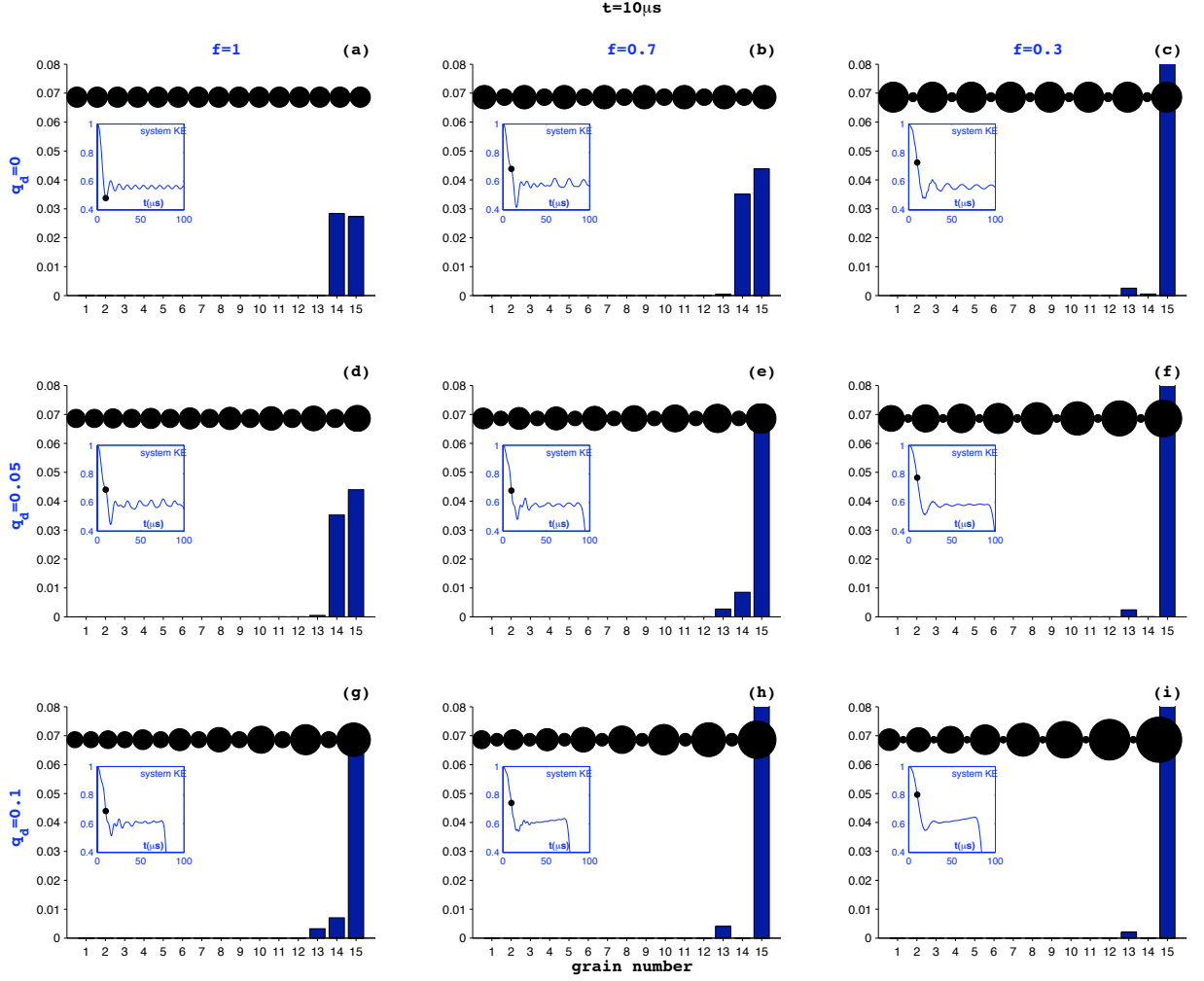


Figure D.1: Instantaneous kinetic energy per grain for various DTC configurations at  $t = 10\mu s$  where  $q_d = \{0, 0.05, 0.1\}$  and  $f = \{1.0, 0.7, 0.3\}$ .



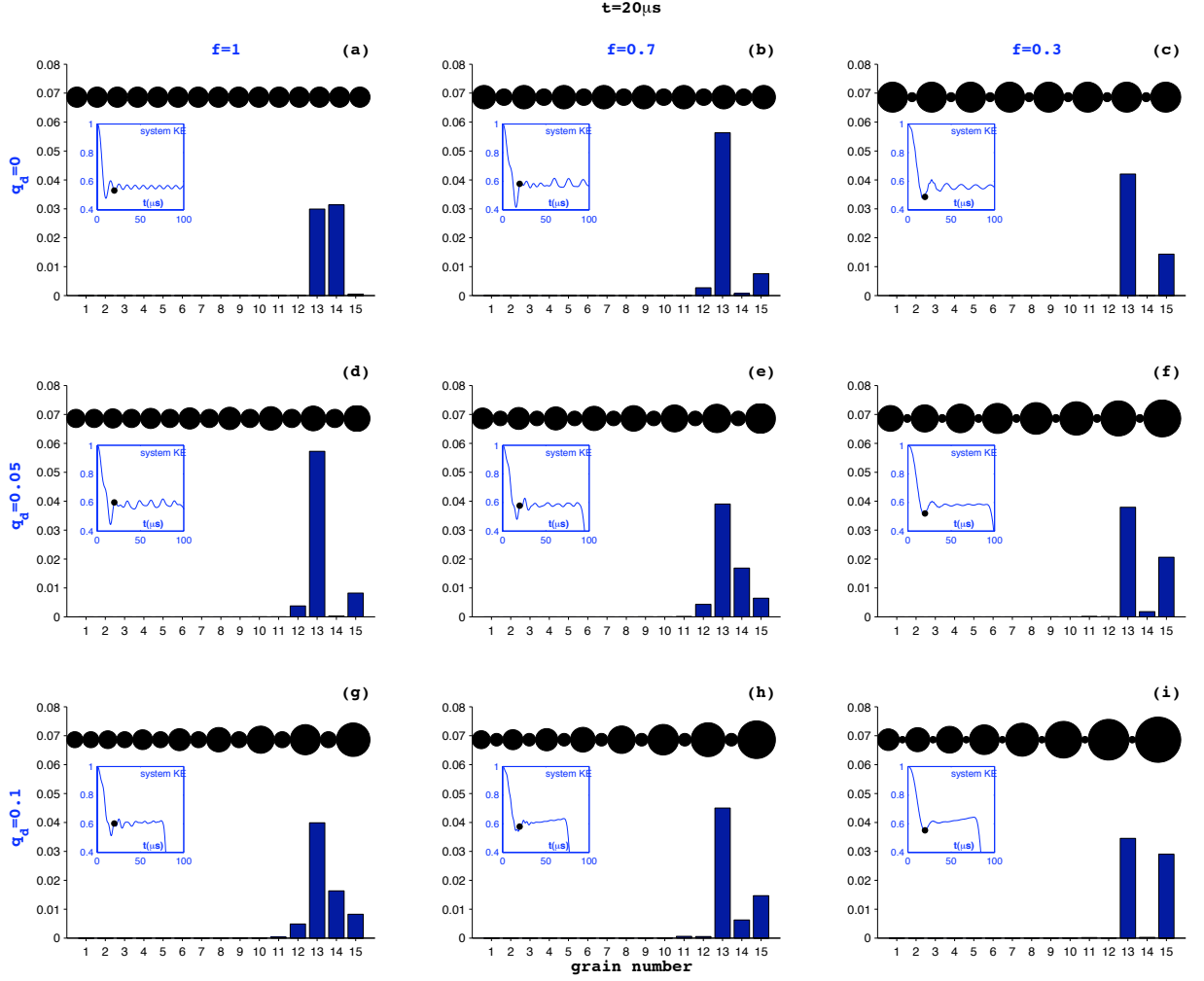


Figure D.2: Instantaneous kinetic energy per grain for various DTC configurations at  $t = 20\mu s$  where  $q_d = \{0, 0.05, 0.1\}$  and  $f = \{1.0, 0.7, 0.3\}$ .

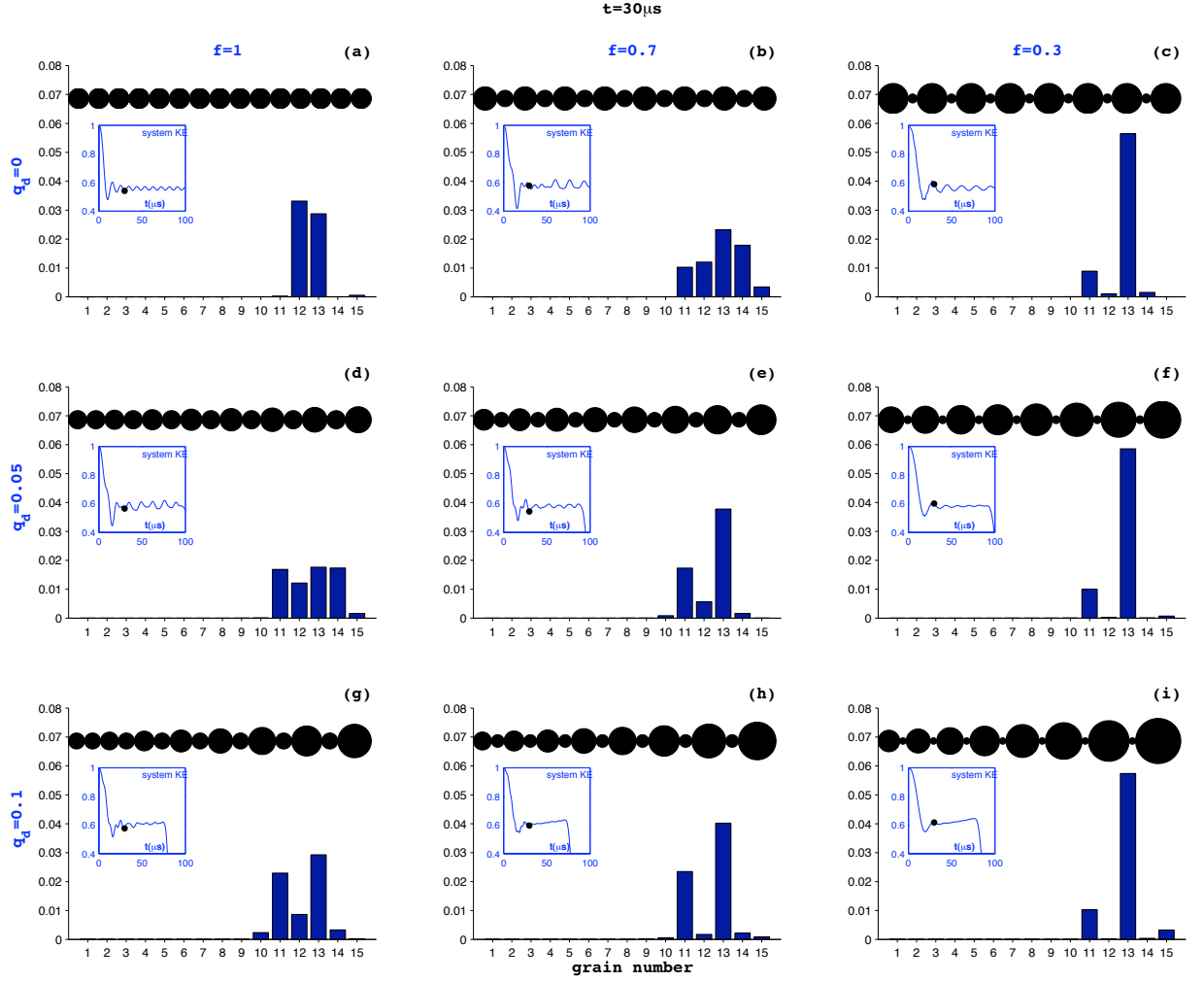


Figure D.3: Instantaneous kinetic energy per grain for various DTC configurations at  $t = 30 \mu s$  where  $q_d = \{0, 0.05, 0.1\}$  and  $f = \{1.0, 0.7, 0.3\}$ .

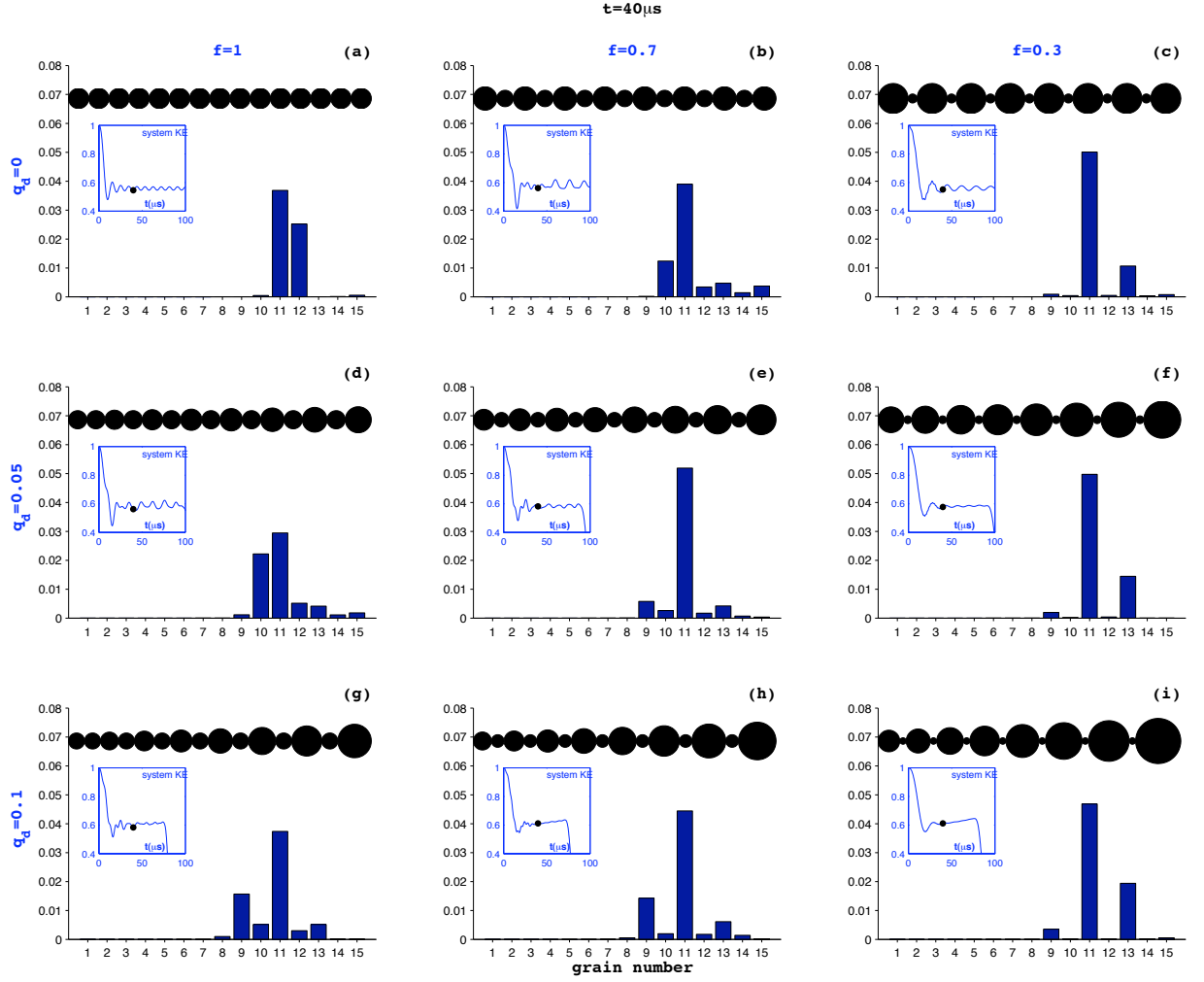


Figure D.4: Instantaneous kinetic energy per grain for various DTC configurations at  $t = 40 \mu s$  where  $q_d = \{0, 0.05, 0.1\}$  and  $f = \{1.0, 0.7, 0.3\}$ .

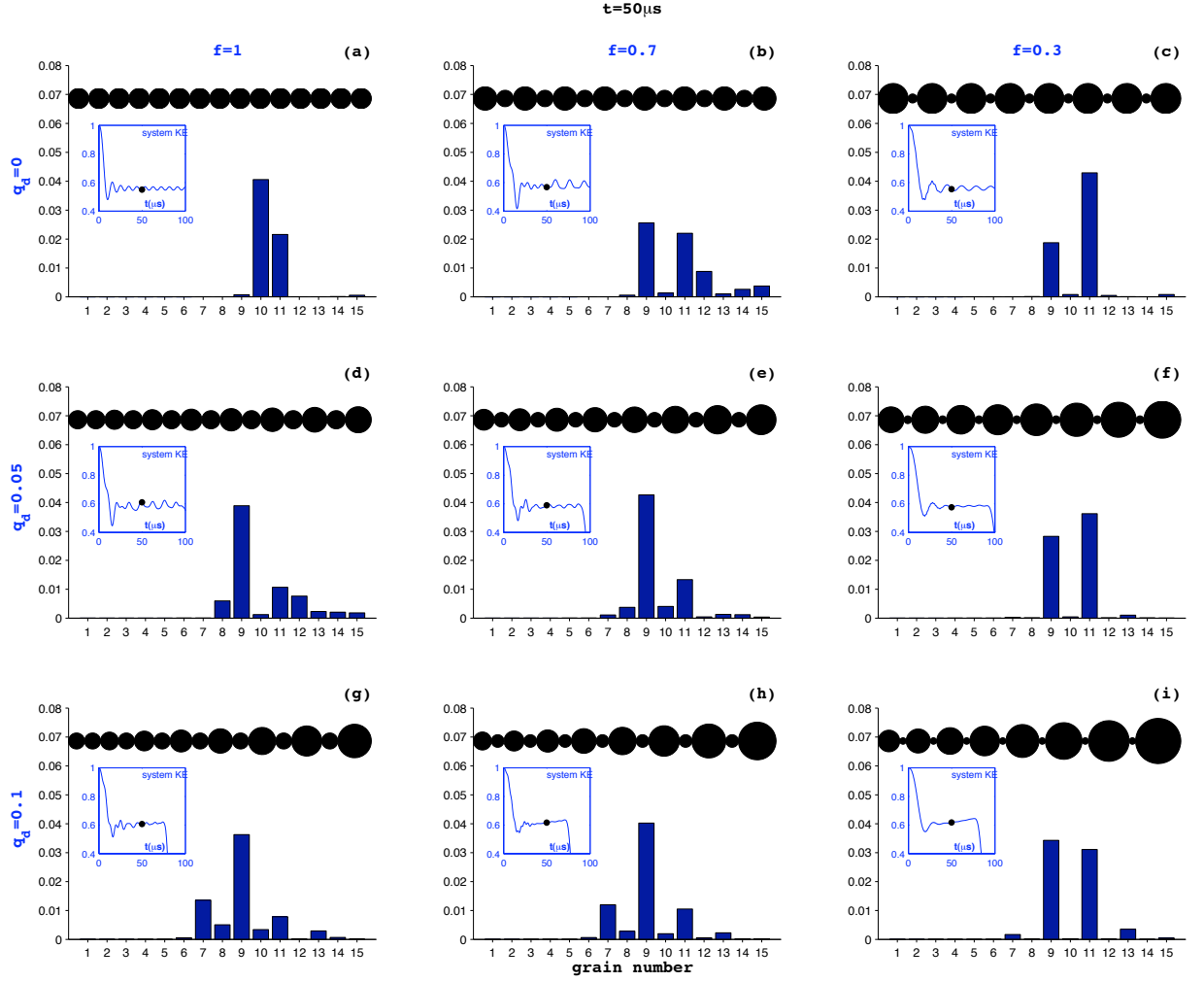


Figure D.5: Instantaneous kinetic energy per grain for various DTC configurations at  $t = 50 \mu s$  where  $q_d = \{0, 0.05, 0.1\}$  and  $f = \{1.0, 0.7, 0.3\}$ .

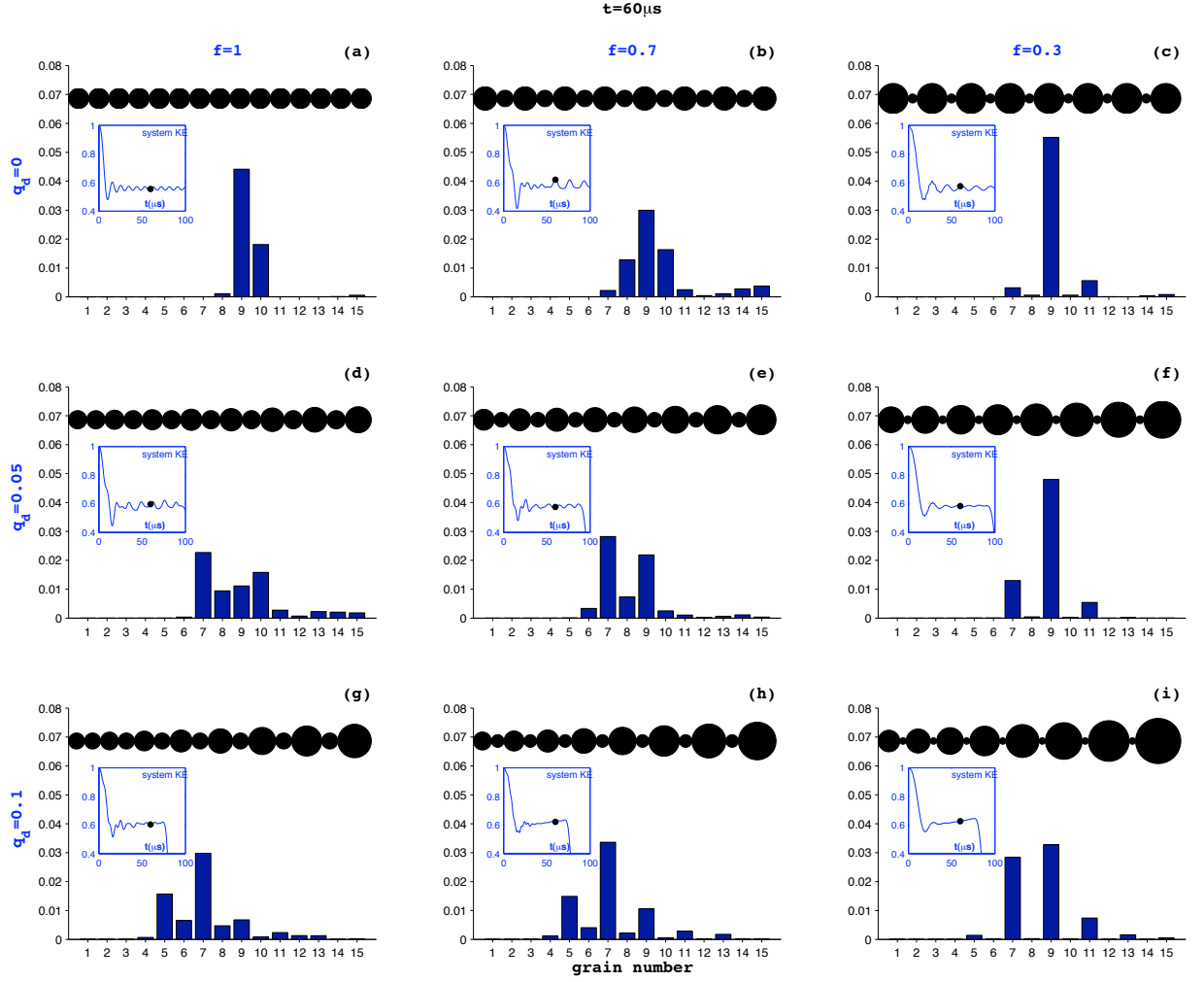


Figure D.6: Instantaneous kinetic energy per grain for various DTC configurations at  $t = 60 \mu s$  where  $q_d = \{0, 0.05, 0.1\}$  and  $f = \{1.0, 0.7, 0.3\}$ .

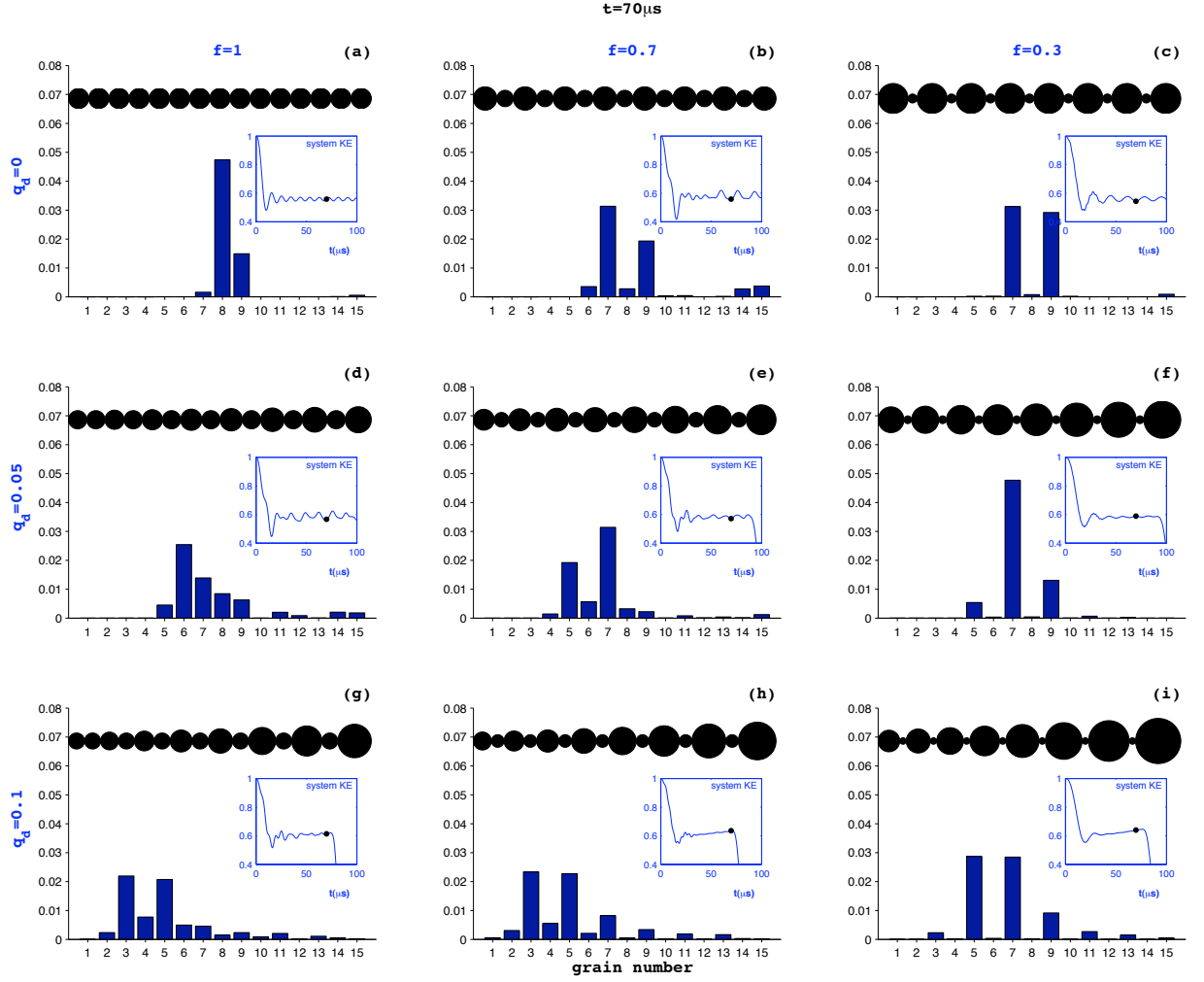


Figure D.7: Instantaneous kinetic energy per grain for various DTC configurations at  $t = 70 \mu s$  where  $q_d = \{0, 0.05, 0.1\}$  and  $f = \{1.0, 0.7, 0.3\}$ .

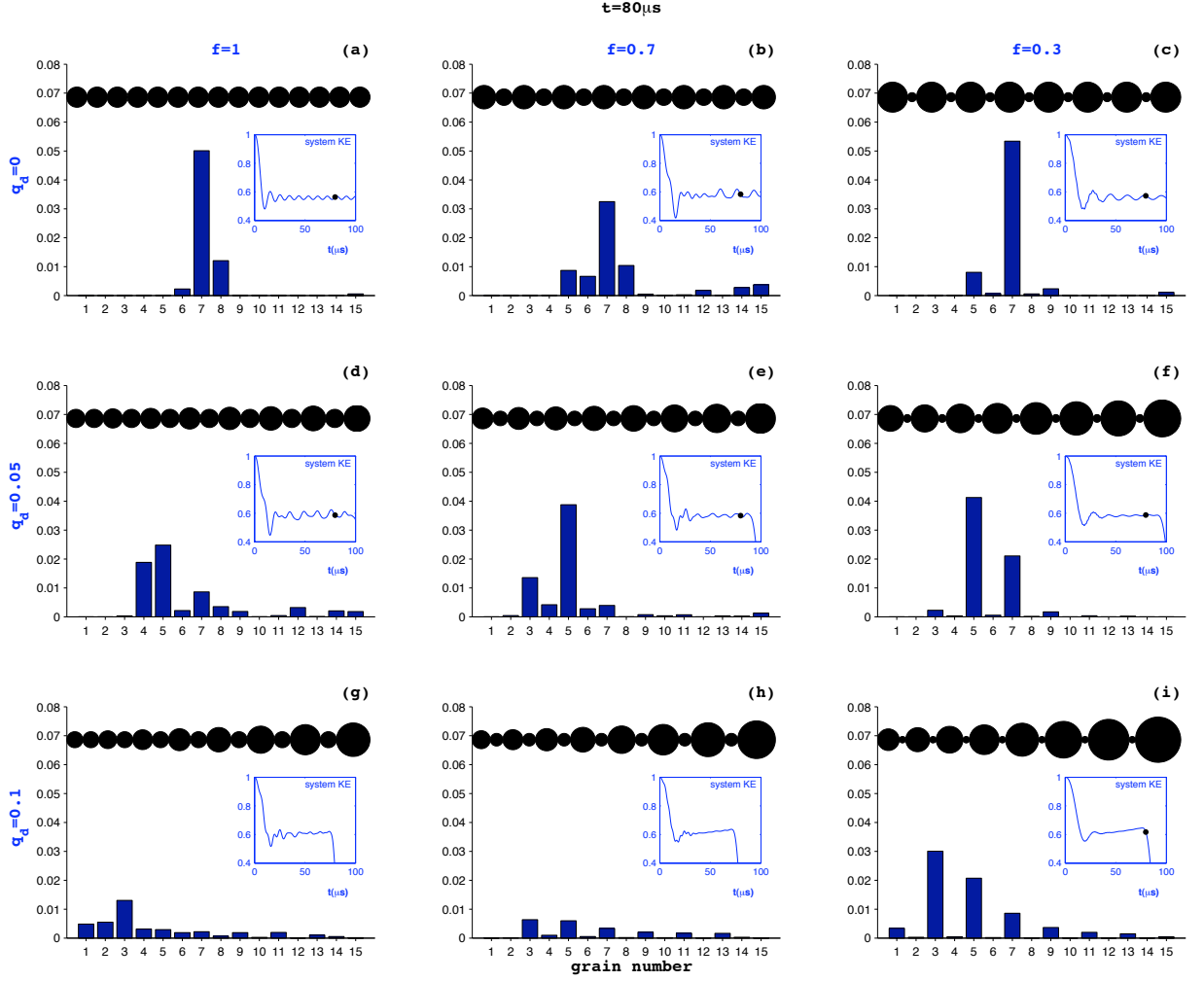


Figure D.8: Instantaneous kinetic energy per grain for various DTC configurations at  $t = 80 \mu s$  where  $q_d = \{0, 0.05, 0.1\}$  and  $f = \{1.0, 0.7, 0.3\}$ .

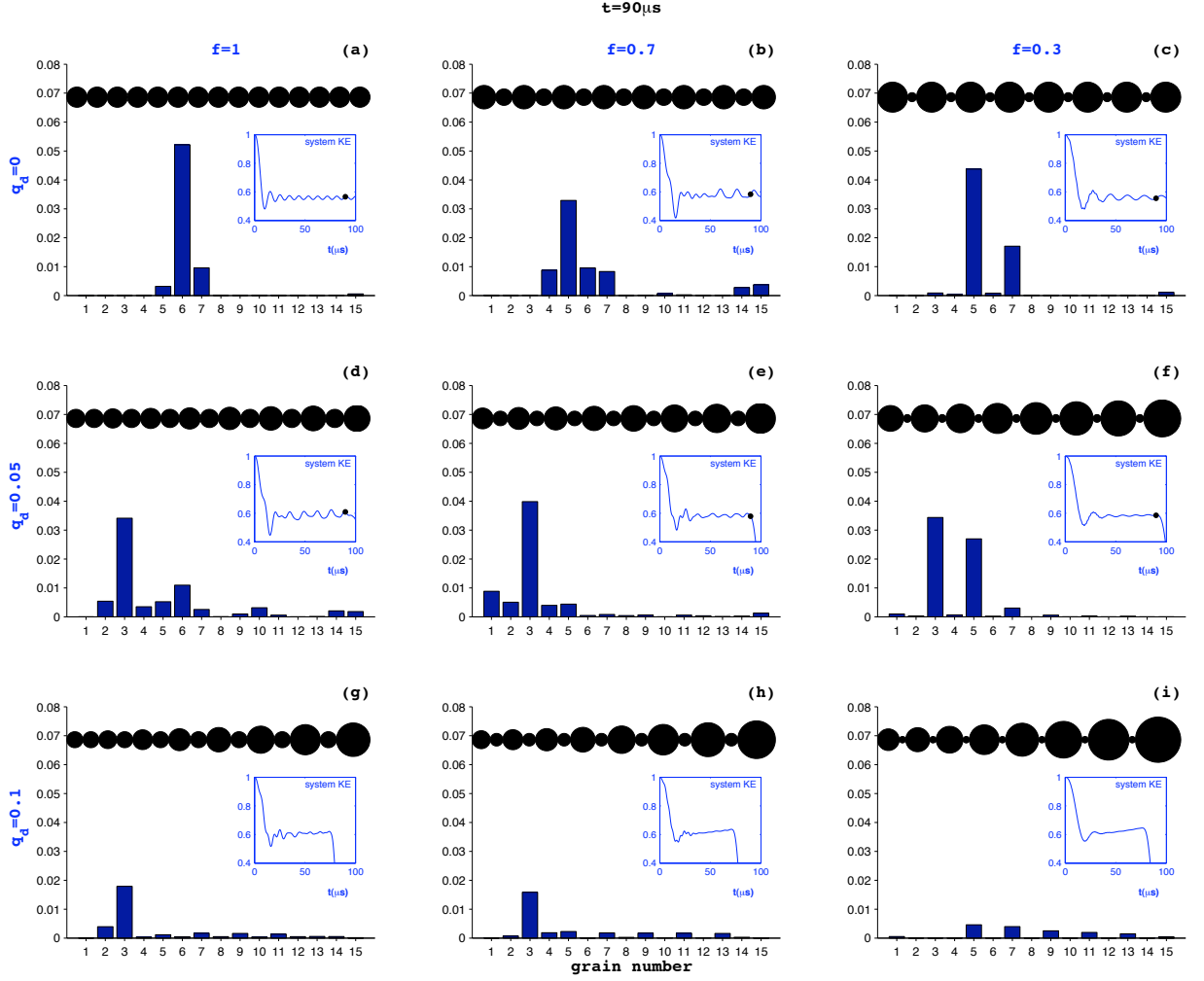


Figure D.9: Instantaneous kinetic energy per grain for various DTC configurations at  $t = 90 \mu s$  where  $q_d = \{0, 0.05, 0.1\}$  and  $f = \{1.0, 0.7, 0.3\}$ .



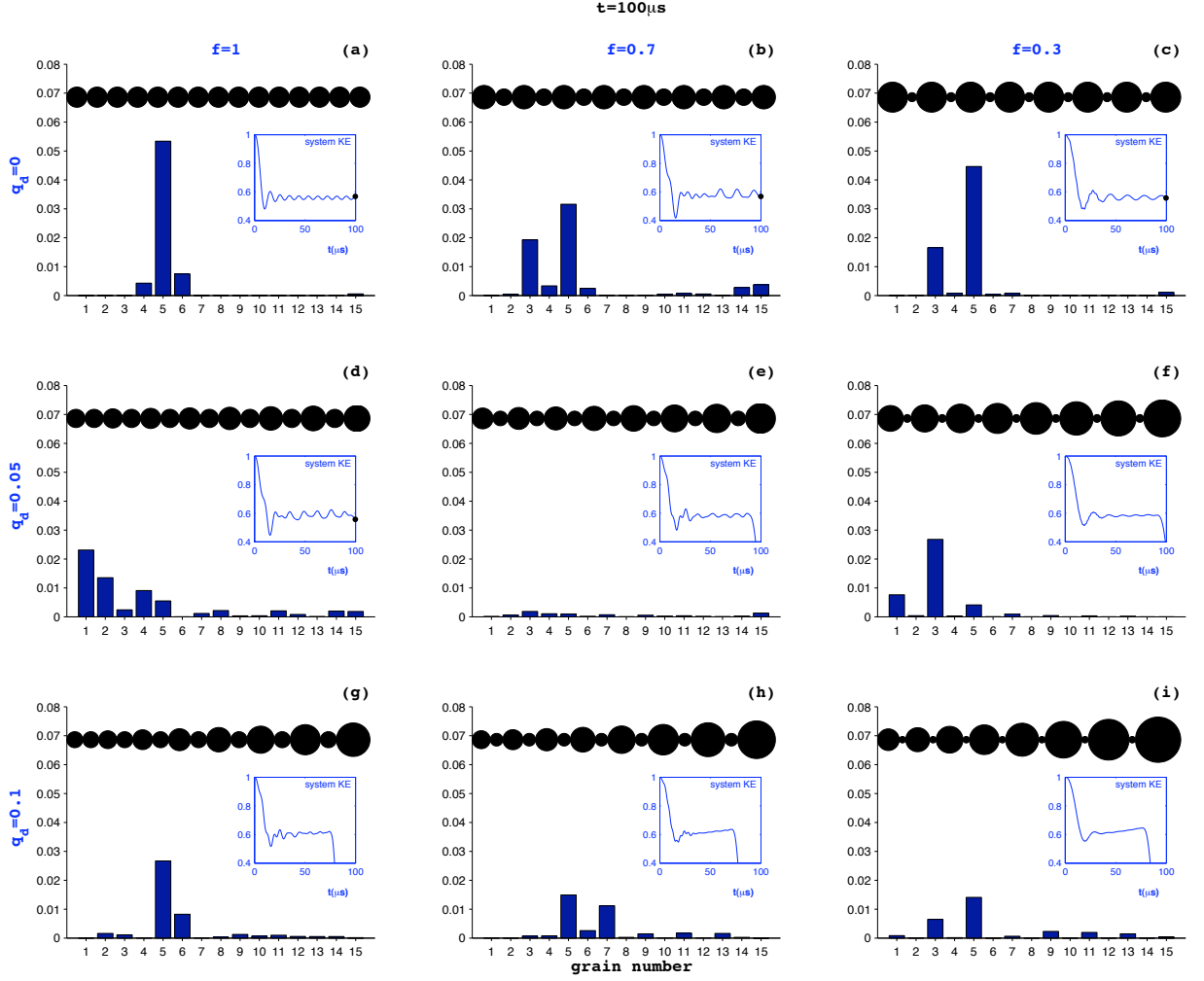


Figure D.10: Instantaneous kinetic energy per grain for various DTC configurations at  $t = 100\mu\text{s}$  where  $q_d = \{0, 0.05, 0.1\}$  and  $f = \{1.0, 0.7, 0.3\}$ .

# Appendix E

## Normalization

Normalization has posed some challenges in trying to properly assess the absorption quality of a simple tapered chain (STC). Proper normalization schemes will help the architect better determine which STC is best for which application. Recall that the goal is to measure the energy at the last grain versus the energy put into the system by the first. In general, the functional form will stay the same regardless of the strategy and adjustments in the normalization will simply scale the kinetic energy (KE) surface. In some cases, the output force of each chain is based on the maximum value felt by any possible chain under consideration (i.e. monodisperse and no energy loss)<sup>1</sup>. This gives a measure of how one chain is better than another.

In this communication, we have chosen to form the ratio based on the output KE and force felt by each specific chain. This serves to grade the individual effectiveness of any chain without reference to another. In choosing a peak value with this method, one could identify either when the impulse first hits the last grain or look for the absolute maximum peak whenever it may occur. We have chosen to use the former for several reasons. First, it ignores the complexity of nonlinear reverberations which can lead to large peaks at unpredictable times. Second, we argue that this is just as realistic as selecting the maximum value anywhere in the time spectrum.

It turns out that in most cases, the absolute maximum is the first peak. There are special cases where the maximum may occur at later times and this needs to be investigated further. In figure 2.5 (in the body of the report) for  $q = 0.1$ , for example, we see the striking occurrence of the secondary pulse about  $225 \mu s$  being much stronger than the initial arrival at  $35 \mu s$ . This is one of those instances that disagrees with the way we choose to normalize our KE surfaces. We have investigated this particular case further without including extraneous plots and report the following observations. The effect exists for  $N = 15 - 20$  for constant  $\omega$ . When  $N = 20$  is held fixed and restitution is increased, the peak KE once again occurs for the first arrival of the pulse. As  $q$  increases, so do the number of collisions and the requisite energy loss (since  $\omega \neq 0$ ). Therefore, it is less likely to find a global peak later in the simulation. The situation is further complicated by the interplay between  $q$

---

<sup>1</sup>Pfannes, J. *Energy propagation in granular chains* M.S. Thesis, SUNY Buffalo, May 2003.

and  $\omega$ .

# Appendix F

## CUBIT script for 3D STC

```
# This is a cubit script to generate a Simple
# Tapered Chain (STC).

# units are in mm
#{scalef = 1.0e-3}

#{N      = 5}          ## Number of grains
#{n      = N-1}        ## used only for loop control
#{nn     = N+1}        ## For vertices
#{Ri     = 5.0}        ## Largest grain radius
#{q      = 0.07}       ## tapering (percentage)
#{nr     = 6}          ## No. of radial divisions
#{ntheta = 40}         ## No. of azimuthal divisions (must be multiple of 8)
#{wall_length = Ri*2}  ## Length of wall boundary along x
#{wall_y   = Ri*2}    ## Transverse y size of wall
#{wall_z   = wall_y}  ## Transverse z size of wall

graphics mode wire
create sphere radius {Ri}

#{rold = Ri}          ## Set the initial r_old
#{xold = 0}           ## Initial center of 1st grain
#{i = 1}              ## counter for cubit body number

{loop(n)}              ## can't loop over algebraic ops
    #{i = i +1}
    #{rnew = rold * (1.0-q)}  ## determine size of next grain
```

```

    #{xnew = xold + rold + rnew} ## find position of next grain
    create sphere radius {rnew}

    body {i} move {xnew} 0 0      ## move the grain along x
    #{rold = rnew}                ## update values and prepare
    #{xold = xnew}                ## for next new values
{EndLoop}

#{edge= xnew + rnew}            ## position of far side of chain
#create vertex {edge} 0 0

create brick x {wall_length} y {wall_y} z {wall_z}
body {nn} move {wall_length/2.0 + edge} 0 0
body {nn} size 1.0
mesh volume {nn}

#merge all

#{i = 0}
{loop(N)}
    #{i =i+1}
    volume {i} scheme sphere graded_interval {nr} Az_interval {ntheta} fraction 0.7
    mesh volume {i}
    volume {i} smooth scheme laplacian
    smooth volume {i}
{EndLoop}

## Scale -----
Transform Mesh Output scale {scalef}

## BLOCK ASSIGNMENT: spheres + block -----
#{i = 0}
{loop(nn)}
    #{i =i+1}
    block {i} volume {i}

```

```

{EndLoop}

### BCs -----
#{i = 0}
{loop(N)}
    #{i =i+1}
    nodeset {i}0 surface {i}
{EndLoop}

#{i = 0}
{loop(N)}
    #{i =i+1}
    sideset {i}0 surface {i}
{EndLoop}

## Block-sphere interface: that surface always seems to be N+4
nodeset 999 surface {N+4}
sideset 999 surface {N+4}

mesh visibility off

disp

export genesis 'stc.gen' overwrite

```

# Appendix G

## ALEGRA script for 3D STC

```
$$$ Alegra input script for STC dynamics
$$$
$$$ Bob Doney
$$$ 10.29.2004
$$$
$$$ 05.30.2006  updated to 3d lagrange
$$$
$$$ -----
$$$ ----- Grain setup-----
${scalef = 1.0e-3}    ## Scale SI to mm
${N       = 5}        ## Number of grains
${n       = N-1}
${nn      = N+1}
${Ri      = 5.0*scalef} ## Largest grain radius
${q       = 0.07}      ## tapering (percentage)

title: STC

units, si

termination cycle, 1

$$$termination time, 1000.0e-6

solid dynamics

cartesian 3d
```

```

ignore kinematic errors

domain

  remesh iterations 10

  remap iterations 1

  mhis advection

  smyra interface tracker
$$$  slic interface tracker

  initial remesh movement limiter 0.005

  remesh movement ratio 1.025

  remesh movement limiter 0.4

end

$$$ --- Attempt to use boundaries as walls that constrain the chain

no displacement, sideset 999, x

$$$ GLOBAL CONTACT --- using SNL input to start with
global contact $$$ for 3D applications
${j=1}
{loop(N)}
  ${i=j*10}
    sideset {i}
  ${j=j+1}
{EndLoop}

sideset 999

package = acme

search algorithm = augmented dynamic search

enforcement algorithm = td enforcement

enforcement iterations = 20

default data

  kinematic partition = auto

```



```

friction model id = 1
search normal tolerance = .0001
search tangential tolerance = .0001
end
friction model 1 frictionless
    $no subkeywords
end
end

initial block velocity: block 1, x 500.0
maximum initial time step 1.0e-9

$$$ TRACER PARTICLES
tracer points
    lagrangian tracer 1 x=0 y=0 z=0      $$$ Initial one at origin

    ${rold = Ri}                        $$$ Set the initial r_old
    ${xold = 0}                         $$$ Initial center of 1st grain
    ${i=0}
    $$$ Center of spheres
    {loop(n)}                           $$$ N-1
        ${i = i+1}
        ${rnew = rold * (1.0-q)}        $$$ determine radius of next grain
        ${xnew = xold + rold + rnew}

    lagrangian tracer {i+1} x = {xnew} y=0 z=0

    ${rold = rnew}                      $$$ update values and prepare
    ${xold = xnew}                      $$$ for next new values
{EndLoop}

$$$ Wall-last sphere interface

```

```

    lagrangian tracer {nn} x= {xnew+rnew} y=0 z=0

end          $$$ End tracer section


    $$$ MESH
    ${i=0}
    {loop(nn)}
        ${i=i+1}
        block {i}
            LAGRANGIAN MESH
            material {i}
        #    hourglass control {i}
        end
    {EndLoop}


end          $$$ -- end physics --


$$$ -----
$$$ --- PLOTTING ---
$$$double precision exodus
emit output, time interval=1.e-6
emit plot, time interval=1.e-6
emit hisplt, time interval=0.2e-6


plot variables
    no underscores
    velocity
    density
    density,avg
    temperature
    temperature, avg

```

```

    energy
    stress
    stress, avg
end

history plot variables
    no material globals
end

$$$ -----
$$$ --- MATERIALS

${i=0}
{loop(nn)}
    ${i=i+1}
material {i}      $$$ Copper spheres
    model = 100
end

{EndLoop}

$--- ELASTIC-PLASTIC ---
model 100 cth elastic plastic
    eos model      = 11
    yield model    = 12
end

$$$ EOS
model 11, keos sesame
feos = 'sesame'
    neos = 3320
    clip = 1.0
end

```

```
$$$ YIELD  
model 12 johnson cook ep  
    matlabel = 'COPPER'  
end  
  
exit
```

# References

1. Materials research society symposium proceedings: The granular state. In *The Granular State* (San Francisco, 2000), S. Sen and M. Hunt, Eds., vol. 627, Materials Research Society.
2. AGUI, J. *To be submitted*.
3. ALLEN, M., AND TILDESLEY, D. *Computer Simulation of Liquids*. Oxford. Clarendon, 1987.
4. BALL, J. He died with his best buddy, citizen times, March 19 2006.
5. BARNES, G. Study of collisions part i: Survey of the periodical literature. *American Journal of Physics* 26 (1958), 5–8.
6. BARNES, G. Study of collisions part ii: Survey of the textbooks. *American Journal of Physics* 26 (1958), 9–12.
7. BATTEH, J., AND POWELL, J. Shock propagation in the one-dimensional lattice at nonzero initial temperature. *Journal of Applied Physics* 49, 7 (1978), 3933–3940.
8. BELL, R., AND HERTEL, E. An improved material interface reconstruction algorithm for eulerian codes, 1992.
9. BHATNAGAR, P. *Nonlinear Waves in One-dimensional Dispersive Systems*. Clarendon Press, Oxford, 1979.
10. BOCCHIERI, P., SCOTTI, A., BEARZI, B., AND LOINGER, A. Anharmonic chain with lennard-jones interaction. *Physical Review A* 2, 5 (1970), 2013.
11. BOKOR, A., AND LEVENTHALL, H. The measurement of initial impact velocity and contact time. *Journal of Physics D: Applied Physics* 4 (1971), 160.
12. BOYLE, J. Wnc honors ‘fallen heroes’, citizen times, March 22 2006.
13. BROWN, K., SUMMERS, R., GLASS, M., GULLERUD, A., HEINSTEIN, M., AND JONES, R. Acme: Algorithms for contact in a multiphysics environment api version 1.0, 2001.
14. BRUCK, H. A one-dimensional model for designing functionally graded materials to manage stress waves. *International Journal of Solids and Structures* 37 (2001), 6383–6395.
15. BURGERS, J. Mathematical examples illustrating relations occurring in the theory of turbulent fluid motion. *Trans. R. Neth. Acad. Sci.* 17 (1939), 1–53.
16. CARROLL, S., DRAKE, R., HENSINGER, D., LUCHINI, C., PETNEY, S., ROBBINS, J., ROBINSON, A., SUMMERS, R., VOTH, T., WEIRS, V., WONG, M., BRUNNER, T., GARASI, C., HALL, T., AND HANSHAW, H.L., M. T. Alegra: Version 4.6 (revised), 2005.
17. CEI. <http://www.ensight.com>, 2005.

18. CHHABILDAS, L., KONRAD, C., MOSHER, D., REINHARD, W., DUGGINS, B., TRUCANO, T., SUMMERS, R., AND PEERY, J. A methodology to validate 3d arbitrary lagrangian eulerian codes with applications to alegra. *International Journal of Impact Engineering* 23, 1 (1999), 101–112.
19. COAPLEN, J., STRONGE, W., AND RAVANI, B. Work equivalent composite coefficient of restitution. *International Journal of Impact Engineering* 30 (2004), 581–591.
20. COSTE, C., FALCON, E., AND FAUVE, S. Solitary waves in a chain of beads under hertz contact. *Physical Review E* 56, 5 (1997), 6104–6117.
21. COSTE, C., AND GILLES, B. On the validity of hertz contact law for granular material acoustics. *The European Physical Journal B* 7 (1999), 155–168.
22. CUBIT. <http://cubit.sandia.gov>, 2005.
23. DARAIO, C., NESTERENKO, V., HERBOLD, E., AND JIN, S. Energy trapping and shock disintegration in a composite granular medium. *Physical Review Letters* 96 (2006), 058002.
24. DELUCA, J., AND LICHTENBERG, A. Energy transitions and time scales to equipartition in the fermi-pasta-ulam oscillator chain. *Physical Review E* 51 (1995), 2877–2885.
25. DONEY, R., AND SEN, S. Impulse absorption by tapered horizontal alignments of elastic spheres. *Physical Review E* 72, 041304 (2005), 1–11.
26. DONEY, R., AND SEN, S. *Ordered and highly scalable granular media for shock mitigation*, vol. ARL-TR-3612. Army Research Laboratory, 2005.
27. DONEY, R., AND SEN, S. The decorated, tapered, and highly nonlinear granular chain. *Physical Review Letters* 97, 155502 (2006), 1–4.
28. DONEY, R., AND SEN, S. Energy partitioning and fluctuations in tapered chains. *To be submitted* (2007).
29. DURAN, J. *Sands, Powders, and Grains : An Introduction to the Physics of Granular Materials*. Springer, Berlin, 1999.
30. FERMI, E., PASTA, J., AND ULAM, S. *The Collected Works of Enrico Fermi, “Studies of Non Linear Problems”*, vol. 2. University of Chicago Press, Chicago, 1965.
31. FORD, J. Equipartition of energy for nonlinear systems. *Journal of Mathematical Physics* 2, 3 (1961), 387.
32. FREY, R. Personal communication, 2005.
33. FREY, R., GNIAZDOWSKI, N., LI, T., AND TARZIAN, F. Ballistic shock from explosive launchers, 2005.
34. GAMA, B., BOGETTI, T., FINK, B., YU, C., CLAAR, H., EIFERT, AND GILLESPIE, J. Aluminum foam integral armor: a new dimension in armor design. *Composite Structures* 52 (2001), 381.
35. GARDENER, C., GREENE, J., KRUSKAL, M., AND MIURA, R. Method for solving the korteweg-devries equation. *Physical Review Letters* 19, 19 (1967), 1095–1097.
36. GOLDSMITH, W. *Impact: The Theory and Physical Behavior of Colliding Solids*. Dover, Mineola, New York, 2001.
37. GOLDSTEIN, H. *Classical Mechanics*, 2nd ed. Addison-Wesley, Reading, Massachusetts, 1980.
38. GOTTLIEB, H. Frequencies of oscillators with fractional-power non-linearities. *Journal of Sound and Vibration* 261 (2003), 557–566.

39. HARTOG, J. D. *Mechanical Vibrations*. Dover, New York, 1985.
40. HAYASHI, C. *Nonlinear Oscillations in Physical Systems*. McGraw-Hill, New York, 1964.
41. HAYES, A., WANG, A., DEMPSEY, B., AND MCDOWELL, D. Mechanics of linear cellular alloys. *Mechanics of Materials* 36 (2004), 691.
42. HERRMANN, F., AND SCHMLZLE, P. Simple explanation of a well-known collision experiment. *American Journal of Physics* 49, 8 (1981), 761–764.
43. HERRMANN, F., AND SCHMLZLE, P. Simple explanation of a well-known collision experiment - response. *American Journal of Physics* 52, 1 (1984), 84–84.
44. HERRMANN, F., AND SEITZ, M. How does the ball-chain work? *American Journal of Physics* 50, 11 (1982), 977–981.
45. HERTZ, H. 'Über die berührung fester elastischer körper (on the behavior of solid elastic bodies). *J. Reine Angew. Math* 92 (1882), 156–171.
46. HESSEL, R., PERINOTTO, A., ALFARO, R., AND FRESCHI, A. Force-versus-time curves during collisions between two identical steel balls. *American Journal of Physics* 74, 3 (2006), 176–179.
47. HIRSCHFELDER, J., CURTISS, C., AND BIRD, R. *Molecular theory of gases and liquids*. John Wiley and Sons, New York, 1954.
48. JAEGER, H., NAGEL, R., AND BEHRINGER, R. Granular solids, liquids, and gases. *Review of Modern Physics* 68, 4 (1996), 1259–1273.
49. JAEGER, H., AND NAGEL, S. Physics of the granular state. *Science* 255, 5051 (1992), 1523–1530.
50. JOB, S., MELO, F., SOKOLOW, A., AND SEN, S. How hertzian solitary waves interact with boundaries in a 1d granular medium. *Physical Review Letters* 94, 178002 (2005), 1–4.
51. KAKALIOS, J. Resource letter gp-1: Granular physics or nonlinear dynamics in a sandbox. *American Journal of Physics* 73, 1 (2005), 8–22.
52. KORTEWEG, D., AND DEVRIES, G. On the change of form of long waves advancing in a rectangular canal, and on a new type of long stationary waves. *Philosophical Magazine* 39 (1895), 422–443.
53. LANDAU, L., AND LIFSHITZ, E. *Theory of Elasticity*. Pergamon Press, Oxford, 1970.
54. LEROY, B. Collision between two balls accompanied by deformation - a qualitative approach to hertz theory. *American Journal of Physics* 53, 4 (1985), 346–349.
55. LOVE, A. *A Treatise on the Mathematical Theory of Elasticity*. Dover, New York, 1955.
56. LUDING, S., CLÉMENT, E., BLUMEN, A., RAJCHENBACH, J., AND DURAN, J. Studies of columns of beads under external vibrations. *Physical Review E* 49, 2 (1994), 1634.
57. MANCIU, F., AND SEN, S. Secondary solitary wave formation in systems with generalized hertz interactions. *Physical Review E* 66, 016616 (2002), 1–11.
58. MANCIU, M. *Nonlinear Acoustics of Granular Media*. PhD thesis, State University of New York, The University at Buffalo, 2000.
59. MANCIU, M., SEN, S., AND HURD, A. The propagation and backscattering of soliton-like pulses in a chain of quartz beads and related problems. (i). propagation. *Physica A* 274 (1999), 588–606.

60. MANCIU, M., SEN, S., AND HURD, A. The propagation and backscattering of soliton-like pulses in a chain of quartz beads and related problems. (ii). backscattering. *Physica A* 274 (1999), 607–618.
61. MANCIU, M., SEN, S., AND HURD, A. Impulse propagation in dissipative and disordered chains with power-law repulsive potentials. *Physica D* 157 (2001), 226–240.
62. MATWEB. <http://www.matweb.com> (accessed aug. 2004), Aug. 2004 2005.
63. MCNAMARA, S., AND YOUNG, W. Inelastic collapse and clumping in a one-dimensional granular medium. *Physics of Fluids A* 4, 3 (1992), 496.
64. MEHTA, A., Ed. *Granular Matter*. Springer, Berlin, 1994.
65. MELO, F., JOB, S., SANTIBANEZ, F., AND TAPIA, F. Experimental evidence of shock mitigation in a hertzian tapered chain. *Physical Review E* 73, 4 (2006).
66. MICKENS, R. *Mathematical Methods for the Natural and Engineering Sciences*, vol. 65 of *Series on Advances in Mathematics for Applied Sciences*. World Scientific, New Jersey, 2004.
67. MICKENS, R. E. *Oscillations in Planar Dynamic Systems*. World Scientific, Singapore, 1996.
68. MINORSKY, N. *Nonlinear Oscillations*. D. Van Nostrand, Princeton, 1962.
69. MOHAN, T., AND SEN, S. A new equilibrium phase in discrete nonlinear chains (invited). *Pramana - Journal of Physics* 64 (2005), 423–431.
70. MOON, F. *Chaotic Vibrations*. John Wiley and Sons, Hoboken, 2004.
71. MOTULSKY, H., AND CHRISTOPOULOS, A. Graphpad prism, 2003.
72. NAKAGAWA, M., AGUI, J., WU, D., AND EXTRAMIANA, D. Impulse dispersion in a tapered granular chain. *Granular Matter* 4 (2003), 167–174.
73. NAYFEH, A., AND MOOK, D. *Nonlinear Oscillations*. John Wiley and Sons, New York, 1979.
74. NAYFEH, A. H. *Perturbation Methods*. John Wiley and Sons, New York, 1973.
75. NESTERENKO, V. Propagation of nonlinear compression pulses in granular media. *Journal of Applied Mechanics and Technical Physics* 5 (1984), 136–148.
76. NESTERENKO, V. *Dynamics of Heterogeneous Media*. Springer, New York, 2001.
77. NESTERENKO, V., LAZARIDI, A., AND SIBIRYAKOV, E. The decay of soliton at the contact of two “acoustic vacuums”. *Journal of Applied Mechanics and Technical Physics* 36, 2 (1995), 166–168.
78. NETTEL, S. *Wave Physics: Oscillations - Solitons - Chaos*, 3rd ed. Advanced Texts in Physics. Springer, Berlin, 2003.
79. PEERY, J., AND CARROLL, D. Multi-material ale methods in unstructured grids. *Computer Methods in Applied Mechanics and Engineering* 187, 3-4 (2000), 591–619.
80. PFANNES, J. *Energy Propagation in Granular Chains*. M. s., State Univeristy of New York, the University at Buffalo, 2003.
81. PIAZZA, F., LEPRI, S., AND LIVI, R. Cooling nonlinear lattices toward energy localization. *Chaos* 13, 2 (2003), 637.
82. PÖSCHEL, T., AND BRILLIANTOV, N. Extremal collision sequences of particles on a line: optimal transmission of kinetic energy. *Physical Review E* 63, 021505 (2001), 1–9.



83. REBBI, C. Solitons. *Scientific American* 240, 2 (1979), 92–116.
84. REIF, F. *Fundamentals of statistical and thermal physics*. McGraw-Hill, Boston, 1965.
85. REIGADA, R., S. A., AND LINDENBERG, K. Energy relaxation in nonlinear one-dimensional lattices. *Physical Review E* 64 (2001), 066608.
86. REMOISSENET, M. *Waves called solitons*. Springer, Berlin, 1999.
87. ROSAS, A., BUCETA, J., AND LINDENBERG, K. Dynamics of two granules. *Physical Review E* 68, 021303 (2003), 1–8.
88. ROSAS, A., AND LINDENBERG, K. Pulse dynamics in a chain of granules with friction. *Physical Review E* 68, 041304 (2003), 1–13.
89. ROSAS, A., AND LINDENBERG, K. Pulse propagation in chains with nonlinear interactions. *Physical Review E* 69 (2004), 016615.
90. ROSAS, A., AND LINDENBERG, K. Pulse velocity in a granular chain. *Physical Review E* 69, 037601 (2004), 1–3.
91. ROSSMANITH, H., AND SHUKLA, A. Photo-elastic investigation of dynamic load-transfer in granular media. *Acta Mechanica* 42, 3-4 (1982), 211–225.
92. RUSSELL, J. Report on waves. *Proceedings of the Royal Society of Edinburgh* (1844), 319–320.
93. SANDER, J. On the development of the theory of the solitary wave: a historical essay. *Acta Mechanica* 86 (1991), 111–152.
94. SARMIENTO, A., REIGADA, R., ROMERO, A., AND LINDENBERG, K. Enhanced pulse propagation in nonlinear arrays of oscillators. *Physical Review E* 60, 5 (1999), 5317.
95. SEN, S., AND MANCIU, M. Discrete hertzian chains and solitons. *Physica A* 268 (1999), 644–649.
96. SEN, S., AND MANCIU, M. Solitary wave dynamics in generalized hertz chains: an improved solution to the equations of motion. *Physical Review E* 64, 056605 (2001), 1–4.
97. SEN, S., AND MANCIU, M. Thermalizing an impulse. *Physica A* 299 (2001), 551–558.
98. SEN, S., MANCIU, M., AND WRIGHT, J. Solitonlike pulses in perturbed and driven hertzian chains and their possible applications in detecting buried impurities. *Physical Review E* 57, 2 (1998), 2386.
99. SEN, S., MOHAN, T., AND PFANNES, J. The quasi-equilibrium phase in nonlinear 1d systems. *Physica A* 342, 1-2 (2004), 336–343.
100. SEN, S., PFANNES, J., AND MOHAN, T. The quasi-equilibrium state: a tale of certain soundless systems (invited). *journal of the Korean Physical Society* 46 (2005), 571–573.
101. SEN, S., AND SINKOVITS, R. Sound propagation in impure granular columns. *Physical Review E* 54, 6 (1996), 6857–6865.
102. SINKOVITS, R., AND SEN, S. Nonlinear dynamics in granular columns. *Physical Review Letters* 74, 14 (1995), 2686.
103. SIVARDIERE, J. Using the virial theorem. *American Journal of Physics* 54 (1986), 1100.
104. SOKOLOV, A., BITTLE, E., AND SEN, S. Solitary wave train formation in hertzian chains. *submitted to Physical Review E (Rapid Communication)* (2006).

105. STEWART, J. T., AND H.B. *Nonlinear Dynamics and Chaos*. John Wiley and Sons, Chichester, 1987.
106. STOKER, J. *Nonlinear Vibrations*. Interscience Publishers, New York, 1950.
107. STOWE, K. *Introduction to Statistical Mechanics and Thermodynamics*. John Wiley and Sons, New York, 1984.
108. STROGATZ, S. *Nonlinear Dynamics and Chaos*. Westview Press, 1994.
109. STRONGE, W. *Impact Mechanics*. Cambridge University Press, Cambridge, 2000.
110. SUMMERS, R., PEERY, J., WONG, M., HERTEL, E., TRUCANO, T., AND CHHABILDAS, L. Recent progress in algebra development and application to ballistic impacts. *International Journal of Impact Engineering* 20, 6-10 (1997), 779–788.
111. TABOR, M. *Chaos and Integrability in Nonlinear Dynamics: An Introduction*. Wiley-Interscience, New York, 1989.
112. THOMPSON, J., AND STEWART, H. *Nonlinear Dynamics and Chaos*. John Wiley and Sons, Great Britain, 1986.
113. TOBOLSKY, A., HOPKINS, I., AND SAMULSKI, E. Energy transients in harmonic oscillator systems. *American Journal of Physics* 38 (1970), 226.
114. TODA, M. *Theory of Nonlinear Lattices*. Springer, Berlin, 1981.
115. VAKAKIS, A. Normal modes and global dynamics of a two-degree of freedom nonlinear system - part 1: low energies. *International journal of nonlinear mechanics* 27 (1992), 861–874.
116. WALTON, O., AND BRAUN, R. Viscosity, antigranulocytes-temperature, and stress calculation for shearing assemblies of inelastic, frictional disks. *Journal of Rheology* 30, 5 (1986), 949–980.
117. WARR, S., H. J. Energy input and scaling laws for a single particle vibrating in one dimension. *Physical Review E* 52, 5 (1995), 5596.
118. WHITHAM, G. *Linear and Nonlinear Waves*. John Wiley, New York, 1999.
119. WOLFRAM, S. Origins of randomness in physical systems. *Physical Review Letters* 55 (1985), 449.
120. WRIGHT, T. Weak shocks and steady waves in a nonlinear elastic rod or granular material, 1984.
121. WU, D. Conservation principles in solitary impulse propagation through granular chains. *Physica A* 315, 1-2 (2002), 194–202.
122. ZABUSKY, N., AND KRUSKAL, M. Interaction of “solitons” in a collisionless plasma and the recurrence of initial states. *Physical Review Letters* 15, 240-243 (1965).

---

## Distribution List

---

DIRECTOR  
US ARMY RSRCH LAB  
ATTN AMSRD ARL RO EN B LAMATTINA  
PO BOX 12211  
RESEARCH TRIANGLE PARK NC 27709-2211

DARPA/DSO  
ATTN J GOLDWASSER  
3701 NORTH FAIRFAX DR  
ARLINGTON VA 22203-1714

US ARMY RSRCH LAB  
ATTN AMSRD ARL WM TA S E SCHOENFELD  
ATTN AMSRD ARL WM TA B LEAVY  
ATTN AMSRD ARL WM TA M BURKINS  
ATTN AMSRD ARL WM TA R DONEY (5 COPIES)  
ATTN AMSRD ARL WM TA C KRAUTHAUSER  
ATTN AMSRD ARL WM TA S BARTUS  
BLDG 393  
ABERDEEN PROVING GROUND MD 21005

US ARMY RSRCH LAB  
ATTN AMSRD ARL WM T P BAKER  
BLDG 309  
ABERDEEN PROVING GROUND MD 21005

US ARMY RSRCH LAB  
ATTN AMSRD ARL WM TE J POWELL  
ATTN AMSRD ARL WM TE C HUMMER  
BLDG 1116A  
ABERDEEN PROVING GROUND MD 21005

US ARMY RSRCH LAB  
ATTN AMSRD ARL WM J MCCAULEY  
BLDG 4600  
ABERDEEN PROVING GROUND MD 21005